Stony Brook University

Two-Component Bosons in State-Dependent Optical Lattices

A Dissertation Presented

by

Daniel Alexander Pertot

to

The Graduate School

in Partial Fulfillment of the Requirements

for the Degree of

Doctor of Philosophy

in

Physics

Stony Brook University

December 2011

Stony Brook University

The Graduate School

Daniel Alexander Pertot

We, the dissertation committee for the above candidate for the Doctor of Philosophy degree, hereby recommend acceptance of this dissertation.

Dominik A. Schneble – Dissertation Advisor
Associate Professor, Department of Physics and Astronomy

Harold J. Metcalf – Chairperson of Defense
Distinguished Teaching Professor, Department of Physics and Astronomy

Jacobus Verbaarschot
Professor, Department of Physics and Astronomy

Péter Petreczky
Scientist, Physics Department,
Brookhaven National Laboratory

This dissertation is accepted by the Graduate School.

Lawrence Martin
Dean of the Graduate School

Abstract of the Dissertation

Two-Component Bosons in State-Dependent Optical Lattices

by

Daniel Alexander Pertot

Doctor of Philosophy

in

Physics

Stony Brook University

2011

Ultracold atoms in optical lattices provide a highly controllable environment for the clean experimental realization of various model Hamiltonians from condensed matter and statistical physics. For example, the two-component Bose-Hubbard model, which reduces to an anisotropic spin-$^1/_2$ Heisenberg model in a certain limit and thus allows for the study of quantum magnetism, can be implemented by using bosons with two different internal states that couple differently to an optical lattice potential. In this thesis, I present our first experiments with two-component hyperfine-state mixtures of ultracold ^{87}Rb atoms in a state-dependent optical lattice, both in the strongly correlated regime and in the context of nonlinear atom optics.

For the production of ^{87}Rb Bose-Einstein condensates we have developed a moving-coil transporter apparatus featuring a magnetic TOP trap which serves as a "phase-space funnel" to load a crossed optical dipole trap. The apparatus further incorporates a

three-dimensional optical lattice setup with simultaneously usable hyperfine state-dependent and state-independent lattice beams of different spacing along the vertical axis. Internal state control is performed via rf and microwave Rabi pulses and Landau-Zener sweeps.

As a first step towards studying strongly correlated two-component mixtures, we have realized a state-selective superfluid-to-Mott insulator transition, where one component enters the Mott insulator regime, while the other one stays superfluid. Using the state-dependent lattice we can tune the second component's properties from highly superfluid to strongly localized. At both extremes we find a reduction of the coherence of the primary component, i.e. a shift of the Mott transition to smaller values of the ratio U/t of interaction to tunneling. We ascribe this to a polaron-like dressing on the one hand, and a "quantum emulsion" causing a disordered atomic background potential on the other hand.

Further, we have observed and studied four-wave mixing of two-component matter waves. Using state-selective Kapitza-Dirac diffraction of a two-component BEC, we prepare seed and pump modes differing both in momentum and internal state. A novel collinear four-wave mixing process then populates the initially empty output modes. While this process can complicate studies of bosonic mixtures loaded into state-dependent optical lattices, it might prove useful for possible applications in quantum atom optics.

Contents

List of Figures

Acknowledgements

The end of my journey as a graduate student is approaching, and there are many people who have influenced my path and contributed in one way or another to make this endeavor a successful one, after all.

First and foremost, I would like to thank my advisor, Dominik Schneble, for giving me the possibility to explore the exciting field of ultracold atoms in his group. He has been a constant source of inspiration and his enthusiasm about physical concepts and experiments is contagious. With his guidance and vision, Dominik has led us through all the ups and downs that come with building a new experiment, and has kept us on track towards the bigger goals. He is also a great mentor, takes good care of his students, and works to make them thrive and prosper. It is hard to imagine a better advisor, and I have been extremely lucky to have been able to work with him.

I have also had the pleasure to work with great lab mates, of whom I first would like to thank David Sproles and Rebekah Schiller, who had done the initial work in building the experiment together with Dominik. It has been fun to design and build the TOP coils with David, and Rebekah has also contributed a lot to our lab, before she left us to become a teacher, which I am sure she is great at. Several generations of German exchange students have done their Master's thesis in our lab, and I am indebted to all of them. Stephan Albert characterized and optimized our MOT and the magnetic transport into the science cell, and together with Rebekah laid the foundations for achieving BEC with our machine. This then was the privilege of Daniel Greif, who worked out and optimized our evaporative cooling sequence, and characterized our first BEC. It has been a great time working with Daniel and we also had fun times outside the lab. René Reimann, another German exchange student, contributed significantly to our state-dependent lattice setup by becoming the master of our Verdi and Coherent 899 lasers, among other things. Moreover, René's dark humor and his stories from his time as a student in Germany were very entertaining during many lunch and dinner breaks.

I am very grateful to my fellow PhD student Bryce Gadway, who has been

an invaluable addition to our group. Not only is he accompanied by an air of brilliance, but he is also a very talented, tireless and committed experimentalist, and it has been great to work with him. He has very interesting ideas, and I have learned a lot from our discussions about physics. Further, he can also be quite a funny guy, especially after one or two beers (keyword "Tecate!"). Additionally, I have to thank him for giving me quite a few rides in his car, when my car was making trouble. I am curious to see where Bryce will do his postdoc, but wherever he will go I am sure he will do very well in the future.

Finally, although they have been working in the lab mostly after my active time, I would like to thank Jeremy Reeves, our (meanwhile not so) new PhD student, and Matthias Vogt, who had been the last German exchange student during my time in Dominik's group. In addition, I would like to thank the various undergraduate students who had done projects in our lab, among them Azure Hanson, Bartosz Bogucki, who became our LIAD and microcontroller expert, Justin Tian, and Gaku Nagashima.

I would also like to thank all the members of the other AMO groups in Stony Brook and the other "inhabitants" of the basement, who helped with equipment, parts, or general advice and discussions. Among them are Tom Bergeman, Tom Weinacht and his group, Hal Metcalf and his group, in particular Jason Reeves for his valuable help with connectorizing high-power fibers, Marty Cohen, from whose experience and knowledge all the AMO groups are benefitting, John Noe from the laser teaching center, and Peter Koch, who has been lending us various pieces of equipment, notably a spectrum analyzer and a crucial SMA elbow.

Moreover, I would like to express my gratitude towards Hal Metcalf, Jac Verbaarschot, and Péter Petreczky for agreeing to serve on my defense committee and for reviewing my dissertation despite the organizational complications involved. Many thanks also go to Michael Köhl and the members of his group for their patience and support while I was working on completing this dissertation.

Further, I am grateful to all the people from the Physics main office who helped me navigate through the typical and less typical administrative issues that can arise during a graduate student's career. In particular, I would like to mention Pat Peiliker, Maria Hofer, Pam Burris, Matt Gilbert, and of course Sara Lutterbie, who somehow managed to make even the most complex administrative matters enjoyable. Regarding guidance in the more fundamental decisions, I would like to thank all the Graduate Program Directors during my time at Stony Brook, Peter Stephens, Laszlo Mihaly, and Jac Verbaarschot, who have always been very supportive.

Also, I would like to say thank you to all my friends from Stony Brook, for the many lunches and dinners, the car rides, the board game nights, the weekend activities, and the occasional trips to the city. Without your company and continued friendship, my time in Stony Brook would not have been the same! Thanks also go to my friends from back home in Germany for keeping in touch over the years.

Finally, I would like to thank my parents, Marianne and Carlo, who have always taken good care of me and have always supported me in my pursuits. Vielen Dank für Eure Unterstützung, und dafür, dass Ihr immer für mich da wart und seid!

This work was supported by the Research Foundation of SUNY, the Office of Naval Research (ONR), and the National Science Foundation (NSF).

Chapter 1

Introduction

In 1925, inspired by Bose's work [1], Einstein conjectured that at sufficiently high phase-space density a gas of bosons saturates and any additional particles have to condense into the ground state, which can thus become macroscopically populated [2, 3]. The validity of this idea has been demonstrated in spectacular clarity in 1995 by the achievement of Bose–Einstein condensation (BEC) in dilute atomic gases [4–7]. These gases, however, are not ideal Bose gases. Binary collisions between pairs of atoms lead to weak interactions between the bosons, and the resultant deviations from the non interacting case were at the focus of early experimental and theoretical research in the field of ultracold atoms [8, 9].

About a decade ago, the focus shifted towards the experimental realization and study of strongly interacting many-body systems which are characterized by the competition of kinetic energy and interaction energy [10]. Such strongly correlated many-body systems can be obtained either by tightly confining the atoms in optical standing waves [11], commonly called optical lattices, or by tuning their mutual interactions via Feshbach resonances [12]. Following the first approach and using a three-dimensional optical lattice, in 2002 Greiner *et al.* [13] were able to observe the quantum phase transition from a lattice superfluid to a Mott insulator, realizing a theoretical proposal of Jaksch *et al.* from 1998 [14]. This hallmark experiment constitutes an important achievement creating inter-disciplinary links between atomic physics, quantum optics, condensed matter and statistical physics.

Many new, interesting phenomena arise when a second atomic species with properties different from the first is added. Such mixtures allow for the study of many interesting topics, such as the two-component Bose-Hubbard model [15–18], with its connection to quantum magnetism [15, 19], and models for decoherence mechanisms [20, 21].

In this thesis, I describe a new versatile experimental setup to produce

two-component hyperfine-state mixtures of ultracold ^{87}Rb atoms in a state-dependent optical lattice. Further, I discuss our first experiments, both in the strongly correlated regime and in the context of nonlinear atom optics.

Bosonic mixtures in optical lattices

Compared to the single-component case, the description of mixtures presents richer physics, but also depends on additional parameters, such as the ratio of the tunneling rates, the interspecies interaction, and the relative atom numbers. The introduction of a second component allows for the investigation of important phenomena such as polaron physics [22–24] and phonon-mediated long-range interactions [18, 23], as well as effects of impurities and disorder [25–29].

Here, I report on the observation of many-body interaction effects for a homonuclear bosonic mixture in a three-dimensional optical lattice with variable state dependence along one axis. Near the superfluid-to-Mott insulator transition for one component, we find that the presence of a second component can reduce the apparent superfluid coherence, most significantly when the second component either experiences a strongly localizing lattice potential or none at all. We examine this effect by varying the relative populations and lattice depths, and discuss the observed behavior in view of recent proposals for atomic-disorder and polaron-induced localization.

Four-wave mixing and non-linear atom optics

In four-wave mixing, two waves form a grating from which a third wave diffracts, thus generating a fourth wave. Four-wave mixing is a fundamental, well-studied concept in nonlinear optics and spectroscopy [30]. Its matter-wave analogue, based on binary collisions in ultracold atomic gases, was first demonstrated experimentally a decade ago [31–33], establishing the field of nonlinear atom optics [34]. Matter-wave four-wave mixing has been used for coherent matter-wave amplification [35, 36], and for the generation of correlated atom pairs [34–38]. Energy and momentum conservation require the magnitudes of all atomic momenta in the center-of-mass frame to be equal which, for atoms in a single internal state, necessitates a two-dimensional geometry [32, 33]. By modifying the dispersion relation with an optical lattice, non-degenerate four-wave mixing of a single species becomes possible also in one dimension [39–41].

Despite considerable theoretical work on atomic four-wave mixing (FWM) with more than one internal state [42–45], experiments have only very recently started to explore possible mechanisms for such FWM [38, 46]. The addi-

tional internal degree of freedom allows for degenerate FWM to occur in one dimension, with pairs of waves in different internal states sharing the same momentum mode, opening up possibilities to generate non-classical matter-wave states, e.g. with macroscopic spin entanglement [43, 44].

In this thesis, I demonstrate free-space collinear atomic FWM involving two internal states with distinct, macroscopically populated momentum modes. Starting from a single-species Bose–Einstein condensate, seed and pump modes are prepared through microwave state transfer and state-selective Kapitza–Dirac diffraction. Four-wave mixing then populates the initially empty output modes. Simulations based on a coupled-mode expansion of the Gross–Pitaevskii equation are in very good agreement with experiment. We find that for a homonuclear mixture of interacting superfluids, four-wave mixing processes can alter the expected momentum-space distributions, masking or even mimicking in-situ interaction effects. Moreover, our system should be of interest in the context of quantum atom optics [47].

Outline of the thesis

After summarizing the fundamentals of BEC in dilute atomic gases in chapter 2, I review important concepts from atomic physics in chapter 3. In chapter 4, a description of our experimental apparatus is given and experimental techniques for the probing and the manipulation of the motion and the internal states of the BEC are discussed. Then, in chapter 5, I describe our experiments with two-component bosons in optical lattices. After a short look at the two-component Bose-Hubbard model, our observations on the effects of a second tunable "background" component on the SF-MI transition of a first component are discussed and interpreted in terms of lattice polarons on the one hand, and localization and percolation phenomena due to an atomic disorder potential on the other. In chapter 6, I will switch to our experiments on two-component four-wave mixing, which, for the most part, are performed on a trapped continuum BEC in three dimensions. Finally, a short conclusion will be given in chapter 7.

Chapter 2

Fundamentals: Bose-Einstein condensation in dilute gases

2.1 Introduction

The idea of Bose-Einstein condensation has its origin in 1924, when Einstein applied Bose's new way of calculating Planck's black-body radiation spectrum [1] to the ideal monatomic gas [2, 3]. He found that at a certain point the density of the gas would saturate, and argued that any increase in density beyond this point would lead to a "condensation" of the excess particles into the state of lowest energy.

Initially, this *"peculiar condensation phenomenon"* had *"rather got the reputation of having only a purely imaginary existence,"* as London had put it in 1938 [48], when he insightfully suggested that the λ-transition and thus superfluidity in liquid Helium could be related to the concept of Bose-Einstein condensation [48, 49]. Even though his idea was appealing, the strong interactions in this system considerably complicate the theoretical understanding and obscure the basic physics of Bose-Einstein condensation. Therefore, for many decades a cloud of mystery was hanging over the topic and motivated physicists to find an experimental system in which the phenomenon could be clearly observed and studied.

Only 70 years after its prediction, Bose-Einstein condensation of weakly interacting particles could be unambiguously realized and observed in an ultracold dilute gas of neutral alkali atoms [4–7]. This involved cooling matter down to the lowest temperatures ever achieved, as the temperatures for condensation are extremely low owing to the extreme diluteness necessary to prevent the atoms from simply combining into molecules. The achievement of BEC thus builds heavily upon the breakthroughs in laser cooling and atom

trapping [50] and evaporative cooling [51] made throughout the 1980s.

Since the achievement of BEC in 1995, considerable theoretical and experimental progress has been made. Many textbook-like experiments not only made it possible to accurately test 50-year-old predictions by Bogoliubov and others, but also to explore entirely new questions. Detailed historical accounts can be found, for example, in the Nobel lectures of Cornell, Wieman and Ketterle [52, 53].

The phenomenon of Bose-Einstein condensation and its fundamental properties are described in detail in many statistical physics textbooks [54, 55], in textbooks about many-body physics [56], and also in books that are devoted to the particular case of BEC in the dilute alkali gases [57, 58]. Much knowledge can also be found in review articles [8, 9, 59]. In the following, the basic properties which are relevant for the remainder of this thesis are introduced and discussed.

2.2 Bose vs. Fermi statistics

In quantum mechanics the symmetrization postulate states that the wavefunction of a system of identical particles has to be either completely symmetric or completely anti-symmetric under the exchange of any two particles. In a simple picture, this can be explained by considering the wave function of a system of identical particles. Now, if we exchange the labels of two particles in the wavefunction, measurements must not depend on this exchange. Assuming that the wavefunction gets multiplied by a phase factor when two labels are interchanged, the modulus of the wavefunction is unaffected only if the phase factor is either $+1$ or -1. Particles of the first kind (completely symmetric) are called bosons and they obey Bose-Einstein statistics, while particles of the second kind (completely anti-symmetric) are called fermions and they obey Fermi-Dirac statistics. In all experiments performed to date, fermions have corresponded to particles with half-integer spin, while particles with integer spins have corresponded to bosons. In 1940, this connection between spin and exchange statistics could also be derived theoretically by Pauli [60] based on relativistic quantum field theory (spin-statistics theorem). As an aside, more exotic exchange statistics are possible in less than three spatial dimensions, for example anyonic statistics in two dimensions [61] with connections to the fractional quantum Hall effect.

The exchange statistics of atoms leads to fundamentally different ways of how they behave at low temperatures. We see this by comparing the thermal de Broglie wavelength $\lambda_T = h/\sqrt{2\pi m k_B T}$ and hence the spatial extent of the single particle wave function of an atom with the average particle separation

$d = 1/n^{1/3}$. Here T is the temperature, m is the mass, k_B is Boltzmann's constant, h is Planck's constant, and n is the number density. The thermal de Broglie wavelength becoming as large as the average inter-particle spacing defines the degeneracy temperature T_D around which exchange statistics start to play a role, either bosonic or fermionic. Bose gases start to condense into the ground state and Fermi gases fill up the Fermi sea. For $T \gg T_D$ the exchange statistics becomes more or less unimportant, and Fermi, Bose and Boltzmann statistics essentially lead to the same physical properties.

Neutral atoms are, of course, composite bosons or fermions made up of more elementary particles. Therefore they have internal excitations and can, in principle, break apart into composites of different statistics. However, the temperatures considered here are so low, that all internal excitations are frozen out, and each atom can be regarded as a simple bosonic particle of mass m.

2.3 The ideal Bose gas in a harmonic trap

Let us first consider an ideal, i.e. non-interacting, Bose gas in a harmonic trapping potential. The Hamiltonian is a direct sum of single-particle Hamiltonians

$$H = \frac{\mathbf{p}^2}{2m} + \frac{1}{2} m \mathbf{q}^t \mathbf{\Omega} \mathbf{q} \tag{2.1}$$

where $\mathbf{\Omega}$ is a 3 by 3 matrix whose eigenvalues are the trap frequencies along the main axes of the harmonic potential (that is the main axes of the equipotential ellipsoids). According to the Bose-Einstein distribution function, the mean occupation of state i of energy ϵ_i is

$$\bar{n}_i = \frac{1}{e^{\beta(\epsilon_i - \mu)} - 1} \tag{2.2}$$

with $\beta = 1/k_B T$ and the chemical potential μ, which is determined from the condition that the mean total atom number has to be $N = \sum_i \bar{n}_i$. Since occupation numbers cannot become negative, the chemical potential has to stay below the ground state energy $\mu < \epsilon_0$. As μ approaches ϵ_0 from below, the occupation of the lowest energy state grows to larger and larger values until eventually all available particles are in the ground state.

Let us thus separate the ground state occupation from the sum over all energy levels before approximating the sum by an integral over the density of states $D(\epsilon)$ assuming closely spaced energy levels and temperatures far above

the level spacings:

$$N = \frac{1}{e^{\beta(\epsilon_0-\mu)}-1} + \int_0^\infty d\epsilon \, \frac{D(\epsilon)}{e^{\beta(\epsilon-\mu)}-1}. \tag{2.3}$$

If the total atom number exceeds the number of available occupancies in the thermal part (integral term), the thermal gas saturates and the excess number of particles have to populate the ground state of the system, i.e. it forms the Bose-Einstein condensate. We can compute the fraction of atoms in the condensate using the so called "Bose function" [54, 57], which is defined as

$$g_p(z) = \frac{1}{\Gamma(p)} \int_0^\infty dx \, \frac{x^{1/2}}{z^{-1}e^x - 1} = \sum_{n=1}^{\infty} \frac{z^n}{n^p} = \mathrm{Li}_p(z) \tag{2.4}$$

and which, more generally, is known as the polylogarithm function $\mathrm{Li}_p(z)$. In the special case $z = 1$ it reduces to the Riemann zeta function $g_p(1) = \zeta(p)$.

The particle density in the thermal component in the semi-classical approximation [9] is

$$n_T(\mathbf{r}) = \lambda_T^{-3} \, g_{3/2}(e^{\beta(\mu - V(\mathbf{r}))}). \tag{2.5}$$

When the temperature drops below a critical value

$$T_c = \frac{\hbar\bar{\omega}}{k_B} \frac{N^{1/3}}{[\zeta(3)]^{1/3}} \approx 0.94 \frac{\hbar\bar{\omega}}{k_B} N^{1/3}, \tag{2.6}$$

the ground state becomes macroscopically occupied and there is a phase transition between the normal phase and the Bose-Einstein condensate. Here, $\bar{\omega} = (\omega_x\omega_y\omega_z)^{1/3}$ is the mean trap frequency. For the ideal Bose gas in a three-dimensional harmonic trap, the condensate fraction behaves as

$$N_0/N = 1 - (T/T_c)^3 \tag{2.7}$$

for $T < T_c$. Note the remarkable feature of BEC that the transition temperature at which the ground state starts to be macroscopically populated is far above the energy distance to the first excited state for typical condensate atom numbers, $k_B T_c \gg \hbar\bar{\omega}$.

While the intuitive picture of Bose-Einstein condensation as described above captures the physical processes correctly, it fails in precisely defining what a Bose-Einstein condensate is. This was achieved by Penrose and Onsager in 1956 [62] who studied the single-particle density matrix of the many-body system $\rho(\mathbf{r_1}, \mathbf{r_2}) = \langle \Psi^\dagger(\mathbf{r_1})\Psi(\mathbf{r_2})\rangle$. A Bose-Einstein condensate exhibits one macroscopically occupied eigenvalue of the density matrix, which measures

the condensate fraction, and off-diagonal long-rage order [63] throughout the whole system. For Helium-4 at $T = 0$ the condensate fraction is only about 10%, whereas in dilute gases condensate fractions in excess of 95% can be achieved. The one-particle density matrix in a homogeneous system depends only on the relative distance $r = |\mathbf{r_1} - \mathbf{r_2}|$ between two locations. The zero-momentum component is macroscopically occupied if the one-particle density matrix tends to a finite value for $r \to \infty$, which is just the condensate fraction.

2.4 Taking into account interactions

The non-interacting Bose gas turns out to be quite an oversimplification even in the case of trapped dilute ultracold gases, where in fact, despite their diluteness, the interaction energy dominates. At the temperatures we are interested in here, only s-wave collisions contribute, since the atoms do not have enough kinetic energy to overcome the centrifugal barrier that is present for non-zero partial waves, i.e. collisions with angular momentum different from zero. Under the condition $k \ll 1/r_c$ where k is the modulus of the relative collision wave vector and r_c is a characteristic length scale of the interatomic potential, the potential can be safely replaced by a δ-function interaction potential,

$$V(\mathbf{r}, \mathbf{r}') = g\,\delta(\mathbf{r} - \mathbf{r}') \tag{2.8}$$

Intuitively speaking, the wave packet of the atomic motion does not have sufficiently high Fourier components to sample the details of the potential. This is often referred to as pseudo-potential approximation [54]. The strength g of this pseudo-potential can be re-expressed in terms of another quantity called the s-wave scattering length a_s, which can be interpreted in terms of the phase shift the scattered wave undergoes in the collision. For two colliding atoms of equal mass one obtains

$$g = 4\pi\hbar^2 a_s/m. \tag{2.9}$$

The problem of the interacting Bose gas can in general not be solved exactly any more. However, it has turned out that a simple mean-field solution describes most relevant physical observations very well, except for strong interactions and in low-dimensional systems. Generally, the corrections to the non-interacting model due to weak interactions are small. Finite-size effects and interactions shift T_c only a few percent away from the non-interacting value given above. While the transition temperature is not affected significantly by interactions, the shape of the condensate in the trap, its excitations and its dynamics are altered considerably, as we will see below.

2.5 The Gross-Pitaevskii equation

The full Hamiltonian for a weakly-interacting Bose gas is given in second quantization by

$$H = \int d^3r\, \Psi^\dagger(\mathbf{r}) \left[-\frac{\hbar^2}{2m}\nabla^2 + V_{\text{ext}}(\mathbf{r}) \right] \Psi(\mathbf{r}) + \frac{1}{2} \iint d^3r\, d^3r'\, \Psi^\dagger(\mathbf{r})\Psi^\dagger(\mathbf{r}')V(\mathbf{r}-\mathbf{r}')\Psi(\mathbf{r}')\Psi(\mathbf{r}) \quad (2.10)$$

where the "field" operators $\Psi(\mathbf{r})$ obey the canonical commutation relations for bosons

$$\begin{aligned} \left[\Psi(\mathbf{r}), \Psi^\dagger(\mathbf{r}')\right] &= \delta(\mathbf{r}-\mathbf{r}'), \\ \left[\Psi(\mathbf{r}), \Psi(\mathbf{r}')\right] &= 0, \\ \left[\Psi^\dagger(\mathbf{r}), \Psi^\dagger(\mathbf{r}')\right] &= 0. \end{aligned} \quad (2.11)$$

For a condensate, $\Psi(\mathbf{r})$ assumes a non-zero expectation value $\psi(\mathbf{r}) = \langle\Psi(\mathbf{r})\rangle$ which acts as a complex order parameter here. It can be regarded as a macroscopic wavefunction of the condensate. If one writes the field operator as its expectation value plus a fluctuation operator $\Psi(\mathbf{r}) = \psi(\mathbf{r}) + \delta\Psi(\mathbf{r})$, the time-dependent Schrödinger equation for the order parameter alone leads to the so-called Gross-Pitaevskii equation (GPE) for the condensate wavefunction [9]

$$\left[-\frac{\hbar^2}{2m}\nabla^2 + V(\mathbf{r}) + g_{3\text{D}}|\psi(\mathbf{r},t)|^2 \right] \psi(\mathbf{r},t) = i\hbar\,\partial_t\,\psi(\mathbf{r},t) \quad (2.12)$$

where $V(\mathbf{r})$ is the external potential, which includes the lattice as well as the trapping potential, and $g_{3\text{D}} = 4\pi\hbar^2 a_{\text{s}}/m$ is the nonlinear coupling with the s-wave scattering length a_{s}. Here, the condensate wavefunction is normalized to the total number of particles

$$\int \mathrm{d}^3r\ |\psi(\mathbf{r},t)|^2 = \int \mathrm{d}^3r\ n(\mathbf{r},t) = N. \quad (2.13)$$

This is only possible in this form if the particle density falls off sufficiently quickly for $r \to \infty$, such that the integral exists, or correspondingly that the condensate is confined in all three directions, which basically is the case in all experimental realizations.

2.6 Density profile: Thomas-Fermi approximation

In experiments one is usually in a situation of a large interaction parameter $Na_s/a_{\rm ho}$ because the atom number N is the range $N \approx 10^5$-10^6. Under these conditions, the kinetic energy term in the Gross-Pitaevskii equation may be neglected except for a small region at the surface of the cloud where the order parameter changes more rapidly across space. To good approximation, the ground state in the trap is then given by the Thomas-Fermi approximation, which leads to a density distribution [9]

$$n(\vec{r}, t=0) = N\,|\Phi_0(\vec{r})|^2 = \begin{cases} \left[\mu - V(\vec{r})\right]/g_{\rm 3D} & V(\vec{r}) < \mu \\ 0 & V(\vec{r}) \geq \mu, \end{cases} \tag{2.14}$$

with the chemical potential μ that is fixed by the atom number. The highest particle density $n^{\rm peak}$ occurs at the minimum of the trapping potential, which we define as the zero point of the energy scale. Note the simple but useful relation $\mu = n^{\rm peak}\, g_{\rm 3D}$. The density vanishes on and outside of the "Thomas-Fermi surface" given by $V(\vec{r}) = \mu$.

We can also obtain a general result on the relation between the chemical potential and the total number of particles. Since the density (2.14) is non-zero only inside the Thomas-Fermi surface, we only need to integrate it over the "Thomas-Fermi volume" $V_{\rm TF}$ to get the number of particles

$$N = \int_{V_{\rm TF}} {\rm d}^3 r\; n(\vec{r}) = n^{\rm peak}\, V_{\rm TF} - \frac{V_{\rm TF}}{g_{\rm 3D}} \frac{\int_{V_{\rm TF}} {\rm d}^3 r\, V(\vec{r})}{\int_{V_{\rm TF}} {\rm d}^3 r} = V_{\rm TF}/g_{\rm 3D}\,(\mu - \overline{V}). \tag{2.15}$$

Here $\overline{V}$ is the average potential inside the Thomas-Fermi volume. By definition we get $0 < \overline{V} < \mu$. Defining $\alpha = 1 - \overline{V}/\mu$ which depends on the actual trap shape and lies between zero and one, we arrive at the general result

$$N = \alpha\, \mu / g_{\rm 3D}\, V_{\rm TF}. \tag{2.16}$$

Note that $V_{\rm TF}$, $\overline{V}$, and also α (unless $\overline{V}$ is linear in μ) depend on μ.

We generally deal with a harmonic trapping potential or a potential which can be approximated as such. In normal coordinates, with the trap frequencies $\omega_{x,y,z}$ the potential takes the form $V(\vec{r}) = m/2\,(\omega_x^2\, x^2 + \omega_y^2\, y^2 + \omega_z^2\, z^2)$. Thus, the Thomas-Fermi surface is an ellipsoid with half-axes $R_i = (2\mu/m)^{1/2}/\omega_i$.

The enclosed volume is

$$V_{\mathrm{TF}} = \frac{4\pi}{3} R_x R_y R_z = \frac{4\pi}{3} \left(\frac{2\mu}{m}\right)^{3/2} \frac{1}{\omega_x \omega_y \omega_z}. \tag{2.17}$$

The average potential becomes $\overline{V} = 3\mu/5$, and therefore $\alpha = 2/5$ is a constant. From eq. (2.16) we get $N = 2/5\, n^{\mathrm{peak}}\, V_{\mathrm{TF}}$ or in terms of μ

$$N = \mu^{5/2} \frac{8\pi\sqrt{8}}{15\, m^{3/2}\, g_{3\mathrm{D}}} \frac{1}{\omega_x \omega_y \omega_z}. \tag{2.18}$$

2.7 Elementary excitations and collective modes

The elementary excitations of the condensate ground state were investigated by Bogoliubov using a theory of small fluctuations around the ground state and linearizing the solutions for weak excitations. The Bogoliubov excitation spectrum of a homogenous system reads

$$(\hbar\omega)^2 = \left(\frac{\hbar^2 q^2}{2m}\right)\left(\frac{\hbar^2 q^2}{2m} + 2gn\right). \tag{2.19}$$

This corresponds to phonon (collective) excitations $\omega \propto k$ at low momenta and free-particle like excitations $\omega \propto k^2$ at large momenta. The speed of sound for low momenta is

$$c = \sqrt{gn/m}. \tag{2.20}$$

For the harmonically trapped system, the wavelength of low-frequency excitations has a natural cutoff provided by the size of the harmonic trap. Hence the lowest collective modes are quantized oscillation modes in the trapping potential. Using the Thomas-Fermi density distribution

$$n(\mathbf{r}, t) = n_{\mathrm{pk}}(t) \left[1 - \frac{x^2}{R_x^2} - \frac{y^2}{R_y^2} - \frac{z^2}{R_z^2}\right] \tag{2.21}$$

small perturbations around the equilibrium lead to a simple scaling of the cloud radii according to

$$R_i(t) = R_i(0)\, b_i(t) \tag{2.22}$$

and hydrodynamic equations, which can be derived from the time-dependent Gross-Pitaevskii equation result in the equations of motion of the scaling parameters [64, 65]

$$\ddot{b}_i = \frac{\omega_{0i}^2}{b_x b_y b_z\, b_i} - \omega_i^2(t)\, b_i. \tag{2.23}$$

Chapter 3

Fundamentals: Putting a handle on atoms

The achievement of quantum control over positioning, motion, internal states, and interactions of ultracold atoms involves a number of involved experimental techniques, most of which are built upon the interactions of atoms with external fields. In order to lay the foundations for the principal functioning of the apparatus and the experiments discussed in the later chapters, I discuss the fundamentals of the interaction of atoms with light and magnetic fields in this chapter as well as the properties of atoms in periodic potentials.

3.1 Atom-Light Interaction

The techniques to cool atoms to Microkelvin temperatures, to manipulate them in optical lattices, and to detect them are fundamentally based on the principles of light-matter interaction. Near-resonant laser light is used to cool the atoms by the exchange of mechanical energy with photons and the dissipative force resulting from this interaction, and far-resonant light is used to provide conservative potentials with a period of a few hundred nanometer in standing wave laser configurations, so called optical lattices. In this section, I review the fundamentals of light-matter interaction.

Let us consider a strongly simplified atom with only two energy eigenstates $|a\rangle$ and $|b\rangle$ of energies E_a and E_b, respectively. In an external oscillating electric field $\mathbf{E}_{\text{ext}}(t)$ that we treat classically the two-level atom is described by the Hamiltonian

$$H = H_{\text{atom}} + H_{\text{ali}}. \tag{3.1}$$

Here, $H_{\text{atom}} = E_a|a\rangle\langle a| + E_b|b\rangle\langle b|$ is the bare atomic Hamiltonian and H_{ali} is

the interaction Hamiltonian

$$H_{\text{ali}} = -\hat{\mathbf{d}} \cdot \mathbf{E}(\mathbf{r}, t) \tag{3.2}$$

with the dipole operator $\hat{\mathbf{d}} = -e\,\hat{\mathbf{r}}$, where we have used the electric dipole and long-wavelength approximations, which usually are excellent approximations for optical transitions. The matrix elements of the dipole operator $\mathbf{d}$ vanish between states of the same parity. The wave functions of the states of our atom therefore have to be of opposite parity, otherwise our example would be rather uninteresting.

In the basis of eigenstates the dipole operator becomes

$$\mathbf{d} = \begin{pmatrix} |a\rangle & |b\rangle \end{pmatrix} \begin{pmatrix} 0 & \mathbf{d}_{ab} \\ \mathbf{d}_{ba} & 0 \end{pmatrix} \begin{pmatrix} \langle a| \\ \langle b| \end{pmatrix} \tag{3.3}$$

with $\mathbf{d}_{ba} \equiv \langle b|\mathbf{d}|a\rangle$. Note that the Hermiticity of the Hamiltonian necessitates $\mathbf{d}_{ba} = \mathbf{d}_{ba}^*$. This leads to the total Hamiltonian

$$H = \begin{pmatrix} E_a & -\mathbf{d}_{ab} \cdot \mathbf{E}_{\text{ext}}(t) \\ -\mathbf{d}_{ba} \cdot \mathbf{E}_{\text{ext}}(t) & E_b \end{pmatrix}. \tag{3.4}$$

For the electric field we assume a linearly polarized classical light field $\mathbf{E}_{\text{ext}}(t) = \hat{\boldsymbol{\varepsilon}} E_0 \cos \omega t$ with the polarization unit vector $\hat{\boldsymbol{\varepsilon}}$. Plugging that in gives

$$H = \begin{pmatrix} E_a & \hbar\Omega_0 \cos \omega t \\ \hbar\Omega_0^* \cos \omega t & E_b \end{pmatrix} \tag{3.5}$$

with the Rabi frequency $\hbar\Omega_0 \equiv -(\mathbf{d}_{ab} \cdot \hat{\boldsymbol{\varepsilon}})E_0$. We can split up the cosine into two exponentials and pull out $\hbar$ to obtain

$$H = \frac{\hbar}{2} \begin{pmatrix} \omega_a & \Omega_0 \left(e^{i\omega t} + e^{-i\omega t}\right) \\ \Omega_0^* (e^{i\omega t} + e^{-i\omega t}) & \omega_b \end{pmatrix}. \tag{3.6}$$

To diagonalize the Hamiltonian, we switch into a frame rotating at angular velocity ω. In this frame, we obtain a time-independent term given by

$$H_{\text{rot}} = \frac{\hbar}{2} \begin{pmatrix} 0 & \Omega_0 \\ \Omega_0^* & -2\delta \end{pmatrix}, \tag{3.7}$$

where $\delta \equiv \omega - |\omega_b - \omega_a|$ is the detuning from resonance. The other term proportional to $e^{-2\omega t}$ rotates at 2ω and for $|\Omega_0| \ll \omega$ it can safely be neglected ("rotating-wave approximation"), as its effects average out. The eigenvalues are given by $\pm\hbar\Omega/2$, with the generalized Rabi frequency $\Omega \equiv \sqrt{\Omega_0^2 + \delta^2}$,

corresponding to ac Stark shifts of the ground and excited states. In the limit of large detuning, $\delta^2 \gg \Omega_0^2$, the ac Stark shift of the ground state is given by

$$\Delta U \simeq \hbar \frac{\Omega_0^2}{4\delta}. \tag{3.8}$$

The corresponding eigenvectors ("dressed states") are mixtures of the original two basis states. The populations in the two original states undergo Rabi oscillations,

$$P_b(t) = \left(\frac{\Omega_0}{\Omega}\right)^2 \sin^2\left(\frac{\Omega t}{2}\right), \tag{3.9}$$

and $P_a(t) = 1 - P_b(t)$. The state dynamics can also be visualized conveniently on the Bloch sphere [66]. From the steady-state value of P_b it is possible to calculate the spontaneous scattering rate $\Gamma_{\rm sc} = \overline{P_b}\,\Gamma$ (where Γ is the natural line width) in the far-detuned limit $\delta \gg \Omega_0, \Gamma$ as

$$\Gamma_{sc} = \frac{\Omega_0^2}{4\delta^2}\Gamma = \Gamma\frac{\Delta U}{\hbar\delta}. \tag{3.10}$$

One can derive the following important relation between the reduced dipole matrix element D and the transition linewidth Γ (see for example Loudon [67])

$$\Gamma = \frac{\omega_0^3 e^2 D^2}{3\pi\epsilon_0\hbar c^3}. \tag{3.11}$$

The saturation intensity I_s of the atomic transition considered is defined as [50]

$$I_s \equiv \frac{2\pi^2\hbar c\Gamma}{3\lambda_0^3} = \frac{\hbar\Gamma\omega_0^3}{3\times 2^2\pi c^2}, \tag{3.12}$$

where $\lambda_0 = 2\pi c/\omega_0$. With the cycle-averaged intensity $I = c\epsilon_0|\mathbf{E}|^2/2$ one obtains

$$\Omega_0 = \Gamma\sqrt{\frac{I}{2I_s}}. \tag{3.13}$$

In the above treatment we have neglected the counter-rotating term. If the detuning becomes comparable to the atomic transition frequency, the counter-rotating term has to be taken into account. In this case the ac Stark shift of the ground state, or in other words the optical potential, is given by

$$\Delta U = -\frac{\hbar\Omega_0^2}{4}\left(\frac{1}{\omega_0-\omega} + \frac{1}{\omega_0+\omega}\right), \tag{3.14}$$

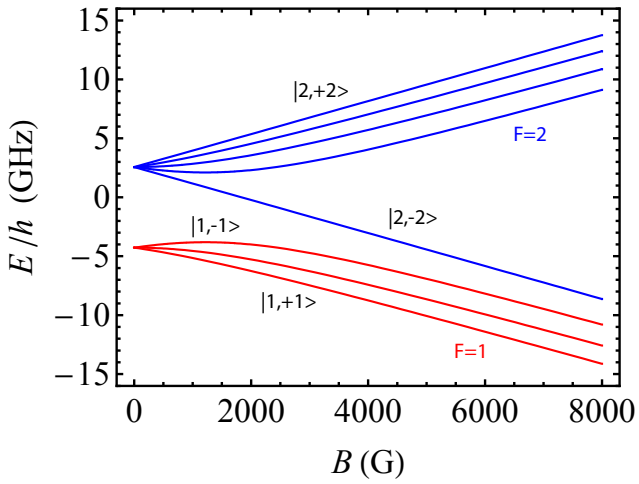

Figure 3.1: Energies of the ground state hyperfine levels of ^{87}Rb as a function of an applied static magnetic field.

and the scattering rate by

$$\Gamma_{\rm sc} = \frac{\alpha^3\omega^3\Gamma^2}{3\times 8\omega_{\rm Ryd}\omega_0}\left(\frac{1}{\omega_0-\omega}+\frac{1}{\omega_0+\omega}\right)^2\frac{I}{I_s} \tag{3.15}$$

which is equal to $\Gamma U_{\rm dip}^{\rm FOR}/\hbar\delta$ when neglecting the "counter-rotating" term.

3.2 Static external magnetic field

An important part of the experimental sequence to produce and manipulate ultracold atomic ensembles is the trapping in inhomogeneous magnetic fields. In order to elucidate the underlying physics, I consider the general case of an atom with total electronic angular momentum $\mathbf{J} = \mathbf{L} + \mathbf{S}$ (L is the orbital angular momentum and S is the spin) and nuclear spin I in a homogeneous magnetic field $\mathbf{B}$. The Hamiltonian of this system is

$$H = -\boldsymbol{\mu}\cdot\mathbf{B} + A\,\mathbf{J}\cdot\mathbf{I}, \tag{3.16}$$

with $\mathbf{F} = \mathbf{J} + \mathbf{I}$, where A is the magnetic dipole hyperfine coupling constant, and $\boldsymbol{\mu} = \mu_B/\hbar\,(g_J\mathbf{J} + g_I\mathbf{I})$.

For the ground state of the experimentally relevant alkalis, which is $^2S_{1/2}$, we have $L = 0$ and $S = 1/2$, so that $\mathbf{J}$ can be replaced by $\mathbf{S}$ and g_J by g_S. In this case the Hamiltonian can be diagonalized analytically, yielding the

so-called Breit-Rabi formula for the eigenenergies [68]

$$W = -\frac{\Delta W}{2(2I+1)} \pm \frac{\Delta W}{2}\sqrt{1 + x^2 + \frac{2m_F}{I+1/2}\,x} + \mu_B g_I m_F B \tag{3.17}$$

with $x = (g_S - g_I)\mu_B B/\Delta W$ and $\Delta W = A(I+1/2)$ is the zero-field hyperfine splitting. The last term is small compared to the others and was neglected in the original paper by Breit and Rabi.

3.3 State-Dependent Optical Potentials

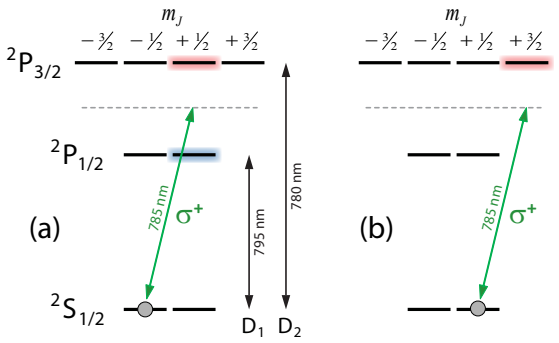

Figure 3.2: Illustration of the basic principle behind state-dependent optical potentials. For clarity, the hyperfine structure is neglected. **(a)** Atoms in the $m_J = -1/2$ state are not affected by σ^+ light at a certain wavelength between the D_1 and D_2 lines where the red and blue-detuned contributions to the light shift cancel exactly. **(b)** Atoms in state $m_J = +1/2$, however, feel an attractive optical potential, since only "red-detuned" intermediate states are accessible. For σ^- light, the roles of the two states are reversed, i.e. only atoms in state $m_J = +1/2$ feel the optical potential (not shown).

The ability to independently control the optical potentials experienced by atoms in different hyperfine states opens up many interesting experimental possibilities. Here, I will focus on the implementation and the properties of state-dependent optical potentials.

The basic idea behind state-dependent optical potentials is to choose the wavelength λ_L and polarization of the trapping or lattice beam such that there are red and blue-detuned contributions from intermediate excited states which cancel for one state of but not for another. This concept is illustrated in Fig. 3.2 for a simplified rubidium atom without hyperfine structure. For

the alkali atoms, one chooses λ_L in between the D_1 and D_2 lines, such that one is red-detuned with respect to the states in the $^2P_{3/2}$ manifold and blue-detuned with respect to $^2P_{1/2}$. Now, from each of the two ground states $m_J = \pm 1/2$ one kind of circularly polarized light ($\sigma^{\mp}$) couples to both red and blue-detuned excited states, while the other kind ($\sigma^{\pm}$) can couple only to the $m_{J'} = \pm 3/2$ states in $^2P_{3/2}$. By choosing the wavelength such that the red and blue-detuned contributions cancel for the transitions where both are present, one can therefore obtain a situation in which $\sigma^{\pm}$ light exclusively affects atoms in the $m_J = \pm 1/2$ ground state [69–71].

In real life, the hyperfine structure splitting leads to additional complications compared to this picture, but the basic principle stays the same. A more serious limitation of this scheme is due to the fact that the D_1 and D_2 lines in ^{87}Rb are only 7 THz apart, such that one cannot arbitrarily reduce residual spontaneous scattering, as the farthest off-resonance one can go is right in the middle between the two lines.[1] In practice, so far, we have not found heating due to spontaneous scattering to be a limiting factor in our experiments. However, the possibility of such heating should be kept in mind.

In the following, I will outline the calculation of state-dependent optical potentials for multi-level atoms, along with scattering and heating rates. After a short discussion of Kapitza-Dirac diffraction as a quick and reliable method for lattice depth calibration, I will present an example of measured lattice depths as a function of polarization for the two hyperfine ground states considered in this work.

3.3.1 Calculation of optical potentials

When an atom is put into a light field that spatially varies in polarization, intensity, or both, the different atomic energy levels experience spatially dependent light shifts, i.e. the so-called optical dipole potential. If the light field is far off-resonant from any atomic transitions ($|\Delta| \gg \Gamma$), the level shifts can be calculated in very good approximation by treating the atom-light interaction as a perturbation to leading order [72]. Thus, for state $|i\rangle$ one obtains the light shift

$$\Delta E_i = \sum_{l \neq i} \frac{|\langle l|\mathbf{d}\cdot\mathbf{E}|i\rangle|^2}{E_i - E_l} = \sum_{l \neq i} \frac{|\mathbf{d}_{li}\cdot\mathbf{E}|^2}{E_i - E_l} \tag{3.18}$$

with the interaction $H_{\text{int}} = -\mathbf{d}\cdot\mathbf{E}$ in the electric dipole approximation, and with the electric dipole matrix elements $\mathbf{d}_{li} \equiv \langle l|\mathbf{d}|i\rangle = \mathbf{d}_{il}^*$. The presence of a

[1] For a quick comparison, the 1064 nm light used for the optical dipole trap is about 95 THz away from the closest resonance, i.e. from the D_1 line. The scattering rate drops as $1/\Delta^2$ where Δ is the detuning.

homogeneous magnetic guiding field that defines a quantization axis and that lifts the residual level degeneracies via the Zeeman shift is implied. As shown in detail in Appendix A, this eventually leads to the optical potential for state $i \in {}^2S_{1/2}$

$$U_{\mathrm{dip}}(\mathbf{r}; i, q) = \frac{3\pi c^2}{2} \left[\frac{\Gamma_{\mathrm{D}_1}}{\omega_{\mathrm{D}_1}^3} \sum_{l \in {}^2P_{1/2}} \frac{\left|c_q^{li}\right|^2}{\omega - \omega_{li}} + 2\frac{\Gamma_{\mathrm{D}_2}}{\omega_{\mathrm{D}_2}^3} \sum_{l \in {}^2P_{3/2}} \frac{\left|c_q^{li}\right|^2}{\omega - \omega_{li}} \right] I(\mathbf{r}), \quad (3.19)$$

where q denotes the polarization of the light ($q = \pm 1$ for $\sigma^{\pm}$ polarization, $q = 0$ for π polarization), $I(\mathbf{r})$ is the cycle-averaged intensity, ω is the frequency of the light, and $\hbar\omega_{li}$ is the energy difference between the atomic levels l and i. The reduced dipole matrix elements have been expressed in terms of the natural linewidths $\Gamma_{\mathrm{D1/D2}}$ and the transition frequencies $\omega_{\mathrm{D1/D2}}$, while the factors c_q^{li} contain the geometrical dependence in terms of Clebsch-Gordan coefficients.

Equation (3.19) can be simplified further, since $\omega_{li} \approx \omega_{\mathrm{D1}}$ for all terms in the first sum and similarly in the second sum. This is a good approximation if the detuning $|\omega - \omega_{li}|$ is much larger than the hyperfine splitting, which is well satisfied for our purposes. The denominators can therefore be pulled out, the sums performed, and with the detunings $\Delta_{\mathrm{D1/D2}} \equiv \omega - \omega_{\mathrm{D1/D2}}$ one obtains [72]

$$U_{\mathrm{dip}}(\mathbf{r}; F, m_F, q) = \frac{\pi c^2 \Gamma_{\mathrm{D2}}}{2\omega_{\mathrm{D2}}^3} \left[\frac{1 - g_F m_F q}{\Delta_{\mathrm{D1}}} + \frac{2 + g_F m_F q}{\Delta_{\mathrm{D2}}} \right] I(\mathbf{r}) \quad (3.20)$$

where m_F is the magnetic quantum number and g_F is the appropriate Landé g-factor of state i (for ^{87}Rb we have $g_F = -1/2$ for $F = 1$, and $g_F = +1/2$ for $F = 2$). Here, we also made use of the fact that $\Gamma_{\mathrm{D1}}/\omega_{\mathrm{D1}}^3 \approx \Gamma_{\mathrm{D2}}/\omega_{\mathrm{D2}}^3$. This simplified form allows for more qualitative insights into the dependence of the potential on wavelength, polarization and internal state. For example, $p \equiv g_F m_F q$ can only take five possible values for ^{87}Rb, namely $p = 0, \pm 1/2, \pm 1$. Accordingly there are only five different equally-spaced potential curves versus wavelength centered around the $p = 0$ curve (see the thin gray curves in Fig. 3.3). For linearly polarized light all ${}^2S_{1/2}$ hyperfine states follow the $p = 0$ curve and experience identical light shifts.

For an optical lattice obtained through complete retro-reflection of an incoming beam of intensity I_{in} and wave vector $k_L = 2\pi/\lambda_L$ along the z direction the resulting spatial intensity distribution is $4I_{\mathrm{in}}\cos^2(k_L z)$. The lattice modulation depth is thus four times as large as the single-beam light shift. In Fig. 3.3 (a), the wavelength dependence of the optical lattice depth is shown for the two chosen hyperfine states $|a\rangle = |1, -1\rangle$ and $|b\rangle = |2, -2\rangle$ as calculated using (3.19). Note that on the scale of the plot the difference compared to the

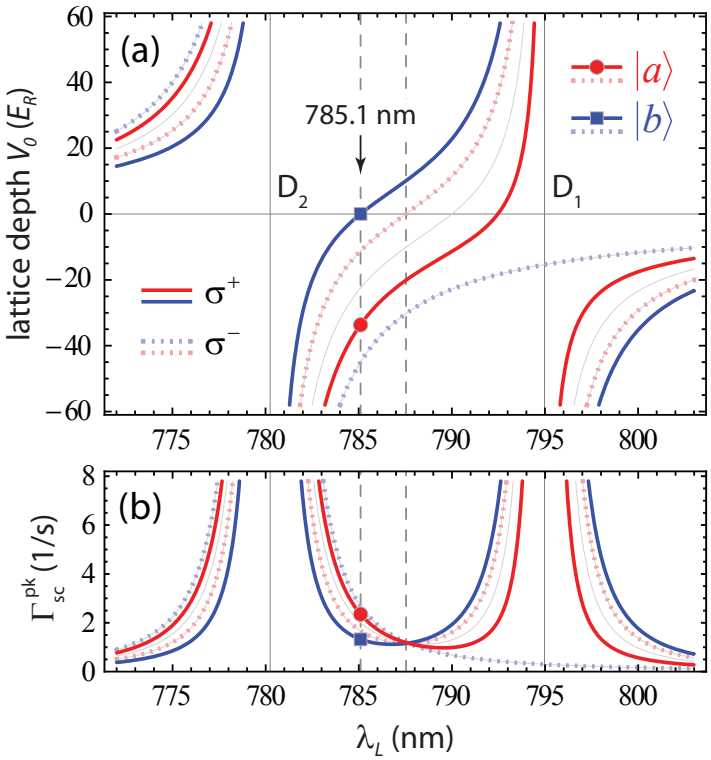

Figure 3.3: **(a)** Calculated lattice depths and **(b)** peak scattering rates $\Gamma_{\rm sc}^{\rm pk} = 4\Gamma_{\rm sc}^{\rm in}$ for the two hyperfine states $|a\rangle = |1,-1\rangle$ and $|b\rangle = |2,-2\rangle$ (red and blue) for σ^+ and σ^- polarized light (solid and dotted) as a function of wavelength (full retro-reflection of an incoming 30 mW beam with a $1/e^2$-radius of 230 μm, yielding $I_{\rm in} = 36.1$ W/cm^2). Negative depths indicate attraction to regions of high intensity (red-detuned character), positive values indicate repulsion (blue-detuned character). At 785.1 nm the optical potential vanishes for $|b\rangle$ atoms in a σ^+ lattice (blue square), while $|a\rangle$ atoms feel a deep lattice potential (red circle, $V_a = 33.6E_R$). The peak scattering rates are 2.35 s^{-1} for $|a\rangle$, and 1.32 s^{-1} for $|b\rangle$ at these settings. The thin gray curves are obtained from the simplified formula showing all five possible values of $g_F m_F q$, as discussed in the text. The dashed line at 787.5 nm represents the center frequency between the D_1 and D_2 lines.

simplified eq. (3.20) (less than 1 %) is not noticeable.

3.3.2 Scattering rates and heating

The scattering rate for a multi-level atom can be obtained by summing over the contributions from each possible excited state similar as in the expressions

for the dipole potential above. Recall that for a two-level atom in the far off-resonant limit one has $\Gamma_{\rm sc} = \Gamma U_{\rm dip}/\hbar\Delta$. This can be applied to each term in (3.20) leading to the expression

$$\Gamma_{\rm sc}(\mathbf{r}; F, m_F, q) = \frac{\pi c^2 \Gamma_{\rm D2}}{2\hbar\omega_{\rm D2}^3} \left[\Gamma_{\rm D1} \frac{1 - g_F m_F q}{\Delta_{\rm D1}^2} + \Gamma_{\rm D2} \frac{2 + g_F m_F q}{\Delta_{\rm D2}^2} \right] I(\mathbf{r}). \quad (3.21)$$

It is interesting to note that the same expression is obtained by a more rigorous derivation using the Kramers-Heisenberg formula [67], which involves summing over all accessible final states. In Fig. 3.3 (b), the calculated scattering rate at the intensity maxima of an optical lattice as a function of wavelength is shown for the two states $|a\rangle$ and $|b\rangle$. For a certain detuning very close to halfway between the D_1 and D_2 lines ($\Delta_{\rm D1} \approx -\Delta_{\rm D2}$), the scattering rate becomes independent of the hyperfine state and the light polarization.

These residual spontaneous emission processes kick the atoms into random directions and therefore result in a diffusion of the atomic momenta or, in other words, heating. Moreover, fluctuations of the dipole force itself also contribute to the overall momentum diffusion [73–75]. The momentum diffusion constant D_p for a (motionless) two-level atom in the far off-resonant, low saturation regime can be written as [75, 76]

$$D_p = \frac{\hbar^2}{2} \frac{3\pi c^2 \Gamma}{2\hbar\omega_0^3} \frac{\Gamma}{\Delta^2} \left[2k_L^2 I(\mathbf{r}) + \frac{1}{2}\nabla^2 I(\mathbf{r}) \right] = \frac{\hbar^2}{2} \left(2k_L^2 + \frac{1}{2}\nabla^2 \right) \Gamma_{\rm sc}^{\rm TLA}(\mathbf{r}) \quad (3.22)$$

where $\Gamma_{\rm sc}^{\rm TLA}(\mathbf{r})$ is just the local scattering rate for a two-level atom in a light field of intensity $I(\mathbf{r})$. The first term proportional to the intensity is due to spontaneous scattering, while the second term proportional to the Laplaceian of the intensity represents the contribution from the fluctuations of the dipole force. The kinetic energy of an atom of mass m increases at the rate $\dot{E} = D_p/m$, also called the heating power [72]. By simply replacing the two-level atom scattering rate in (3.22) by the one for the multi-level atom (3.21) we obtain the heating power

$$\dot{E} = E_R \left(2 + \frac{1}{2k_L^2}\nabla^2 \right) \Gamma_{\rm sc}(\mathbf{r}) \quad (3.23)$$

with the usual recoil energy $E_R = \hbar^2 k_L^2/2m$. For a single beam (i.e. a traveling wave) of intensity $I_{\rm in}$ the heating power is $\dot{E} = 2E_R\Gamma_{\rm sc}^{\rm in}$, since the intensity and thus the scattering rate are spatially homogenous. Each spontaneous scattering event thus increases the energy by $2E_R$, where one recoil energy is due to spontaneous emission and the other one is due to the prior absorption

that is not canceled by induced emission.[2]

Retro-reflection of the beam leads to a standing wave for the dipole potential as well as for the scattering rate $\Gamma_{\rm sc}(\mathbf{r}) = 4\Gamma_{\rm sc}^{\rm in}\cos^2(k_L z)$. The peak scattering rate at the intensity anti-nodes is thus four times as high as for the single-beam case. If there was no contribution from the dipole force fluctuations, the spatially averaged heating power (assuming a homogeneous atom distribution) would be twice as large as for a single beam. However, the Laplaceian term causes "cooling" at the anti-nodes and additional heating at the nodes of the intensity, where the dipole force is largest. In total the heating power becomes $\dot{E} = 4E_R\Gamma_{\rm sc}^{\rm in} = E_R\Gamma_{\rm sc}^{\rm max}$ which actually is still twice as much as for a single beam, but surprisingly is independent of the position in the standing wave [75–77].

It is also noteworthy in the context of state-dependent potentials that even when the dipole potential for a certain state vanishes does the scattering rate remain finite. Although one would not expect the spontaneous contribution to the heating power to vanish, it is somewhat counter-intuitive at first, that also the contribution due to the dipole force fluctuations in a standing wave exists, even when the potential is flat. This flatness, however, comes from the cancellation of possibly deep red and blue-detuned lattices. The dipole force fluctuations thus do not arise from the population fluctuations between ground and excited states in this case, but from the population fluctuations in between red and blue-detuned excited states.

Finally, the heating power due to momentum diffusion $\dot{E}$ can be translated into an actual heating rate $\dot{T}$ [72]. Assuming thermal equilibrium, the mean total energy per atom is a function of temperature. For example, in a three-dimensional harmonic trap one has $E = 3k_BT$, such that the heating rate becomes $\dot{T} = \dot{E}/3k_B$. Consequently, if we shine light onto an atomic cloud sitting in a harmonic trap, the cloud's temperature increases at a rate

$$\dot{T} = 2E_R\Gamma_{\rm sc}/3k_B = \Gamma_{\rm sc}\,T_R/3 \tag{3.24}$$

where the recoil temperature is $T_R \equiv 2E_R/k_B$. For ^{87}Rb and 785 nm light, the recoil temperature is about 360 nK, such that a scattering rate of 1 $\rm s^{-1}$ leads to a temperature increase of 12 nK in 100 ms. Once the thermal energy k_BT becomes comparable to the trap depth, more and more atoms are lost from the trap due to evaporation and the temperature ceases to increase at a constant rate. Retro-reflection of the light to form a lattice would naively cause twice the heating since the heating power is doubled. However, the relation between energy and temperature would not correspond to a simple harmonic trap any

[2] As an aside, the spontaneous force is completely negligible compared to the dipole force in the regime considered here [72, 75].

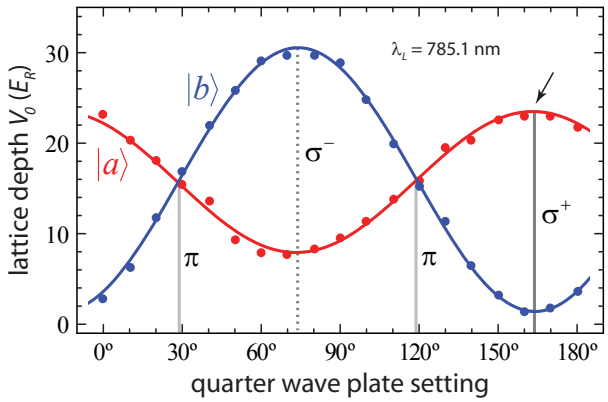

Figure 3.4: Measured lattice depths in a simple retro-reflected beam configuration for the two states $|a\rangle \equiv |1,-1\rangle$ and $|b\rangle \equiv |2,-2\rangle$ as a function of the lattice beam polarization at a given intensity and at a wavelength of 785.1 nm. The lattice depths were obtained separately for each state from Kapitza-Dirac diffraction patterns after a 10 μs lattice pulse. The solid lines are sinusoidal fits [78].

more, at least along the direction of the beam. A more detailed treatment thus seems necessary in this case.

3.3.3 Experimental Lattice Depth Determination

Experimentally determined lattice depths for the two hyperfine states $|a\rangle$ and $|b\rangle$ are shown in Fig. 3.4 as a function of the polarization of the lattice light at constant intensity [78]. The polarization of the incoming beam can be adjusted through a quarter wave plate. Since the lattice is formed by simple retro-reflection of this beam, the polarizations of the two counter-propagating beams are identical. As expected, the lattice depths for both states are the same for linearly polarized light, while circular polarization leads to maximally different lattice depths for the two states considered. In accordance with the theoretical curves in Fig. 3.3 (a), at the chosen wavelength of 785.1 nm the potential for state $|b\rangle$ approximately vanishes[3] for σ^+ light while state $|a\rangle$ is at its maximum lattice depth. Similarly, for a σ^- lattice, $|b\rangle$ experiences a deep lattice potential, while the lattice depth is minimal but non-zero for $|a\rangle$, as expected.

[3]The non-zero lattice depth for $|b\rangle$ at σ^+ polarization in this set of measurements is caused mainly by an imperfect alignment of the magnetic guiding field with respect to the lattice beam. Further details can be found in [78]. With careful alignment, the residual lattice can be reduced down to virtually zero for all practical purposes.

In order to experimentally determine the actual depth of the lattice potential V_0 experienced by the atoms, we generally employ Kapitza-Dirac diffraction [79–81], which we have found to be quick and reliable in comparison to other possible methods [11]. The method consists of pulsing on the optical lattice onto a BEC for a short time τ_{KD} on the order of the recoil time $\tau_R \equiv h/E_R$. The optical lattice acts as a grating from which the BEC is diffracted, very much in analogy to usual diffraction of light from a material grating, just that the roles of light and matter are interchanged. Here, the pulse duration corresponds to the thickness of the material grating in the optics analogy. From the matter-wave diffraction pattern observed after time of flight, one can then determine the modulation depth of the optical lattice.

For typical experimental parameters considered here, the mean-field interaction can be neglected and it suffices to treat the condensate as a homogeneous non-interacting matter wave $\psi(z,t)$ evolving according to the usual Schrödinger equation

$$i\hbar\,\partial_t\,\psi = \left[-\frac{\hbar^2}{2m}\partial_{zz} + V_0\sin^2(k_L z)\right]\psi \tag{3.25}$$

for the duration of the lattice pulse.

If the pulse is sufficiently short, the spatial distribution of the atoms remains essentially unchanged and the gain in kinetic energy is small. However, the optical lattice potential imprints a periodic phase variation onto the condensate. This thin-grating or Raman-Nath regime is attained provided that $\tau_{\mathrm{KD}} \ll T_{\mathrm{ho}}$, where $T_{\mathrm{ho}} = \tau_R/2\sqrt{s}$ (with $s \equiv V_0/E_R$) is the classical oscillation period when approximating each lattice well by a harmonic potential. In this regime, the kinetic energy term in (3.25) can be neglected. The time evolution is then simply given by $\exp\left[-i\,(V_0\tau_{\mathrm{KD}}/2\hbar)\,(1-\cos 2k_L z)\right]$. Use of the identity $\exp(i\,a\cos\phi) = \sum_n i^n J_n(a)\exp(i\,n\phi)$ leads to

$$P_{2n} = |c_{2n}|^2 = J_n^2\left(\frac{V_0\tau_{\mathrm{KD}}}{2\hbar}\right) \tag{3.26}$$

for the population distribution of the even diffraction orders $2n$, where J_n denotes Bessel functions of the first kind. The odd orders remain unpopulated.

More generally, the mode populations can be calculated numerically by integrating the Schrödinger equation. We can expand $\psi(z,t)$ in terms of plane waves propagating along z with multiples of the recoil velocity $v_R = \hbar k_L/m$

$$\psi(z,t) = \sum_{n=-\infty}^{\infty} c_n(t)\,e^{i\,n k_L z}. \tag{3.27}$$

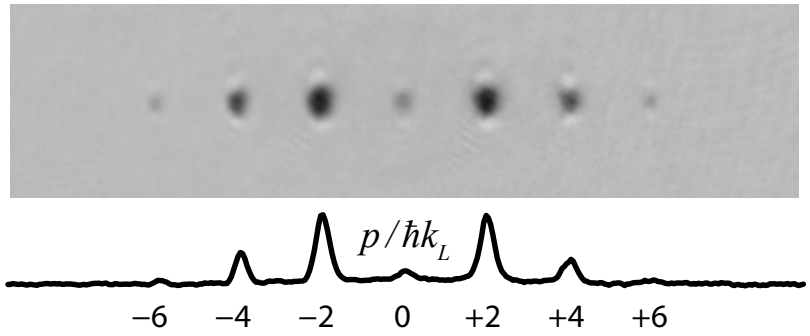

Figure 3.5: Example of a Kapitza-Dirac (KD) diffraction pattern as seen in absorption imaging after time of flight. The different diffraction orders are clearly visible. In the bottom the integrated optical density is shown. The slight variation in the shapes of the different orders is caused by the mean-field repulsion between the atoms that rapidly translates into kinetic energy after release from the trap. (Here, the KD pulse is applied just before the trap is turned off.)

In this basis, (3.25) becomes a system of coupled differential equations for the amplitudes $c_n(t)$

$$i\hbar\,\dot{c}_n = E_R\,n^2 c_n + V_0\left[\,\tfrac{1}{2}\,c_n - \tfrac{1}{4}\,(c_{n+2} + c_{n-2})\right]. \tag{3.28}$$

The initial conditions for Kapitza-Dirac diffraction of a motionless BEC are $c_n(t=0) = \delta_{n0}$, i.e. only the zero-momentum mode is occupied. According to (3.28), the lattice potential only couples momentum modes that are $2\hbar k_L$ apart, and the equations are symmetric under interchange of positive and negative momenta. With the above initial conditions, the mode populations $P_n(t) = |c_n(t)|^2$ will thus be non-zero only for n even, and the distribution will always be symmetric $P_{-n}(t) = P_n(t)$. These general considerations are of course also valid in the Raman-Nath regime. For the determination of lattice depths we do not rely on the Raman-Nath approximation, i.e. we fit numerically integrated diffraction patterns to the experimentally obtained ones. More details on this method can be found in our publication Ref. [81].

3.4 Optical lattice band structure and wave functions in terms of the Mathieu equation

When particles are confined to the periodic potential of a lattice, the usual free-space dispersion relation $E = \hbar^2 k^2/2m$ is dramatically modified. As pointed out by Felix Bloch and others in the early days of quantum mechanics, the dispersion relation becomes periodic in momentum space and energy gaps open up in the energy spectrum. In this section, I will review the fundamental properties of single particles in a periodic potential.

We assume that the lattice potential is formed by a one-dimensional optical standing wave, i.e. an optical lattice, which gives rise to the spatially periodic potential (shown in Fig. 3.6)

$$V(x) = V_0 \sin^2(k_L x), \tag{3.29}$$

with $k_L = 2\pi/\lambda$ and λ the wavelength of the light. With this potential, we can rewrite the Schrödinger equation as a Mathieu equation (in the notation of [82, 83])

$$y''(z) + [a - 2q\cos(2z)]\, y(z) = 0. \tag{3.30}$$

Here the parameter q corresponds to the lattice depth, while a corresponds to the energy as follows

$$q \equiv -s/4, \tag{3.31}$$

$$a \equiv e - s/2 = e + 2q \tag{3.32}$$

with $s \equiv V/E_R$ and $e \equiv E/E_R$, i.e. measuring the lattice depth and the energy in units of the recoil energy. Length is measured in units of $1/k_L = \lambda/2\pi$, and the dimensionless momentum r is measured in units of $\hbar k_L$. For the Mathieu equation exact analytical solutions exist in terms of the Mathieu functions [82, 83].

3.4.1 Energy bands

In the reduced zone scheme, the states are labeled by a pair (n, r_{red}) where n is the band index and $r_{\text{red}} \in [-1, 1)$ is the quasi-momentum. In the expanded or free scheme they are labeled, in principle, only by $r \in \mathbb{R}$. However, for integer values of $r \neq 0$ there are two states of different energy, such that a further

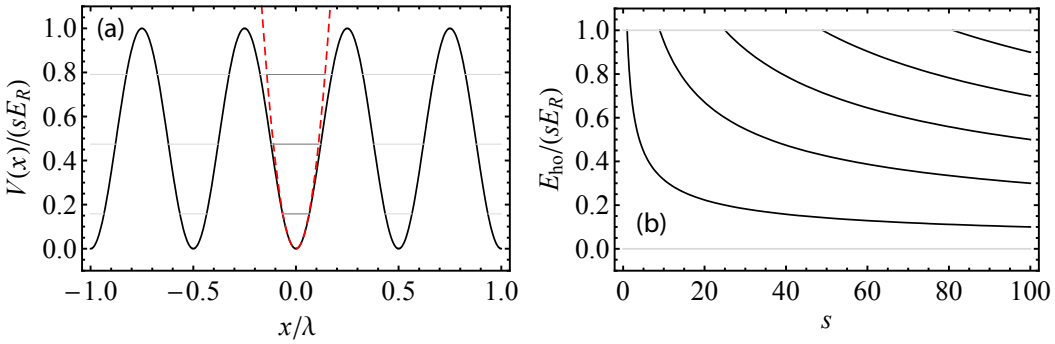

Figure 3.6: **(a)** Sinusoidal lattice potential $V(x)$ as created by an optical standing wave. The dashed red curve shows the approximation by a harmonic potential around the minimum of a single lattice well. Harmonic oscillator (ho) levels are shown for the case of $s = 40$. **(b)** Relative energy of ho levels fitting into a single well, as the lattice depth s is increased. The second level gets pulled in only at $s = 9$, the third at $s = 25$. The harmonic approximation is useful only for ho levels lying sufficiently deep in the well ($E_{\rm ho} \ll V_0 = sE_R$).

distinction at these points is necessary in the expanded scheme[4]. The energy bands are thus given by

$$e(r; s) = a_r(-s/4) + s/2 \qquad r \notin \mathbb{Z} \tag{3.33}$$

everywhere except at the band edges.

3.4.2 Bloch wave functions

According to Bloch's theorem, the wave functions of a particle in a general periodic potential can be written in the form

$$\varphi_r(z) = e^{irz} u_r(z) \qquad \text{with} \quad u_r(z + 2\pi) = u_r(z). \tag{3.34}$$

Note that this does not mean that an arbitrary solution to the Schrödinger equation is of this form, with counter-examples being the even and odd superpositions of two Bloch waves. For the a sinusodial potential, they are given in terms of the even and odd solutions `MathieuC[a, q, z]` and `MathieuS[a, q, z]` provided by *Mathematica* as follows (where C and S basically take the

[4]This distinction is provided by $a_r(q)$ and $b_r(q)$, in Mathematica called `MathieuCharacteristicA` and `...B`, respectively. For given q, these functions coincide everywhere except at $r \in \mathbb{Z}$.

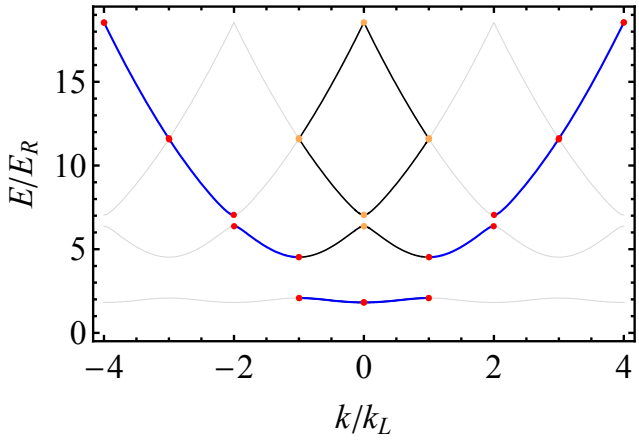

Figure 3.7: Allowed energy bands $E(k)$ of solutions propagating with wave vector k, here at $s = 5$. Shown are the reduced zone scheme (first Brillouin zone only, black), the extended zone scheme (blue, relevant for adiabatic lattice depth changes, cf. band map) and the repeated zone scheme (gray). The band edges are marked by red dots in the extended scheme and orange dots in the reduced scheme.

role of generalized cosine and sine functions):

$$\varphi_{\pm r}(z) = \mathrm{MathieuC}\left[a_r(q), q, z\right] \pm i\mathrm{MathieuS}\left[a_r(q), q, z\right]. \tag{3.35}$$

In the notation of Ref. [82, 83] this is

$$\varphi_{\pm r}(z) = \mathrm{ce}_r(z, q) \pm i\,\mathrm{se}_r(z, q). \tag{3.36}$$

The sign determines in which direction the solution moves completely analogous to a plane wave, to which it reduces for $q \propto s = 0$, i.e. $\mathrm{ce}_r(z, 0) = \cos(rz)$.

3.4.3 Localized basis states – Wannier functions

Localized Wannier functions can be obtained as a superposition of the delocalized Bloch functions. For deep lattices the Wannier functions can be approximated by Gaussians, just as each optical lattice well can be approximated by a harmonic potential of the form $m\omega^2 z^2/2$ (see Fig. 3.9). The trapping frequency (respectively the distance between the harmonic oscillator levels) increases with the lattice depth as

$$\hbar\omega = 2E_R\sqrt{s}. \tag{3.37}$$

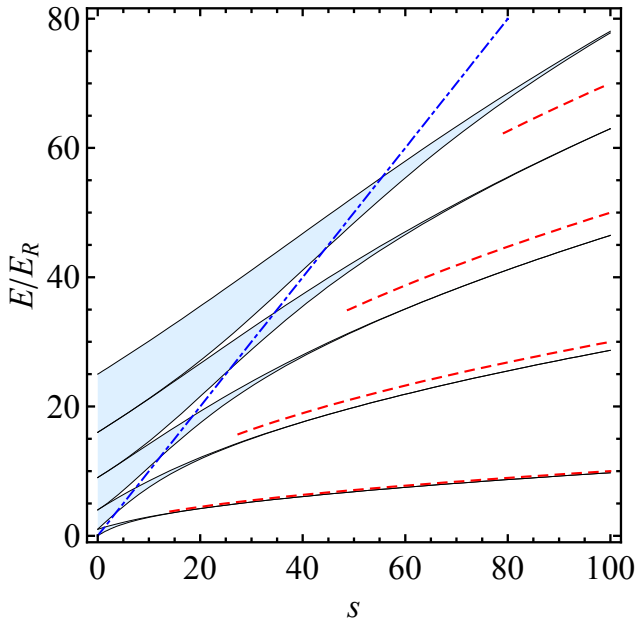

Figure 3.8: The five lowest bands, i.e. the energy ranges where propagating solutions exist, as a function of lattice depth s (shaded light blue). In the gaps between these regions only localized and evanescent wave solutions exist. As the lattice depth is increased, the bands flatten out and approach the harmonic oscillator levels of the single well harmonic approximation shown as dashed red curves. The dash-dotted blue line shows the modulation depth s of the lattice. Naturally, the states above have predominantly free particle character, while they have the character of bound states below.

The size of the wave function on a single site is then just the harmonic oscillator length

$$\sigma = \sqrt{\frac{\hbar}{m\omega}} = \frac{\lambda}{2\pi} s^{-1/4}. \tag{3.38}$$

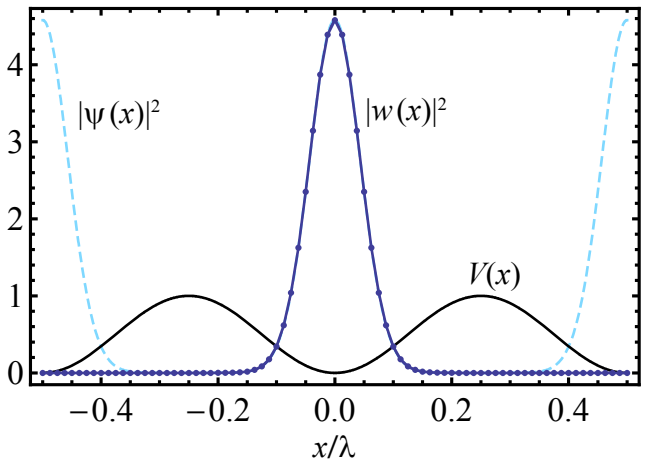

Figure 3.9: Ground state Wannier function $|w_0(x)|^2$ localized at a single site in a lattice potential $V(x)$ of depth $s = 50$. For comparison the density distribution of the delocalized Bloch function $|\psi(x)|^2$ is shown as dashed line.

3.5 Strongly-correlated atoms and the Bose-Hubbard model

In second-quantized notation, the full Hamiltonian for a trapped Bose gas in a lattice potential interacting via an effective contact interaction is given by

$$\begin{aligned} H = &\int d^3r\, \Psi^\dagger(\mathbf{r}) \left[-\frac{\hbar^2}{2m}\nabla^2 + V_{\text{lat}}(\mathbf{r}) + V_{\text{trap}}(\mathbf{r}) \right] \Psi(\mathbf{r}) \\ &+ \frac{1}{2}\,\frac{4\pi\hbar^2 a_s}{m} \int d^3r\, \Psi^\dagger(\mathbf{r})\Psi^\dagger(\mathbf{r})\Psi(\mathbf{r})\Psi(\mathbf{r}). \end{aligned} \tag{3.39}$$

The potentials of the optical lattice and the external trap are typically of the forms $V_{\text{lat}}(\mathbf{r}) = V_0 \left[\sin^2(k_L x) + \sin^2(k_L y) + \sin^2(k_L z)\right]$ for a simple-cubic three-dimensional lattice, and $V_{\text{trap}}(\mathbf{r}) = m\omega^2 r^2/2$ for an isotropic harmonic trap, respectively.

We now expand the field operators $\Psi(\mathbf{r})$ that create or destroy an atom at the point $\mathbf{r}$ in terms of the operators b_{ni} that create or destroy an atom of the band n that is localized at lattice site i, described by the Wannier wave function $\psi(\mathbf{r}) = w^{(n)}(\mathbf{r} - \mathbf{r}_i) = w_i^{(n)}(\mathbf{r})$. Expanding

$$\Psi(\mathbf{r}) = \sum_i w^{(0)}(\mathbf{r} - \mathbf{r}_i)\, b_{0i} \tag{3.40}$$

into the lowest band[5] (in the following $b_{0i} \equiv b_i$), we obtain the Hamiltonian in the Wannier basis

$$H = -\sum_{i,j} t_{ij}\, b_i^\dagger b_j + \sum_{i,j} V_{ij}\, b_i^\dagger b_j + \frac{1}{2}\sum_{i,j,k,l} U_{ijkl}\, b_i^\dagger b_j b_k^\dagger b_l \tag{3.41}$$

with the tunneling matrix elements t_{ij} for tunneling from site i to site j, the matrix elements V_{ij} from the trapping potential that leads to an on-site energy offset, but may also induce directional tunneling (e.g. for a potential gradient), and the general interaction matrix elements U_{ijkl} involving four lattice sites. The matrix elements introduced in (3.41) are given by

$$t_{ij} = -\int d^3r\, w_i^*(\mathbf{r}) \left[-\frac{\hbar^2}{2m}\nabla^2 + V_{\mathrm{lat}}(\mathbf{r})\right] w_j(\mathbf{r}), \tag{3.42}$$

$$V_{ij} = \int d^3r\, w_i^*(\mathbf{r})\, V_{\mathrm{trap}}(\mathbf{r})\, w_j(\mathbf{r}), \tag{3.43}$$

$$U_{ijkl} = \frac{4\pi\hbar^2 a_s}{m}\int d^3r\, w_i^*(\mathbf{r}) w_j^*(\mathbf{r}) w_k(\mathbf{r}) w_l(\mathbf{r}). \tag{3.44}$$

We note that the n^{th}-nearest neighbor tunneling matrix elements $t_{i,i+n}$ can alternatively be obtained as the Fourier coefficients of the dispersion relation in the lattice. In figure 3.10 we show a comparison of the different order tunneling terms for different lattice depths of the optical lattice. For large lattice depths, higher order tunneling is small, such that a simple nearest-neighbor-tunneling tight-binding model is well applicable.

As shown by Jaksch *et al.* in 1998 [14], the full Hamiltonian (3.41) can be significantly simplified yielding the well-known Bose-Hubbard model (BHM) under certain conditions that are easily realizable with ultracold atoms in optical lattices. The Bose-Hubbard model had been used before to describe Josephson junction arrays as realized by superfluid Helium-4 in porous media, for example. Since porous media are irregular structures, early theoretical attention had been focused on the more involved disordered case [84]. The Bose-Hubbard model Hamiltonian with an external trapping potential reads

$$H_{BHM} = -t\sum_{\langle ij\rangle}\left(b_i^\dagger b_j + b_j^\dagger b_i\right) + \frac{1}{2}U\sum_i n_i(n_i-1) + \sum_i V_i\, n_i \tag{3.45}$$

[5] In order to leave the Hamiltonian unchanged, we should use the full expansion including higher Wannier levels or bands $\Psi(\mathbf{r}) = \sum_{i,n} w^{(i)}(\mathbf{r}-\mathbf{r}_i)\, b_{ni}$. However, this would only complicate the notation, and is not necessary for our purposes. One should keep in mind, though, that this projection of H onto the lowest band technically is valid only at very low energies.

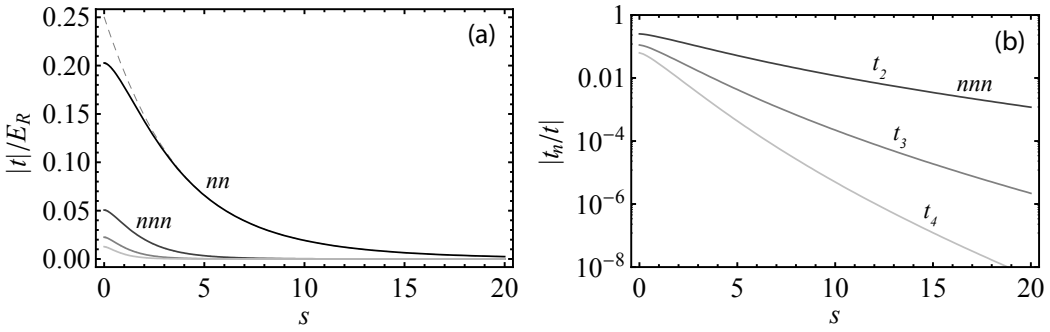

Figure 3.10: (a) Size of the tunneling matrix elements as a function of s, calculated as Fourier coefficients of the dispersion relation of the lowest band. The higher-order matrix elements becoming small corresponds to the band becoming approximately sinusoidal. Then, the nearest neighbor (nn) tunneling t approaches 1/4 of the bandwidth, shown as dashed grey line. **(b)** Magnitude of higher-order tunneling matrix elements $|t_n|$ compared to nearest neighbor tunneling t. (nnn: next nearest neighbor).

where $\langle ij \rangle$ denotes a sum over nearest neighbor links between sites i and j (here the link $\langle 12 \rangle$ is the same as the link $\langle 21 \rangle$, these are *undirected* links, and thus each link appears only once in the sum; note that other conventions are also used in the literature), $n_i \equiv b_i^\dagger b_i$ is the number operator at site i, t is the nearest neighbor tunneling matrix element, $U = g \int d^3r \, |w(\mathbf{r})|^4$ is the on-site repulsion with $g = 4\pi\hbar^2 a_s/m$, and $V_i = \int d^3r \, |w_i(\mathbf{r})|^2 \, V_{\text{trap}}(\mathbf{r})$ is the mean external potential at site i. In order for ultracold atoms in optical lattices to behave according to the BHM (3.45), the following conditions have to be fulfilled:

- nearest-neighbor tunneling has to dominate,
- off-site interactions have to be negligible, only on-site interactions should be sizeable (this and the previous condition require $a_{\text{ho}} \ll \lambda_L/2$),
- the external potential has to change sufficiently slowly on the length scale of the lattice spacing, such that it does not induce tunneling between sites,
- only the lowest band should play a role, excited states should not be populated, the temperature therefore has to be sufficiently close to zero (we have already implied this above by projecting onto the lowest band).

Even without an external potential ($V_i = 0$) the BHM cannot be solved analytically for arbitrary parameter values. One therefore has to resort to analytical

approximations or numerical methods such as exact diagonalization of small systems using the Lanczos algorithm or the increasingly powerful quantum Monte-Carlo (QMC) methods. However, in the two limiting cases of negligible tunneling and of negligible on-site repulsion, H_{BHM} can be diagonalized almost trivially, as discussed in the following. These solutions can then be used as starting points for perturbation theory.

3.5.1 Exact solutions for special cases

Negligible tunneling ($t \ll U$)

In this case ($t = 0$), the Hamiltonian reduces to the on-site repulsion part, and since the sites do not communicate with each other any more, it can be written as a sum over single site Hamiltonians H_i

$$H_{t=0} = \frac{1}{2} U \sum_i n_i(n_i - 1) + \sum_i V_i \, n_i = \sum_i H_i \tag{3.46}$$

with the single-site Hamiltonians

$$H_i = \frac{1}{2} U n_i(n_i - 1) + V_i \, n_i. \tag{3.47}$$

The Hamiltonians are already diagonal in an occupation number basis $|n_i\rangle = \left(b_i^\dagger\right)^{n_i} |0\rangle$ with $n_i = 0, 1, 2, \ldots$. The Hamiltonian summed over all sites is diagonal in the basis $|n_0, n_1, \ldots, n_M\rangle = \prod_{i=0}^{M} \left(b_i^\dagger\right)^{n_i} |0\rangle$.

Negligible on-site interaction ($U \ll t$)

When the on-site interaction is turned off ($U = 0$), we have only the kinetic energy term and the external potential

$$H_{U=0} = -t \sum_{\langle ij \rangle} \left(b_i^\dagger b_j + b_j^\dagger b_i \right) + \sum_i V_i \, n_i. \tag{3.48}$$

For a vanishing external potential this is just a tight-binding Hamiltonian, that can be diagonalized by simply going over to momentum space via a Fourier expansion

$$b_i = \frac{1}{\sqrt{N}} \sum_k b_k \, e(i\mathbf{k} \cdot \mathbf{r}_i). \tag{3.49}$$

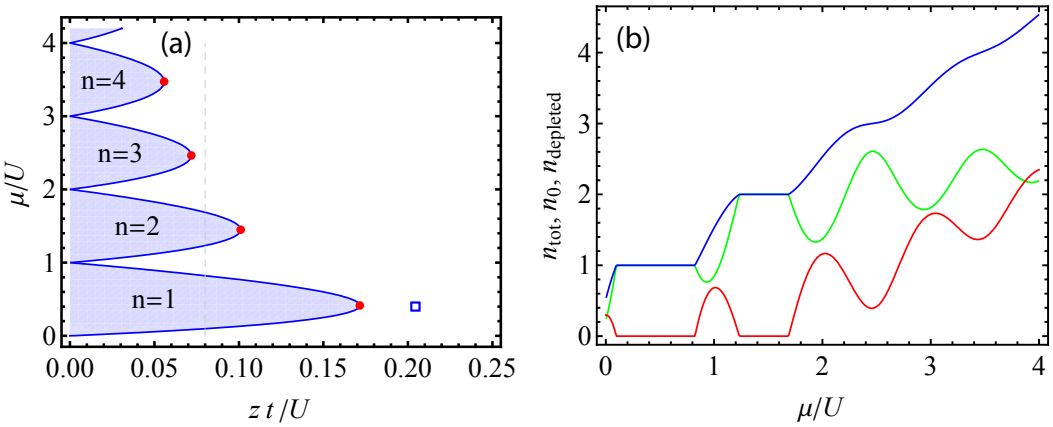

Figure 3.11: **(a)** Phase diagram of the Bose-Hubbard model at $T = 0$ according to the decoupling mean-field approach. The blue shaded regions are Mott insulating with vanishing compressibility and with the atom number per site fixed to an integer. The red dots indicate the critical points at the tips of the Mott lobes. The blue open square indicates the position of the $n = 1$ Mott lobe in 3D determined by quantum Monte-Carlo calculations [85]. **(b)** Atom number per site along the dashed line in (a). *Blue:* Total atom number. The integer filling within the Mott lobes can clearly be seen. *Red:* Expectation value of ψ^2 which gives the number of condensed atoms per site. *Green:* The difference between total and condensed atom number per site, i.e. the number of quantum depleted atoms per site. It coincides with the total atom number only in the Mott insulating regions. Although the condensate fraction is small in between the lobes, the whole system still shows a superfluid response there (similar to the situation in Helium-4 at $T = 0$, which has a superfluid fraction of 100%, while the condensate fraction is only about 10%).

The result is

$$H_{U=0} = \sum_k \epsilon(k)\, n_k \tag{3.50}$$

with the dispersion relation $\epsilon(k) = -2t\cos(ka)$.

3.5.2 Mean-field treatment and $T = 0$ phase diagram

Using a decoupling mean-field approach [86] for the tunneling term, one can determine a phase diagram of the BHM. Essentially, we can write the creation and destruction operators in the kinetic energy term as a sum of a mean value plus a fluctuation operator, $A = \langle A \rangle + \Delta A$. Neglecting terms of higher order

than linear and reexpressing ΔA as $A - \langle A \rangle$ again, we obtain

$$b_i^\dagger b_j \approx \langle b_i^\dagger \rangle b_j + b_i^\dagger \langle b_j \rangle - \langle b_i^\dagger \rangle \langle b_j \rangle = \psi \left(b_j + b_i^\dagger \right) - \psi^2. \tag{3.51}$$

Assuming a homogeneous system, the "mean-field" $\langle b_i \rangle = \psi$ has the same value on each site, and we choose it to be real. It essentially represents the condensate density. For given parameters, we now have to determine the value of ψ that minimizes the system's energy. In this approach, all lattice sites have become equal, such that it is enough to look at a single site with the effective Hamiltonian

$$H_{\mathrm{MF}} = -zt \left(b + b^\dagger \right) \psi + zt\psi^2 + \frac{U}{2} n(n-1) - \mu n, \tag{3.52}$$

where z is the number of nearest neighbors ($z = 2d$ for a cubic lattice in d dimensions). This Hamiltonian can now be diagonalized numerically, yielding the lowest energy for given parameters t, U, z, μ, ψ. Alternatively, one can start from the eigenstates in the $t = 0$ limit and treat the first term in second-order perturbation theory, which leads to analytical forms of the Mott lobe boundaries which differ from the numerical values only by a few percent,

$$B(x) = \frac{(x - \lfloor x \rfloor)\left(\lceil x \rceil - x \right)}{1 + x} \tag{3.53}$$

where $x \equiv \mu/U$, $B \equiv t/U$, and $\lfloor x \rfloor$ and $\lceil x \rceil$ denote the floor and ceiling functions, respectively.

Figure 3.11 (a) shows the $T = 0$ phase diagram, while Fig. 3.11 (b) shows the total number of atoms per site in a cut at constant $zt = 0.08$ as determined using exact diagonalization of the mean-field Hamiltonian, and then using

$$n_{\mathrm{tot}} = -\frac{\partial \langle H_{\mathrm{MF}}(\psi_{\mathrm{min}}) \rangle}{\partial \mu}. \tag{3.54}$$

Also shown is the order parameter $n_0 = \psi^2$, which corresponds to the number of condensed atoms per sites, and the resulting number of quantum-depleted atoms per site $n_{\mathrm{tot}} - n_0$.

Note that the mean-field treatment is most accurate in infinite dimensions, so significant abberations from the exact phase boundaries are expected in one and two dimensions, as verified by QMC calculations, showing that the lobes get pointed tips extending much further out. The $n = 1$ Mott lobe in three dimensions has also been extensively studied for finite temperatures using a numerically exact QMC method [85] (with "numerically exact" meaning that

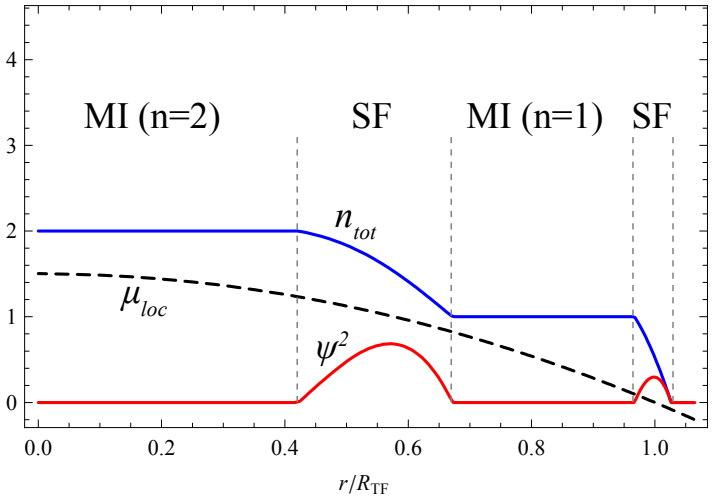

Figure 3.12: Shell structure in an isotropic harmonic trap $V_{\mathrm{trap}}(r) = m\omega^2 r^2/2$. The dashed line is the local chemical potential $\mu_{\mathrm{loc}}(r) = \mu - V_{\mathrm{trap}}(r)$. Here, $zt = 0.08$ and $\mu/U = 1.5$ is chosen such that in the trap center we are in the middle of the $n = 2$ Mott lobe (cf. Fig. 3.11). The $n = 2$ Mott plateau in the center is surrounded by a superfluid shell, an $n = 1$ Mott-insulating shell, and another superfluid shell at the edge.

no uncontrolled approximations have been made and the values obtained can, in principle, be made as close to the exact values as desired given enough computing time). From this study, the tip of the Mott lobe is located at $(U/t)_c = 29.34(2)$ or $(t/U)_c = 0.03408(2)$, as indicated in the figure. To date, much more elaborate versions of the mean-field approach such as dynamical mean-field theory which incorporates site-dependent potentials have been applied, for example, to the disordered BHM [29], and to two-component mixtures [87].

Chapter 4

Experimental Setup

In this chapter I will discuss our newly constructed apparatus for producing magnetically and optically-trapped condensates in a moving-coil transporter scheme [88]. A particularly attractive feature of our apparatus, that reduces the overall complexity of the design, is that the movable quadrupole coils are also used as an essential part of the final magnetic trap, the "McTOP" trap, which belongs to the family of time-averaged orbital potential (TOP) traps [89]. As a stand-alone device, this trap reliably produces condensates with minimal technical complexity. In experiments with optically-trapped Bose-Einstein condensates, the quadrupole coils can be retracted before quantum degeneracy is reached, providing large optical access. The apparatus is well-suited for experiments with optical lattices, as demonstrated by observing the superfluid-to-Mott insulator transition. This chapter is an extended version of our publication Ref. [90].

4.1 Overview of our BEC machine

Our moving-coil transporter apparatus is illustrated in figure 4.1. A cylindrical glass vapor cell is connected to a UHV chamber with an attached small quartz glass science cell (cf. also figure 4.5) through a differential pumping tube. In the vapor cell, we typically collect 7×10^9 atoms in a standard six-beam ^{87}Rb MOT, making use of light induced atom desorption (LIAD) [92–94] to temporarily enhance the loading rate. After an 8 ms molasses phase that lowers the temperature to about 25 μK, the atoms are optically pumped to the $|F = 1, m_F = -1\rangle$ hyperfine ground state, and subsequently caught in a magnetic quadrupole trap using the same coil pair as for the MOT at an axial field gradient of $B'_z = 100$ G/cm, yielding 2.2×10^9 trapped atoms at 150 μK.

The quadrupole coils are mounted on a mechanical translation stage assem-

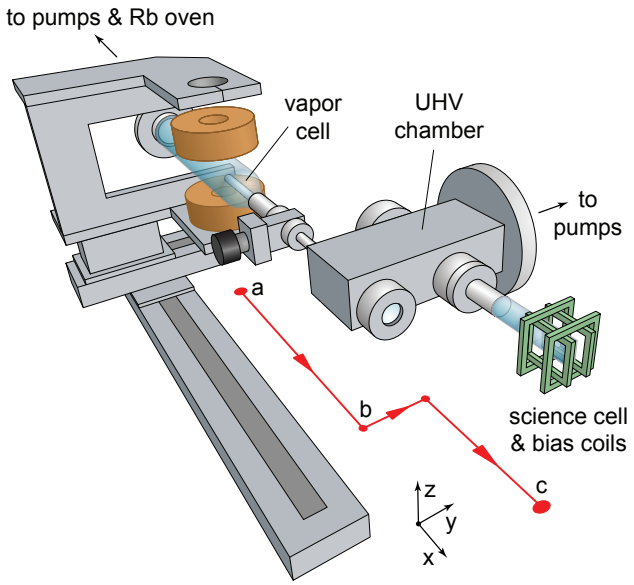

Figure 4.1: Transporter apparatus. The vapor cell is made from a 5.7 cm-diameter Pyrex tube and is connected through valves with an ion pump and a rubidium reservoir (not shown), maintaining a rubidium background pressure of several 10^{-9} torr. A 28 cm-long differential pumping tube of 1 cm inner diameter connects the vapor cell to the UHV chamber and the attached science cell, which are pumped down to less than 10^{-11} torr by an ion pump in combination with a titanium sublimation pump (not shown). The quadrupole coils (shown in MOT position 'a') are mounted on an aluminum holder (sliced to reduce eddy currents) that sits on two orthogonally stacked translation stages (Parker Daedal 404XR) (for details see [91]). The kink in the translation path protects the science cell from fast ballistic atoms escaping from the vapor cell, and it enhances optical access to the condensate along the x-axis. A small gate valve located midway in the pumping tube allows to completely disconnect the two vacuum regions for servicing.

bly [91], which is used to move the magnetically trapped cloud into the science cell. This is done as quickly as possible ($a = 4.5$ m/s^2, $v_{\max} = 0.94$ m/s) in order to minimize losses due to collisions with background gas atoms in the vapor cell. The quadrupole trap is simultaneously compressed to its final value of $B'_z = 350$ G/cm within 150 ms before the cloud reaches the pumping tube. This adiabatically heats up the cloud to 450 μK. We have confirmed that non-adiabatic heating during the motion amounts to less than 10 μK. A detailed study of the transfer in terms of atom number losses and heating can be found in [95].

Once the cloud reaches the UHV chamber 'b', where the measured lifetime

exceeds 150 s, the transporter slows down and proceeds along a kinked path ($a = 0.5$ m/s^2, $v_{\max} = 0.18$ m/s). After a total travel time of 3 s and a covered distance of 66 cm, about 1.6×10^9 atoms, or 75% of the atoms initially caught (see also [95, 96]), arrive in the science cell 'c', where they are evaporatively cooled as discussed in section 4.8.1. We attribute the loss of atoms during the motion to background gas collisions while moving out of the vapor cell, and to a possible shaving off of hot atoms on the walls of the differential pumping tube.

By performing the final evaporation in an optical trap, it is possible to easily use the TOP trap for optical lattice experiments, thus avoiding the usual drawback of TOP traps: atomic micromotion [97] can lead to strong heating due to an oscillatory motion of the atoms relative to the lattice at the frequency of the rotating bias field [98].

4.2 Cooling and Imaging Laser System

Our laser setup, shown schematically in Fig. 4.4, is comparatively simple. All the light used for laser-cooling and imaging is derived from two commercial external cavity diode lasers (ECDLs). Both are locked to atomic transitions using polarization (saturation) spectroscopy [99–101], which directly provides an error signal that can be used for locking without the need for effect modulation or a Pound-Drever-Hall scheme. The cycling light along with the imaging and depump light is generated by a Toptica DL pro ECDL with 60 mW at 780 nm. A tapered amplifier (Toptica BoosTA) provides the necessary power for the MOT and molasses cycling light.[1]

A small fraction of the light is diverted for spectroscopy. The light forked off to lock the lasers to atomic transitions is delivered to the spectroscopy setups via PM fibers. The polarization spectroscopy cells are relatively sensitive to temperature changes, vibrations and magnetic field fluctuations, so that it proved advantageous for stability to place them not directly on the laser table, but into light tight boxes away from the table.

Most beams are coupled into polarization-maintaining fibers which then deliver the light to their destinations. Only the MOT repump and depump

[1] As a historical aside, in the initial stages of the experiment we were struggling with a commercially available 1W tapered diode laser from a competitor. That laser proved to have insufficient frequency stability for reliable absorption imaging (see [95]), and was generally plagued by bad thermal behavior, drifting and several spontaneous laser diode deaths. We were thus forced to image our first condensates on the repumping transition which is not particularly effective, as it is not closed. The reliability of the machine increased considerably after replacing this laser by a DL pro-BoosTA combination.

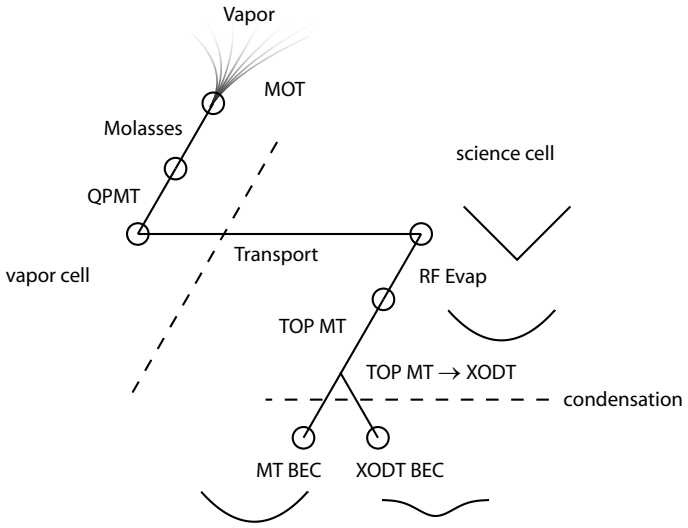

Figure 4.2: Schematic illustration of the steps to BEC in our apparatus. In the room temperature vapor cell, a MOT captures and cools an atomic cloud to μK temperatures. A short optical molasses phase further reduces the temperature, before all laser-light is extinguished and the magnetic quadrupole trap (QPMT) is rapidly turned on to catch the cloud of cold atoms. The magnetic coils of the quadrupole trap along with the cold atoms trapped in it are then quickly moved to the science cell where the ultrahigh vacuum allows for trap lifetimes sufficiently long for evaporative cooling. As evaporative cooling is more efficient in stiffer traps, the first part of the rf-induced forced evaporation is done in the linear potential of the QPMT. Just before losses due to Majorana spin flips at the field zero at the trap center set in, the trap is converted to TOP trap by turning a the rotating bias field, yielding a harmonic potential. Evaporative cooling continues in the TOP trap either until condensation sets in which provides us with a magnetically trapped BEC in the $|1,-1\rangle$ hyperfine state. In the other path taken for our optical lattice experiments, evaporation in the TOP trap is stopped just before condensation sets in. The ultracold thermal cloud is then transferred into a crossed optical dipole trap (XODT), where the final evaporation down to an optically trapped BEC is performed by lowering the trap depth. Although approximately harmonic at the trap bottom the potential in the XODT is anharmonic when moving away relatively little from the trap bottom compared to the TOP trap, especially along the direction of gravity.

beams, which are relatively insensitive to alignment are delivered to the vapor cell as free-space beams (in this case, more power is more important than pointing stability).

For the imaging setup, we took care that the imaging beam paths are mechanically as rigid as possible, such that fringes in the illumination caused by dust and other artifacts do not move significantly between the absorption image and the illumination reference image, greatly improving the quality of our absorption images.

- Acousto-optical modulators are used to rapidly (on the time scale of a few microseconds) control the beam intensity and to shift the frequency of the light.
- Cycler locked to less than 500 kHz using grating and diode current feedback, 187 MHz below the $F = 2 \rightarrow F' = 3$ cycling transition (cf. Fig. 4.3).
- Repumper locked (via grating feedback only) to 80 MHz below the $F = 1 \rightarrow F' = 2$ transition
- The depump beam ($F = 2 \rightarrow F' = 2$) fulfills essentially the opposite role of the repumper by removing all atoms from the cycling transition and accumulating them in the $F = 1$ ground state. (It also can act to partially close the $1 \rightarrow 2$ transition, e.g. for imaging) This is used to optically pump the laser-cooled cloud into the $F = 1$ state before loading it into the magnetic quadrupole trap.
- The power behind the MOT fiber is regulated via a feedback loop that controls how much light the AOM diffracts, very similar to the lattice beams.
- A double-pass AOM configurations for the cycling light which allows for reaching the depump transition with simple 80 MHz AOMs ($3 \times 80 = 240$ MHz) and allows for a larger accessible detuning range of the cycling light (the single-pass AOM frequency change also affects the deflection angle of the light, so in order to cancel this effect a back-reflected double pass configuration is necessary).

4.3 Magnetic Traps and Transporter

4.3.1 Movable Quadrupole Coil Pair

Each of the water-cooled quadrupole coils consists of 33 turns of 1/4 inch-diameter coated hollow copper tubing. At a current of 425 A, the quadrupole coils ($L = 90$ μH) produce an axial field gradient of $B'_z = 350$ G/cm , which can be switched off completely within less than 1 ms using an IGBT.

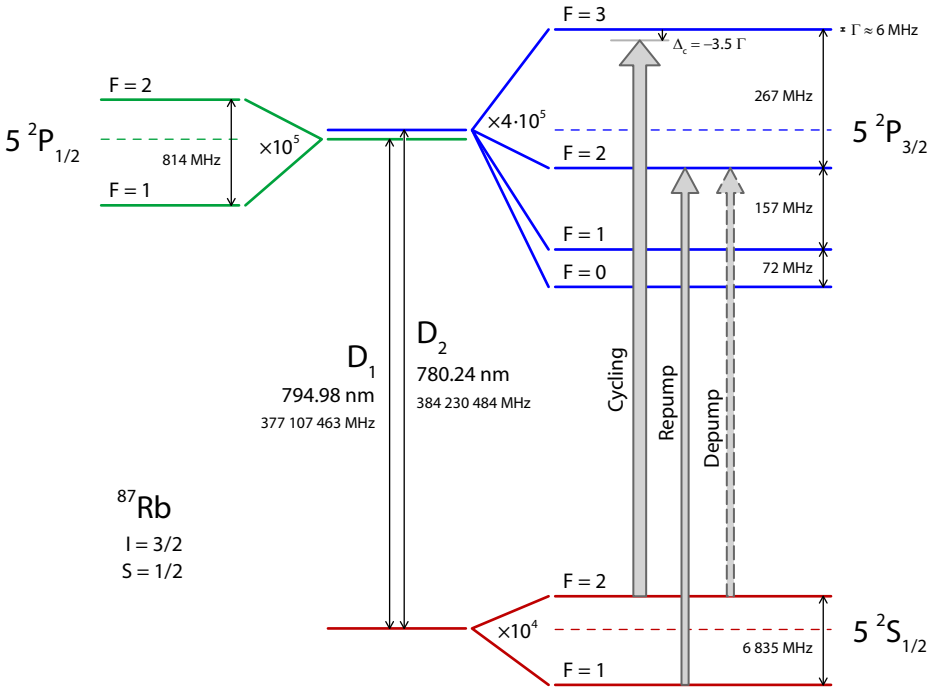

Figure 4.3: Relevant level-structure of rubidium-87 and transitions used for laser-cooling and imaging (to scale, the fine-structure manifolds are magnified by different factors to show the hyperfine structure).

4.3.2 Time-averaged Orbiting Potential Trap

Instead of producing the condensate in a separate Ioffe-Pritchard trap, as generally found in transporter apparatus based on [88], we use the movable quadrupole coils as an integral part of the final magnetic trap. This could be done, in principle, by realizing either a TOP trap [89] or a QUIC trap [102]. For the latter, however, the trap bottom depends on the delicate cancelation of the much larger fields of the quadrupole coils and the Ioffe coil, making the trap very sensitive to fluctuations of their relative positions.

For a TOP trap, the trap bottom is solely determined by the magnitude B_0 of the rotating bias field. It is therefore inherently insensitive to the relative positioning of the coils provided that the bias field is sufficiently homogeneous. With the bias field rotating in the xy-plane, the time-averaged magnetic potential at the center of the trap is given by

$$V(\rho, z) = \mu B_0 + \frac{1}{2} m \omega_\perp^2 \rho^2 + \frac{1}{2} m \omega_z^2 z^2 \quad (\rho, z \ll \rho_0). \tag{4.1}$$

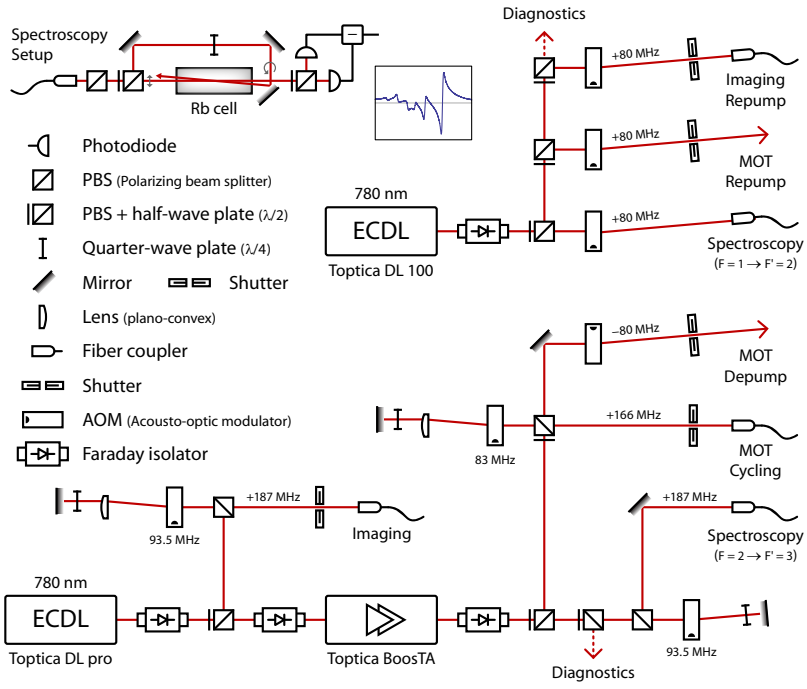

Figure 4.4: Schematic laser setup for laser-cooling and imaging (folding mirrors and components for beam shaping such as fiber coupling lenses are omitted for clarity). Also shown is a spectroscopy setup and an experimental polarization spectroscopy signal when scanning over the transitions involving the ^{87}Rb $F = 2$ level. The largest amplitude line is the $F = 2 \rightarrow F' = 3$ cycling transition which is the lock-point for the cycling laser (see also Fig. 4.3).

Here, m denotes the atomic mass, μ the magnetic moment, and $\rho_0 = B_0/B'_\perp$ is the radius of the "circle-of-death" on which the field-zero is moving [89], where $B'_\perp = B'_z/2$ is the radial quadrupole field gradient. The radial and axial trap frequencies are $\omega_\perp = B'_\perp(\mu/2mB_0)^{1/2}$ and $\omega_z = \sqrt{8}\,\omega_\perp$, respectively. A further advantage of a TOP trap is that magnetic field fluctuations on time scales much slower than the trap frequencies do not affect the trap bottom, unlike for dc magnetic traps. Our "moving-coil TOP trap" (McTOP) is formed by combining the movable quadrupole coils with stationary bias-field coils at the science cell, as illustrated in figure 4.5. We note that a similar strategy has been used in [103] in conjunction with a magnetic waveguide.

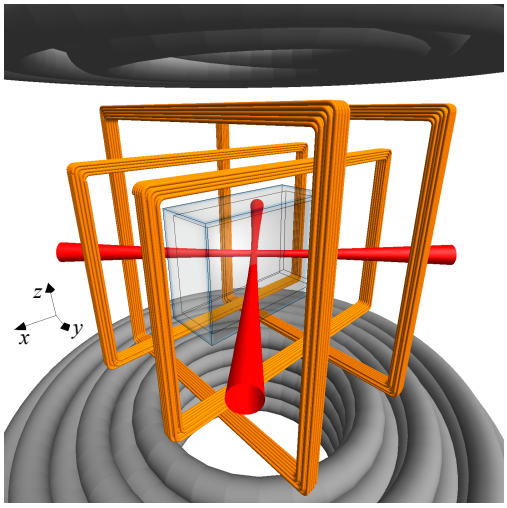

Figure 4.5: Moving-coil TOP trap configuration (McTOP) around the science cell. The rectangular bias-field coils have dimensions of 56 mm×37 mm (inner coils) and 54 mm×54 mm (outer coils), and a center-to-center spacing of 25.5 mm and 29.5 mm, respectively. They are tightly sandwiched between the movable quadrupole coils used for transport (6.0 cm vertical clearance), which each have an inner (outer) diameter of 4.4 cm (11.5 cm) and a height of 4.0 cm. The science cell is a small quartz glass cell with inner dimensions of 10× 20×45 mm^3 and 1.25 mm wall thickness, which is fused to a glass-to-metal adapter (not shown). Also sketched are the laser beams forming the crossed optical dipole trap.

Bias-field coils

The bias-field coils are designed to provide a maximally homogeneous bias field, while minimally obstructing the optical access to the trap center for the given science cell geometry, as shown in figure 4.5. The outer B_x (inner B_y) coils each consist of 25 (20) turns of 24 AWG (0.5 mm-diameter) magnet wire and are wound onto a stiff fiberglass holder structure. Each coil pair produces a field of 7.5 G/A at the center of the trap with a simulated field inhomogeneity of less than $\pm 3 \times 10^{-4}$ within a distance of 1 mm from the center. The air-cooled coils can thermally withstand ac currents of 8 A amplitude for the duration of the evaporation, corresponding to a 60 G bias field and a circle-of-death radius $\rho_0 = 3$ mm at the maximum quadrupole field.

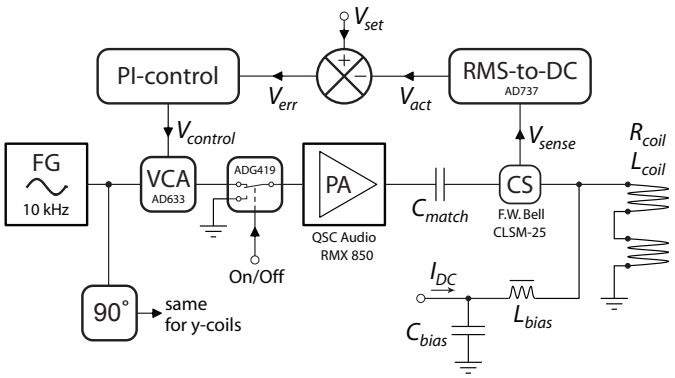

Figure 4.6: Closed-loop bias coil driving circuit (shown for one coil pair). An audio power amplifier (PA) resonantly drives the coils at 10 kHz. The coil current is sensed by a closed-loop Hall-effect current sensor (CS) whose output is converted into a dc voltage $V_{\rm act}$, corresponding to the amplitude of the ac current, by an rms-to-dc converter which determines the regulation bandwidth of about 200 Hz. The error signal $V_{\rm err} = V_{\rm set} - V_{\rm act}$ is fed into an op-amp integrator that acts as a PI-controller and adjusts the gain of the voltage-controlled amplifier (VCA) to counteract any deviations from the desired amplitude $V_{\rm set}$. The ac current can be switched off rapidly with an analog switch. A bias-T allows dc currents to be run through the coils independent of the ac operation, e.g. for earth-field compensation.

AC bias-field coil drivers

To drive the bias-field coils, we use an 800 W audio power amplifier (PA). For each coil pair, the impedance at the 10 kHz driving frequency is minimized down to the ohmic resistance by canceling the inductance with a matching capacitor. The measured inductance of the outer (inner) coil pair is 190 μH (110 μH). The PA can easily supply the ac currents for a 60 G bias field directly into the resulting loads of $\sim 1\ \Omega$, without the need for step-up transformers. The amplitude of the ac current through each coil pair is actively stabilized to within $\sim 10^{-4}$ using the circuit outlined in figure 4.6. The regulation bandwidth of about 200 Hz is more than sufficient for compensating thermal drifts in the coil resistance [2]. The current can be switched off within less than 1 ms limited by the quality factor of the matched coil pair.

[2] An alternative, fast feedback scheme has been described in [104], where the focus is on reducing current noise to improve the coherence time for condensate interferometry in a special TOP waveguide [103].

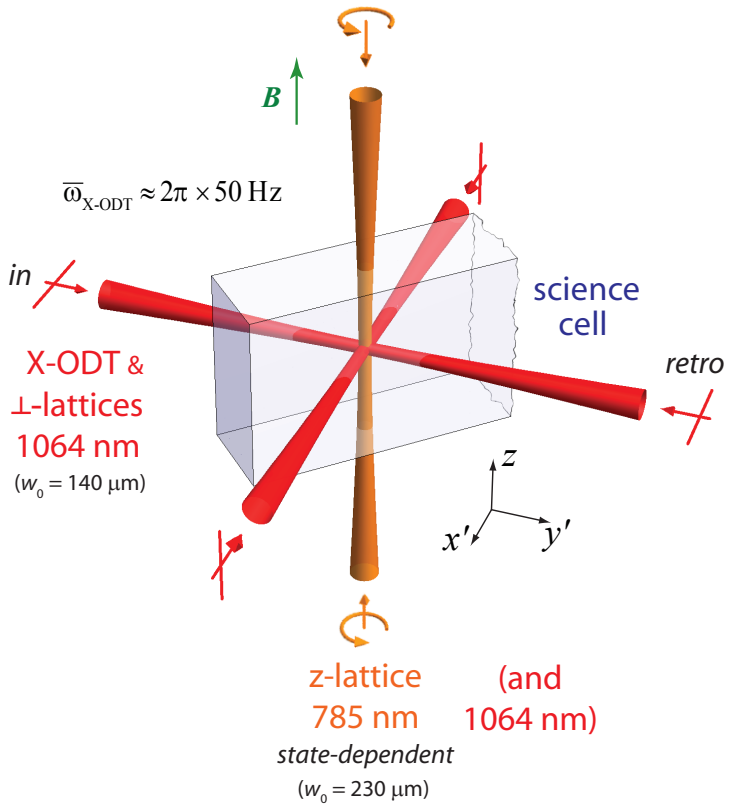

Figure 4.7: Illustration of the dipole trap and lattice beam configuration with respect to the science cell. The two linearly polarized, orthogonal 1064 nm beams in the xy-plane (red) form a crossed optical dipole trap. These two beams can be continuously converted into lattice beams by turning on a retro-reflected beam using a double AOM setup shown in Fig. 4.13. Along the vertical z-axis there is a third state-independent 1064 nm lattice beam, as well as a circularly polarized 785 nm lattice beam that creates a state-dependent optical lattice (orange). The vertical lattices are obtained by simple retro-reflection with a mirror. When using the state-dependent lattice, a small magnetic guiding field is present along the vertical direction. Absorption imaging of the atoms can be performed along both horizontal beam axes.

4.4 Optical dipole trap

The focus of a red-detuned Gaussian beam constitutes the simplest optical trap. The optical dipole potential is essentially proportional to the intensity,

which for a Gaussian beam is given by

$$I(\rho, z) = \frac{2P}{\pi w^2(z)} e^{-2\rho^2/w^2(z)} \tag{4.2}$$

where P is the beam power, and $w(z) = w_0(1 + z^2/z_R^2)^{1/2}$ is the $1/e^2$-radius of the beam, w_0 is the beam waist, i.e. the $1/e^2$-radius at the focus, and $z_R = \pi w_0^2/\lambda$ is the Rayleigh range.

The potential can be expanded around the minimum which yields the harmonic trap frequencies ω_z and ω_ρ. Note that gravity displaces the trap minimum below the point of maximum intensity, and reduces the trap frequency along the vertical direction. Further, there is a critical potential depth below which the trap cannot support the atoms against gravity. The confinement along the beam axis is typically very weak. This can be overcome by adding a second beam perpendicular to the first, thus forming a crossed-beam optical dipole trap.

The beams of our crossed optical dipole trap (cf. figure 4.7) have a $1/e^2$ radius of ~ 135 μm and a combined power of 3 W. They are derived from a single-frequency 1064 nm ytterbium fiber laser (IPG YLR LP-SF series) with a relative frequency offset of 20 MHz to average out interference effects. The maximum depth of the optical trap, including gravity, is 6 μK in the horizontal and 1 μK in the vertical direction, which allows for efficient gravity-assisted evaporation of atomic clouds.

4.5 State-dependent lattice setup

The 785 nm light for the state-dependent optical lattice potential is derived from a Coherent 899 Titanium-Sapphire ring laser that is pumped by a 10 W diode-pumped solid-state laser Coherent Verdi V10 at 532 nm. More details about this laser setup, e.g. a measurement of its line-width by heterodyning it with our cycling laser can be found in [78]. After passing trough an AOM for fast intensity control and a shutter, the light is delivered to the experiment via a polarization-maintaining optical fiber. Behind the fiber, which is also used to provide a clean spatial mode, the polarization is cleaned up with a polarizing beam splitter cube, part of the light is picked up onto a photodiode for intensity stabilization via a PID-controller loop, and the beam is shaped and delivered to the science cell. The polarization can be adjusted manually via a quarter-wave plate situated directly before the beam enters the science cell.

4.6 RF Setup

The setup for the generation of radio-frequency radiation at the position of the atoms is described in detail in [96]. It is used for the forced evaporation in the magnetic quadrupole and TOP traps. Once in optical trap, it is also used for hyperfine state manipulation within the hyperfine state manifolds and for combined microwave and rf two-photon transitions.

4.7 Microwave Setup for Hyperfine State Manipulation

4.7.1 Microwave Generation

The experimental setup for the generation and delivery of microwave radiation to the atoms in the science cell is shown schematically in Fig. 4.8. In the following, I will briefly describe the functions and properties of the individual components.

Microwave synthesizer

The microwave carrier signal is produced by an ultra-low-noise frequency synthesizer module (Microsource SNP-0608-520-02) that is locked to an external rubidium frequency standard (SRS SIM 940). The phase noise performance of the synthesizer module is comparable to high-end microwave generators (e.g. -104 dBc/Hz at 1 kHz away from carrier), but comes at a fraction of the price. The carrier frequency f_c can be programmed via a serial port to anywhere between 6 and 8 GHz with a resolution of 1 Hz. For the experiments presented in this thesis, the carrier was typically set to $f_c = 6827$ MHz.

Mixer and IF modulation signal

In order to achieve fast frequency and amplitude control of the microwave signal, we use a quadrature double-balanced diode mixer (Marki IQ-4509L) to modulate a so-called intermediate frequency (IF) signal f_{mod} onto the microwave carrier. This quadrature (or IQ) mixer in principle allows for extensive control of the amplitude, frequency and phase of the microwave signal with an IF signal bandwidth of up to 500 MHz, if both the in-phase (I) and quadrature (Q) ports are driven separately from a two-channel arbitrary waveform generator. So far, however, we use a simple single-sideband scheme, by feeding the two ports with the same modulation signal, but phase-shifted by 90° for

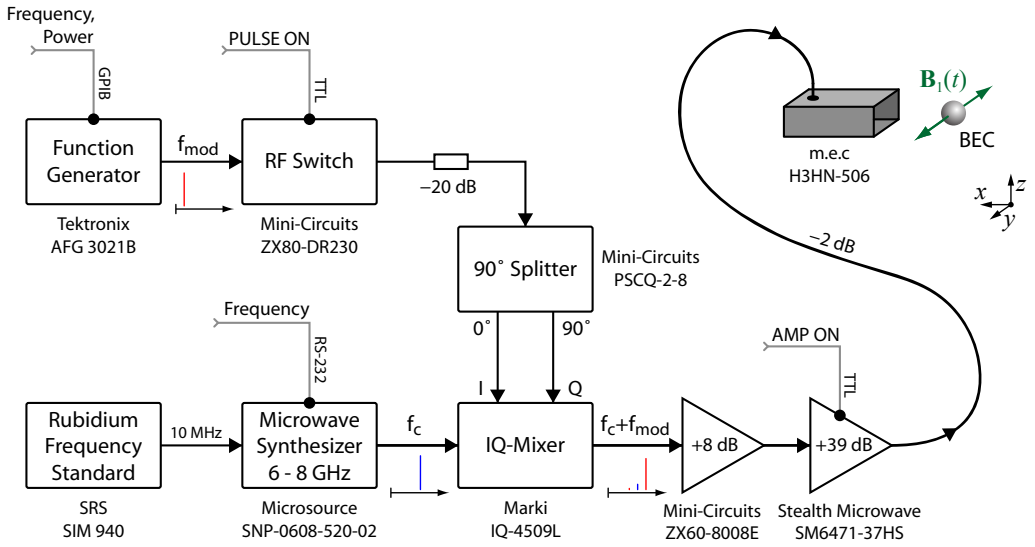

Figure 4.8: Schematic illustration of the experimental setup for the generation and delivery of microwave radiation to the atoms in the science cell.

the Q-port. This is done with a 90° power splitter (Mini-Circuits PSCQ-2-8), which limits the modulation signal frequency to a range from 2 to 8 MHz. The microwave signal thus can be quickly adjusted within the frequency range $f_c + 5 \pm 3$ MHz. Despite being rather narrow, this "instantaneous bandwidth" of 6 MHz has proven sufficient for the small magnetic fields at which we have been working so far, and at which the Zeeman splitting is less than a few MHz. Also, to drive transitions at higher magnetic fields, the carrier frequency can be reprogrammed easily within about 25 ms to center the 6 MHz band around the desired frequency.

With this configuration of the IQ mixer, the IF signal amplitude controls the upper side band (USB) $f_c + f_{\mathrm{mod}}$, while the lower side band $f_c - f_{\mathrm{mod}}$ is rejected by about 33 dB in comparison to the USB. The carrier feed-through is constant and suppressed by about 30 dB. At high modulation signal power, the nonlinear characteristics of the diode mixer become apparent with the power in higher and lower order sidebands growing at the cost of the USB.

The modulation signal f_{mod} is generated by an ordinary function generator (usuallly a Tektronix AFG 3021B) that can be programmed via GPIB. For simple pulse shaping we employ an RF switch (Mini-Circuits ZX80-DR230) providing about 90 dB isolation when off. The rise and fall times are 1 μs and 1.6 μs, respectively.

With the current, low IF frequencies the use of a narrow-band filter after

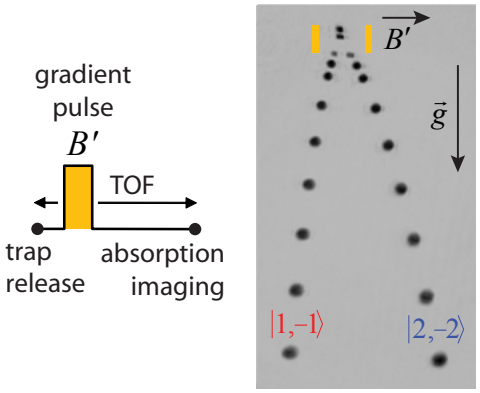

Figure 4.9: Superposition of absorption images taken at different times of flight (TOFs) 2 ms apart after a BEC mixture of the $|1,-1\rangle$ and $|2,-2\rangle$ hyperfine states is released from the trap. The yellow shading indicates the time during which a magnetic field gradient is applied along the horizontal axis. The gradient pulse accelerates the two different components in opposite directions due to their different magnetic moments, which leads to spatial separation during TOF.

the mixer to remove the residual carrier and undesired higher order sideband signals is not possible. They are thus also getting amplified in the following amplifier stages, which reduces the power available for the desired signal, and creates more intermodulation frequency components. These are, however, usually much smaller than the signal unless the mixer saturates.

Amplification

The modulated microwave signal is then sent through a pre-amplifier (Mini-Circuits ZX60-8008E) into a narrow-band, solid-state 5 W linear power amplifier (6.4 to 7.1 GHz, Stealth Microwave SM6471-37HS). The power amplifier can be turned off via a TTL signal (more than 100 dB suppression when off). This is a very useful feature, since even when the modulation signal is switched off, the amplified carrier signal leaking through the mixer is enough to adversely affect the evaporative cooling in the magnetic trap due to parasitic microwave evaporation. The amplifier can be turned on and off within roughly 5 μs and 300 μs, respectively.

Microwave antenna

A 6-feet cable (-2 dB loss) directly connects the power amplifier to the microwave antenna (Microwave Engineering Corp. H3HN-506). The antenna is

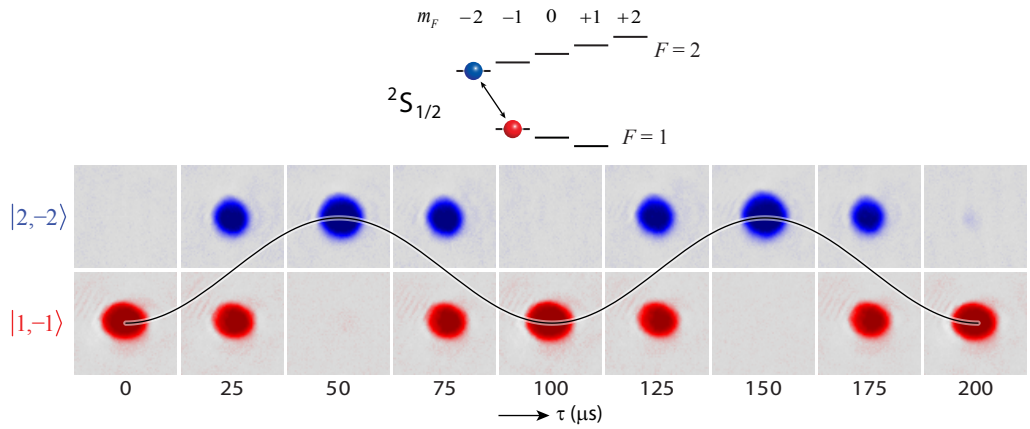

Figure 4.10: Example of Rabi oscillations between the hyperfine states $|1, -1\rangle$ (marked red) and $|2, -2\rangle$ (marked blue) as the microwave pulse duration τ is varied. Shown are absorption images after Stern-Gerlach separation and time of flight. Here, the microwave power was adjusted to yield an on-resonance Rabi frequency Ω_0 of about $2\pi \times 10$ kHz.

essentially a matched sawed-off rectangular waveguide pointing towards the science cell. At the position of the atoms it creates a horizontally polarized oscillating magnetic field. The opening of the waveguide is located about 8 cm away from the position of the atoms. Although a closer position would be possible mechanically, we found that, when the antenna is placed too close, eddy currents around the opening of the waveguide affect the turn-off of the magnetic quadrupole trap and slightly kick the atoms away from the waveguide.

4.7.2 Hyperfine State Manipulation and Detection

The purpose of the microwave radiation produced by the setup just described is to drive magnetic dipole transitions between the two ground state hyperfine manifolds $F = 1$ and $F = 2$. At a vanishing external magnetic field $B_0 = 0$, they are separated by 6834 MHz and are $(2F+1)$-fold degenerate. As discussed in section 3.2, a non-zero magnetic field lifts the degeneracy of the hyperfine levels and for small fields the energy difference between adjacent magnetic sub-levels grows at about 0.7 MHz/G, as illustrated in Fig. 3.1. In order to detect the population of the different internal states we map the internal states to different motional states via Stern-Gerlach separation in a pulsed on magnetic field gradient during time of flight (see Fig. 4.9). The transition frequencies between the different magnetic sub-levels can be calculated analytically with

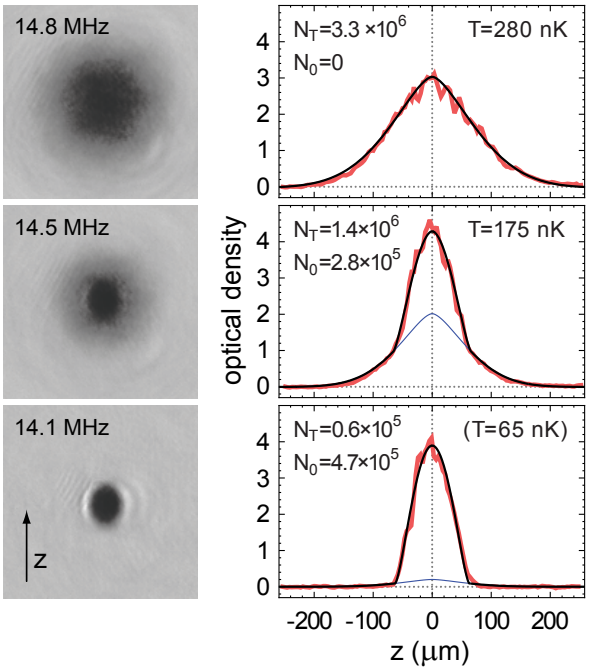

Figure 4.11: Condensate production in the McTOP trap: Phase transition as seen in near-resonant absorption images ($F = 2 \rightarrow F' = 3$) after 16 ms time of flight along with vertical cuts through the density profiles. The data are fitted with the sum of two-dimensional Bose-enhanced Gaussian (thin line) and Thomas-Fermi distributions [8]. Condensation sets in at a critical temperature of (223 ± 12) nK at which the cloud contains $(2.7 \pm 0.4) \times 10^6$ atoms. For the quasi-pure condensate shown, the temperature in brackets is an estimate based on the condensate fraction assuming an ideal Bose gas.

the Breit-Rabi formula (3.17), and close to a particular transition the system can be described as a two-level system, undergoing coherent Rabi oscillations as shown in Fig. 4.10. On resonance, full population transfer occurs and the Rabi frequency becomes minimal at fixed power. From the observed resonance position one can therefore calibrate the magnitude of the magnetic field B_0.

4.8 Condensate production

4.8.1 Condensate production in the McTOP trap

After transport into the science cell, the atom cloud typically contains 1.6×10^9 atoms in the $|1, -1\rangle$ state at a phase-space density of 5×10^{-7}. Forced

radio-frequency (rf) evaporative cooling is initially performed in the stiff linear potential of the fully-compressed quadrupole trap (350 G/cm axial gradient), where it is more efficient until Majorana losses outweigh the advantage of a linear potential [105]. After a 14 s-long linear rf evaporation ramp down to a temperature of 75 μK and an atom number of 7×10^7, the phase-space density has increased to 1×10^{-4} and the lifetime in the quadrupole trap due to Majorana losses has decreased to 35 s. At this point, the trap is converted into a TOP trap by switching on an 18 G rotating bias field, which preserves the atom number to within 15% and the phase-space density to within a factor of two [96]. The resulting harmonic trapping potential has measured trap frequencies of 70.4 Hz in the axial and 25.0 Hz in the radial direction. The trap parameters are held constant for the remaining 30 s of the evaporation sequence, during which another piecewise-linear rf ramp takes the cloud to quantum degeneracy, cf. figure 4.11(a). A detailed description of various evaporation scenarios in the magnetic trap including the one currently used can be found in [96].

Position and Atom Number Reproducibility

We have found the shot-to-shot position reproducibility of the condensate to be consistent with the specified positioning uncertainty of the translation stages ($3\sigma = 3\mu$m) once the system is warmed up, as shown in figure 4.11(b). For this measurement, the condensate was imaged simultaneously along two orthogonal axes in the horizontal xy-plane with resonant absorption imaging on the repump transition $5S_{1/2}(F = 1) \rightarrow 5P_{3/2}(F' = 2)$, immediately after the magnetic trap had turned off. We have not observed any systematic shifts of the condensate position caused by the "dual" imaging itself for the beam intensities used.

During the first 63 of a total of 173 consecutive runs after a cold start, the condensate position drifts by roughly 15 μm, as seen in figure 4.11(b). In the z-direction we find a similar drift of about 7 μm. This initial drift is directly correlated with the slow temperature increase and subsequent stabilization at $\sim$ 75°C of the supply cables (4/0 AWG, i.e. 11.6 mm core diameter) of the quadrupole coils. As the cables warm up, their thick rubber insulation becomes much less rigid, thus changing the mechanical torque exerted on the coil holder. This potential problem can most easily be avoided by pre-warming the cables at high quadrupole coil currents.

We have found the condensate atom number to be stable to within 5-10% depending on the performance of the MOT. For optimized conditions, condensates containing up to 1×10^6 atoms have been observed. No correlations were found between the atom number and the position jitter of the cloud in

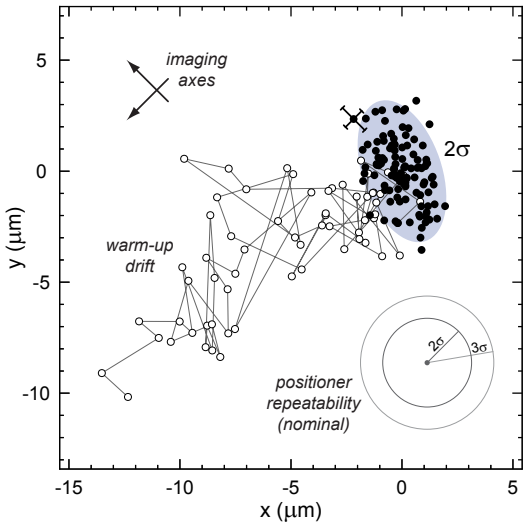

Figure 4.12: Condensate production in the McTOP trap: Reproducibility of the condensate position in the horizontal plane. The filled circles show the in-situ positions of the condensate (as determined from simple Gaussian fits) for the last 110 of a series of 173 runs. The 2σ ellipsoid (shaded) with 95% of the runs has half-lengths of 3.3 μm and 1.8 μm, comparable to the specified repeatability of the translation stages. The open circles represent a warm-up drift during the first 63 runs (see text). The arrows indicate the two imaging directions used, and the error bars indicate the maximum uncertainty in the fits used to determine the condensate position. The radial Thomas-Fermi diameter of the trapped condensate is ~ 40 μm.

the science cell.

4.8.2 Condensate production in the optical trap

For condensate production in an optical trap, the evaporation in the McTOP trap can also be used as "phase-space funnel" to load an optical dipole trap after which the quadrupole coils are moved out of the way. The stationary bias-field coils can then still be used to control the spin quantization axis, for example.

The experimental procedure is as follows. After RF evaporation in the magnetic potential, the atoms are loaded adiabatically into a crossed-beam optical dipole trap formed by two orthogonally intersecting laser beams. This is done by smoothly ramping up the optical potential over 400 ms and then smoothly ramping down the magnetic confinement over another 400 ms. After the transfer, the quadrupole coils are moved back to the intermediate

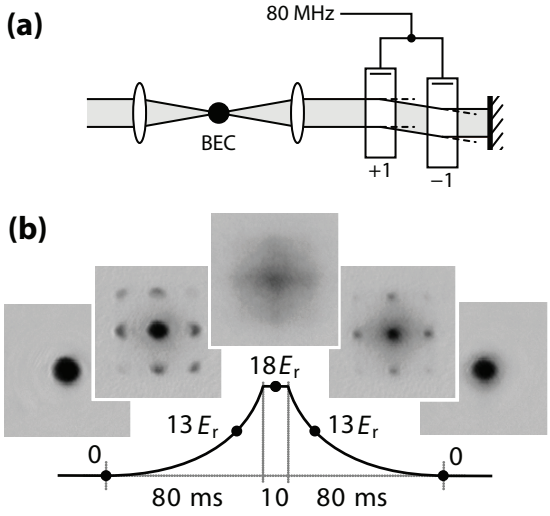

Figure 4.13: All-optical trapping and manipulation of a condensate after transfer from the McTOP trap. **(a)** Conversion of each of the two beams of the crossed dipole trap (cf. figure 4.7) into an optical lattice beam by partial retro-reflection, using a double-pass AOM configuration [106] with zero net frequency shift and rapidly adjustable reflectivity of 10^{-6}-10^{-1}. To realize a three-dimensional lattice, a third beam pair (with full retro-reflection) is added along z. **(b)** Superfluid-to-Mott insulator transition and back in a three-dimensional state-independent optical lattice $(1064\text{ nm})^3$ as observed in absorption images after 18 ms time of flight. The lattice depth follows exponential ramps of 80 ms duration, separated by a 10 ms hold time at a depth of 18 recoil energies E_R (solid line).

position 'b' indicated in figure 4.1.

We typically load the optical trap with clouds at ~ 250 nK and then ramp down the trap depth to 5 μK in the horizontal and 200 nK in the vertical direction where condensation sets in. At this point, the trap is nearly isotropic with measured frequencies between 50 and 60 Hz. The loading procedure results in nearly pure condensates with atom numbers that are within 90% of those reached in the McTOP trap.

4.9 Demonstrating the Superfluid-to-Mott insulator Transition with our Apparatus

By performing the final evaporation in an optical trap, it is possible to easily use the TOP trap for optical lattice experiments, thus avoiding the usual drawback of TOP traps: atomic micromotion [97] can lead to strong heating

due to an oscillatory motion of the atoms relative to the lattice at the frequency of the rotating bias field [98]. To demonstrate the suitability of our apparatus for optical lattice experiments, we have observed a reversible superfluid-to-Mott insulator transition in a three-dimensional (state-independent) optical lattice [13, 14], as shown in Fig. 4.13(b). Since this initial data has been taken, we have improved the quality of our lattice beams and the lattice ramps, such that much cleaner single-component SF-MI transitions can be realized at the time of writing this thesis.

Chapter 5

Interacting Bosonic Mixtures in Optical Lattices

In this chapter, I report the observation of many-body interaction effects for a homonuclear bosonic mixture in a three-dimensional optical lattice with variable state dependence along one axis. Near the superfluid-to-Mott insulator transition for one component, we find that the presence of a second component can reduce the apparent superfluid coherence, most significantly when the second component either experiences a strongly localizing lattice potential or none at all. We examine this effect by varying the relative populations and lattice depths, and discuss the observed behavior in view of recent proposals for atomic-disorder and polaron-induced localization. This chapter is based on our publication Ref. [107].

5.1 Introduction

Bosonic mixtures in optical lattices allow for the study of many interesting topics, such as the two-component Bose–Hubbard model [15–18], as illustrated in Fig. 5.1, with its connection to quantum magnetism [15, 19] (see Fig. 5.2) and models for decoherence mechanisms [20, 21]. In regard to condensed matter physics simulations, the introduction of a second component allows for the investigation of phenomena such as polaron physics [22–24] and phonon-mediated long-range interactions [18, 23], as well as effects of impurities and disorder [25–29].

Recent experiments have addressed heteronuclear mixtures of atoms in optical lattices, both for the boson-boson [108] and boson-fermion [109–111] cases. The superfluid coherence of the heavier bosonic component was universally found to decrease in the presence of the lighter second species, indepen-

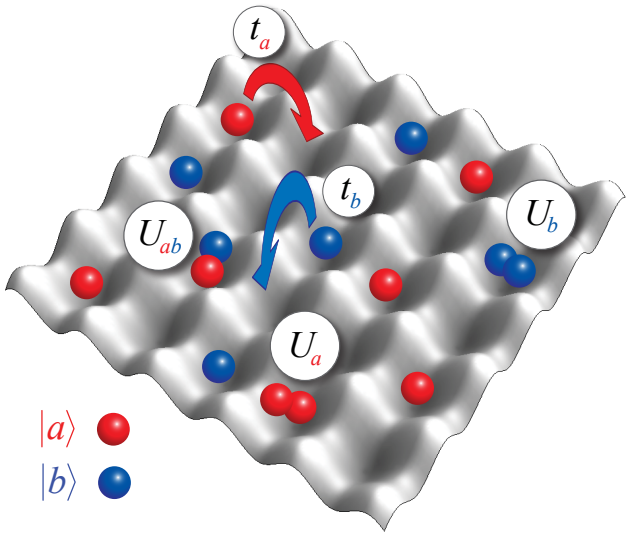

Figure 5.1: Illustration of the two-component Bose-Hubbard model. Here, the two components are realized by two different internal states $|a\rangle$ and $|b\rangle$. Each component has its own tunneling rates t_a and t_b between nearest-neighbor sites, and intra-component on-site repulsions U_a and U_b. Additionally, the two components interact via the inter-component on-site repulsion U_{ab}.

dent of the sign of the interaction, even for small overlap between the components [108]. There exists a number of explanations for the observed behavior, ranging from localization due to impurities [110], self-trapping [111], the formation of composite particles [109], incoherent scattering of phonons [108], to thermalization effects [109] and changes in the chemical potential [112]. Compared to the single-component case, the description of mixtures presents richer physics, but also depends on additional parameters, such as the ratio of the tunneling rates, the interspecies interaction, and the relative atom numbers.

In this chapter we study how the superfluid coherence of bosons in a lattice is affected by a variable bosonic "background" medium. Through a state-dependent optical lattice we can vary the localization of the medium's constituent atoms, and we find a non-monotonic dependence of the coherence properties of the primary species ("foreground atoms") on this localization. For a binary mixture of ^{87}Rb hyperfine states, we demonstrate a reversible state-dependent transition from the superfluid into the Mott regime, and we systematically examine interaction effects by varying both the relative populations and the respective lattice depths. Remarkably, the superfluid coherence decreases not only when the bosons of the medium are strongly localized, but also when they are very delocalized.

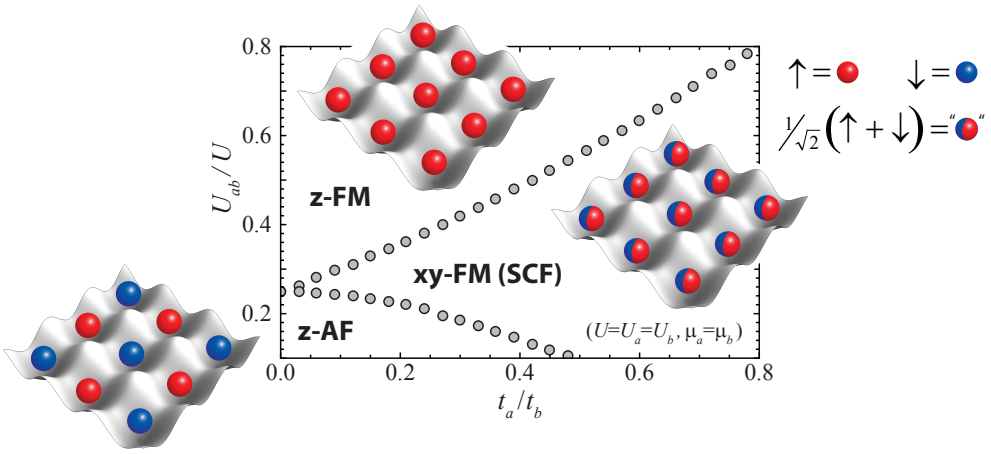

Figure 5.2: Ordered phases of the two-component Bose-Hubbard model in the deep Mott-insulator limit at unit filling ($n_a + n_b = 1$) at $T = 0$ obtained via a simple mean-field ansatz following Ref. [17] (details of the calculation can also be found in [78]). In this limit, the model can be mapped to the spin-1/2 XXZ anisotropic Heisenberg model, and the two types of bosons can be viewed as the eigenstates of a pseudo-spin 1/2. Depending on the tunneling ratio t_a/t_b and the strength of the inter-species interaction U_{ab}, the system favors different "magnetically" ordered phases, such as an easy-axis ferromagnet (z-FM), which corresponds to phase-separation in the particle picture, an Ising antiferromagnet (z-AF) or checkerboard-ordered state, and an easy-plane ferromagnet (xy-FM). In the particle point of view, this last phase is a so-called counterflow superfluid [15], and represents the most interesting of the three magnetic phases shown here.

5.2 Experimental Procedure

Our experimental setup has been described in detail in chapter 4. In brief, we produce a ^{87}Rb Bose–Einstein condensate in the $|F, m_F\rangle = |1, -1\rangle$ hyperfine ground state containing $3 - 5 \times 10^5$ atoms in a crossed-beam optical dipole trap (ODT) at $\lambda_\perp = 1064$ nm, with a mean trap frequency of about 50 Hz. We prepare mixtures of the $|1, -1\rangle \equiv |a\rangle$ and $|2, -2\rangle \equiv |b\rangle$ hyperfine ground states, with variable fractional populations f_a and $f_b = 1 - f_a$, via microwave Landau–Zener sweeps [113]. These mixtures are subsequently loaded into an adiabatically ramped up 3D optical lattice. The state-independent transverse lattice potentials along x and y are generated by partial retroreflection of the ODT beams [90], maintaining constant gravitational sag through coordination of the forward beam intensities with the amount of retroreflection. The state-dependent lattice along z is generated by full retroreflection of a beam at

$\lambda_z = 785.1$ nm ($1/e^2$ radius: 230 μm). At this wavelength (between the D_1 and D_2 lines of ^{87}Rb), the individual depths V_a and V_b of the z-lattice, for $|a\rangle$ and $|b\rangle$, are strongly polarization dependent [69]. A 0.4 G magnetic bias field along z defines the quantization axis. By varying the polarization of the beam from σ^+ to σ^-, we can adjust the ratio V_b/V_a from approximately 0 to 3.5. We characterize the many-body state in the lattice by releasing the atoms and then absorptively imaging both components on the $F = 2 \rightarrow F' = 3$ cycling transition after 18 ms time-of-flight (TOF), concurrent with optical pumping from $F = 1 \rightarrow F' = 2$. Additionally, we use a magnetic Stern–Gerlach pulse to separate the states in TOF.

The use of a homonuclear mixture avoids differential gravitational sag [108] in our far-detuned ODT, and the similarity of all relevant scattering lengths (difference $< 2\%$ [114]) precludes macroscopic phase separation. We characterize component overlap in the ODT using collinear two-component four-wave mixing as a sensitive probe [115]. Residual magnetic field gradients were carefully canceled by maximizing component overlap and inferred to be less than 40 μG/cm from hyperfine Ramsey measurements.

We first demonstrate a state-dependent transition from the superfluid to the Mott regime, keeping the final transverse lattice depth constant at 12 $E_R^\perp$ ($E_R^\perp = \hbar^2 k_\perp^2/2m$, $k_\perp = 2\pi/\lambda_\perp$) and ramping up and down the z-lattice depth[1]. The transverse lattice depth is slightly below the superfluid-to-Mott insulator transition in an isotropic 3D cubic lattice (at a tunneling-to-interaction ratio $t/U \approx 1/36$ [13]), and sufficiently large for undesired four-wave mixing effects in TOF [115] as discussed in section 6.6 to be negligible. Fig. 5.3 shows TOF images for the case $V_a = 4V_b$ and a ramp of V_a up to 15 E_R ($E_R = \hbar^2 k_z^2/2m$, $k_z = 2\pi/\lambda_z$). The $|a\rangle$ atoms undergo a reversible transition into the Mott regime, while the $|b\rangle$ component remains superfluid.

5.3 Visibility and diffraction peak width as coherence measures

To characterize the many-body states of the two components, we analyze the visibility [116] and peak width [117] of their TOF diffraction patterns. As our optical lattice is anisotropic (transverse and vertical axes) in both lattice constant and depth, we employ a single-axis visibility measure along the state-

[1] Our initial attempts with a slightly different lattice loading sequence are described in detail in Ref. [78]. There, however, we were not able to observe any interspecies interaction effects, simply because the two components got vertically separated due to a change in gravitational sag during the lattice ramp up, which we had not considered at that time.

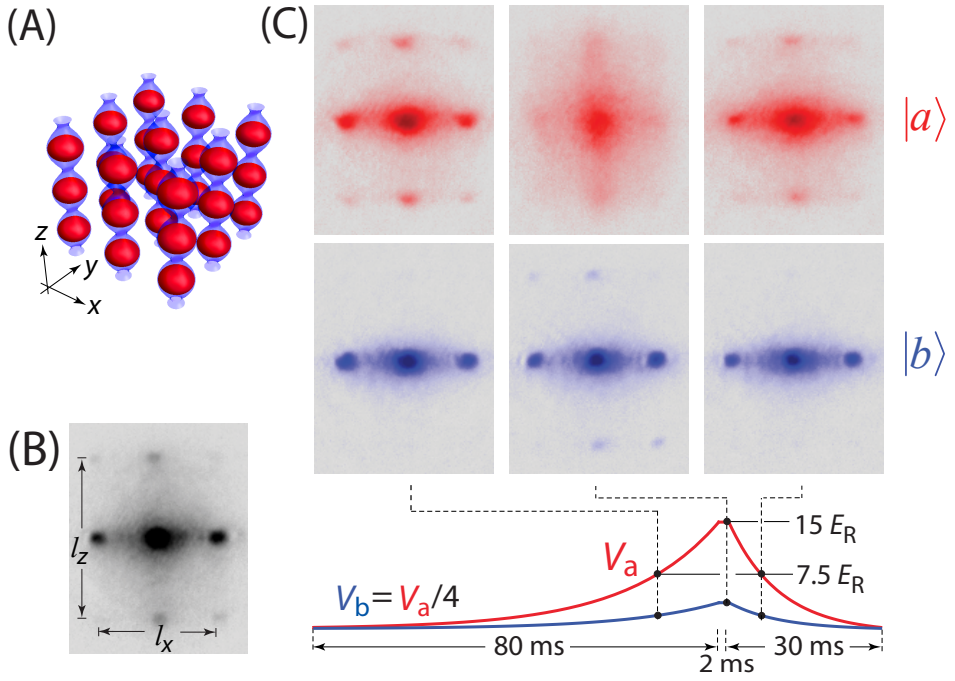

Figure 5.3: State-dependent transition from the superfluid to the Mott-insulating regime. **(A)** Surfaces of equal probability density ($1/e^2$) for non-interacting atoms of type $|a\rangle$ (red) and $|b\rangle$ (blue) in a three-dimensional lattice with depths of 12 $E_R^{\perp}$ in the transverse directions (x, y), and 15 (3.8) E_R along z for $|a\rangle$ ($|b\rangle$) atoms. **(B)** Time-of-flight (TOF) absorption image after release of a balanced mixture ($f_a \approx f_b$). The aspect ratio l_z/l_x is given by $k_z/k_{\perp}$. **(C)** TOF images after Stern–Gerlach separation. The $|a\rangle$ component (red) enters the Mott regime (with $t_a/U_{aa} \approx 1/39$, and $t_{\perp}/U_{aa} \approx 1/38$), whereas the $|b\rangle$ component (blue) remains superfluid. The bottom graph illustrates the state-dependent z-lattice ramp. The transverse lattice ramp (not shown) follows a sigmoid curve of 115 ms duration and reaches its full depth of 12 $E_R^{\perp}$ as the z-lattice goes through half of its maximum depth.

dependent vertical axis. A 600 μs gravitational π-phase shift [13, 118] between adjacent vertical lattice sites produces a symmetric diffraction pattern with two vertical peaks separated by $2\hbar k_z$ (in contrast to the patterns of Fig. 5.3 without a shift). This is accomplished by turning off the ODT while keeping on the z-lattice. The visibility is then defined as $\gamma = N_-/N_+$, where $N_{\pm} = N_{+1} + N_{-1} \pm 2N_0$ are the sum and difference of the atom numbers in the diffraction peaks (N_{+1}, N_{-1}) and intermediate region (N_0), as shown in Fig. 5.4 (I-A). To determine the peak width σ ($1/e$ half-width), we sum over a vertical strip and fit the projection with two Gaussian peaks on top of a broad Gaussian background.

In the following, we examine how the coherence properties of a given superfluid component depend on the presence of a background of either a lighter (in terms of the band mass m_z^*) superfluid, or heavier "impurity" atoms. This is implemented by a halving (I) and doubling (II) of the maximum z-lattice depths as compared to Fig. 5.3. In the first case (I) the background medium is formed by $|b\rangle$ atoms in a 2 E_R deep potential, and in the second case (II) by $|a\rangle$ atoms in a potential with 31 E_R depth. In both cases, the foreground component ($|a\rangle$ atoms in (I), $|b\rangle$ atoms in (II)) experiences an 8 E_R deep lattice, for which the visibility displays a strong differential dependence on lattice depth and tunneling (at the chosen transverse lattice depth of 12 $E_R^\perp$). In both cases, we vary the relative populations f_a and $f_b = 1 - f_a$ of the two components while keeping the total atom number constant, which allows for separating out effects of interspecies coupling from simple overall density effects.

5.4 Delocalized background medium

In case (I) the background density is only weakly modulated by the 2 E_r deep z-lattice, while the foreground atoms are concentrated on lattice sites to a good approximation, but can still tunnel appreciably. The collisional interaction will thus tend to repel background atoms away from sites populated by the foreground atoms, as shown schematically in Fig. 5.5 (A) . The resulting dips in the background density (within a characteristic range given by the mean-field healing length ξ) in turn increase the foreground atoms' localization. This mechanism, similar to self-trapping of impurities in a condensate [22], corresponds to the formation of polarons [23] – composite quasiparticles consisting of individual foreground atoms surrounded by a coherent phonon cloud comprising the background's local mean-field depression. The immersed foreground atoms should thus have an increased effective mass and a lower tunneling than bare foreground atoms, leading to a degradation of the foreground's observed coherence.

Data for case (I) are shown in Fig. 5.4 (I). As the superfluid background of $|b\rangle$ atoms gets more and more populated at the expense of the foreground $|a\rangle$ component, the $|a\rangle$ visibility drops continuously and the diffraction peaks get broader. A reference without background, in which the $|a\rangle$ atom number is correspondingly varied, in contrast reveals a slight increase in visibility with a reduction in $|a\rangle$ atom number, consistent with the naive expectation for a decrease in on-site density. We note that atom transfer from the $|a\rangle$ component to the less localized $|b\rangle$ component lowers the on-site density as well, which naively should also lead to an increase in visibility. The observations thus are not consistent with a simple overall density effect. Additionally, the visibility

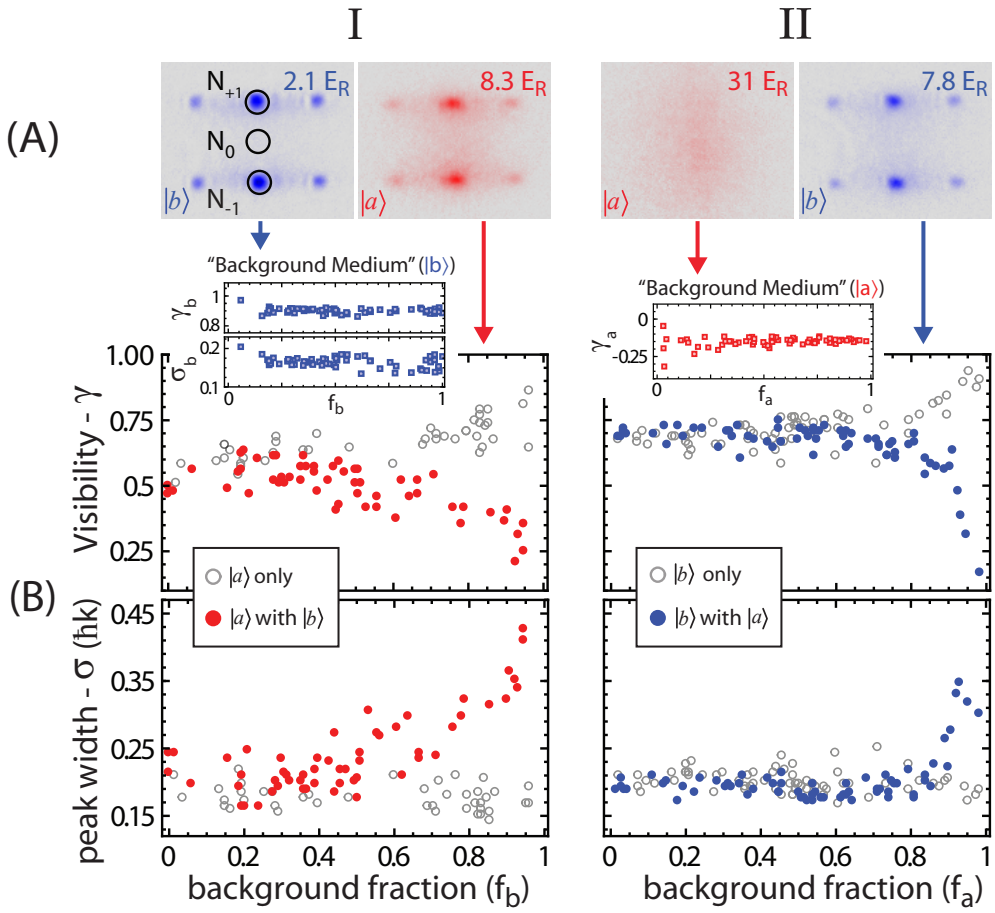

Figure 5.4: Effects of a background medium on the superfluid coherence. (I;left column) $|a\rangle$ atoms ($V_a = 8.3\ E_R$) in contact with superfluid $|b\rangle$ atoms ($V_b = 2.1\ E_R$) and (II;right column) $|b\rangle$ atoms ($V_b = 7.8\ E_R$) in contact with localized $|a\rangle$ atoms ($V_b = 31\ E_R$). **(A)** Stern–Gerlach separated TOF images (for $f_a \approx f_b$) after a gravitational phase shift. The circles in (I) denote apertures used to determine visibility. **(B)** Dependence of the visibility and the peak width on the relative population of the background medium, with constant total atom number $1.7(1) \times 10^5$; the insets show corresponding data for the background medium. The open circles denote reference measurements without background medium, in which the atom numbers are varied correspondingly. All ramp shapes are as in Fig. 5.3, with $V_\perp = 12\ E_R^\perp$.

could in principle be affected by incoherent intra- and interspecies collisions after release from the trap. However, both would similarly degrade the $|b\rangle$ visibility which, as seen in the inset of Fig. 5.4 (I-B), remains at a consistently high value throughout.

The observed reduction of the $|a\rangle$ visibility from $\gamma_a \approx 0.5$ (no atoms in background) to $\gamma_a \approx 0.3$ (95% in background), and the associated increase in peak width, would correspond in the single-component case to a reduction of tunneling by about 40%, as estimated from an independent single-component reference measurement in which the lattice depth was varied. For a single immersed $|a\rangle$ atom, the surrounding dip of the $|b\rangle$ component density leads to an on-site polaronic energy shift $V_p = g_{ab,1D}/\xi \sim 0.2\ E_R$ [23] (where $\xi \sim 200$ nm, $g_{ab,1D} = 2a_{ab}\hbar\omega_\perp$ and $a_{ab} \approx a_{bb} \approx 100a_0$ is the interspecies scattering length), and one can roughly estimate that for the modified on-site potential depth $\sim V_a + V_p$ there is an approximately 5% reduction in tunneling. Therefore, this single-polaron effect alone seems insufficient to explain the observed change in visibility. However, given the large number of $|a\rangle$ atoms even at $f_b = 0.95$, additional localization can be expected due to polaron clustering [23], illustrated in Fig. 5.5 (A), which results from attractive off-site interactions mediated by the superfluid background [18]. The mutual exponential localization of polarons in clusters has been predicted to lead to a broadening of the momentum distribution [23], similar to our observations.

With regard to possible temperature effects, adiabatic loading of bosons into the lowest band of a 3D optical lattice should lead to lower temperatures due to the reduction in band width [119]. Given the unequal z-lattice depths, one thus would expect unequal final temperatures for the two components if loaded separately, leading to thermalization in a mixture [77]. However, thermalizing elastic collisions should be largely suppressed due to the mismatch in band structure [77, 115]. Moreover, the expected temperatures in the lattice are incompatible with the magnitude of the observed effects, even assuming thermalization. Reference measurements with only $|a\rangle$ atoms showed that visibilities below 0.3 require initial loading temperatures exceeding 75 nK, which can be estimated [2] to yield final temperatures above 14 nK. However, for the mixture we start with much lower initial loading temperatures ∼15 nK that should accordingly be reduced to below 4 nK even in the weaker $|b\rangle$ lattice (also, these temperatures $\ll V_p/k_B$ are sufficiently low to suppress effects of thermal phonons on polaron tunneling [23]). We can also exclude trivial heating effects due to spontaneous photon scattering from the state-dependent lattice beam, since the $|b\rangle$ atoms are not only less confined to intensity maxima, but also have a slightly lower scattering rate, so that such heating should be lower for higher values of f_b.

[2] Using $T_f/T_i \sim m/m^*$ [119], with $m^* = \sqrt[3]{m_x^* m_y^* m_z^*}$ for our anisotropic lattice [120]

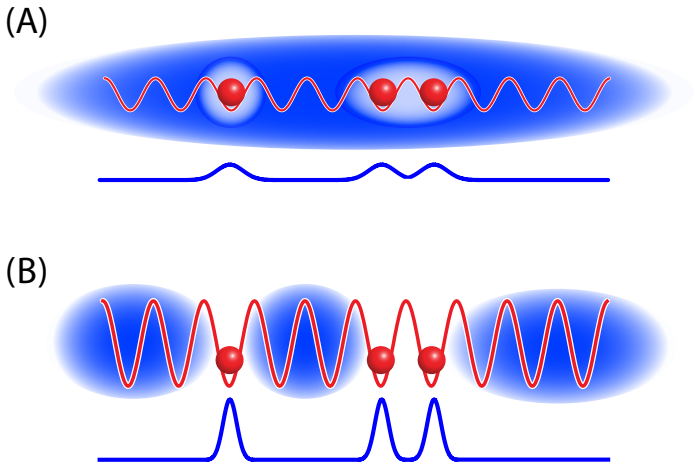

Figure 5.5: **(A)** The delocalized background component (blue) forms a superfluid bath for the foreground atoms (red). Because of the inter-species repulsion a foreground atom creates a region of reduced background density around it, and effectively gets "dressed" by the phonon excitations of the bath, forming a polaron [23]. The tunneling of this polaron is reduced compared to a bare foreground atom since, pictorially speaking, it has to carry the dressing cloud along as it moves through the bath. With the density dip extending over a slightly larger range than the lattice spacing, the foreground atoms should further feel off-site attractive interactions mediated through the background component, which can lead to clustering and localization. Both, reduced tunneling and clustering will reduce the superfluid coherence of the foreground component compared to the single-component superfluid-to-Mott insulator transition. **(B)** The opposite case of a strongly localized background medium, now formed by the red atoms, which act as static local impurities for the blue foreground component. Here, as for the first case, the red curve indicates the optical lattice potential felt by the red atoms, while the blue curve shows the potential seen by the blue atoms through the interaction with the red ones. The random atomic disorder potential can lead to Anderson localization and Bose-glass physics [25], in effect reducing the superfluid coherence of the foreground component, as in the first case. One could think that the red atoms should form a regular, Mott insulating phase instead of a disordered assembly. However, when co-loading two interacting components into a state-dependent optical lattice, in a certain parameter range this can result in a disordered mixture of small droplets of the two components, a so-called "quantum emulsion" [27]. Another interpretation is through a percolation phenomenon [28, 29], i.e. at some point when the impurity density has become large enough, there exists no percolating path connecting the different condensate droplets any more, so that the overall superfluid coherence suddenly disappears.

5.5 Strongly-localized background medium

Observations

We now turn to the case (II) of a superfluid coupled to a background medium that is pinned to the optical lattice. We ramp the z-lattice to $V_{b(a)} \approx 8(31)\ E_R$, for which the $|a\rangle$ component, now playing the role of the background, is deep in the Mott regime. With an increasing background fraction, we again observe a drop in visibility and an increase in peak width of the foreground $|b\rangle$ atoms, as is shown in Fig. 5.4 (II).

Possible causes and interpretations

The observed changes for the $|b\rangle$ component could be caused by a simple increase of on-site interactions due to localized $|a\rangle$ atoms. However, the changes to both visibility and peak width are quite abrupt, which may be indicative of a disorder effect. The simultaneous loading of multi-component gases with differing lattice parameters is predicted to result in a "quantum emulsion state" [27, 112] similar to a Bose-glass, with the less mobile species acting as quasi-static impurities [25], as illustrated in Fig. 5.5 (B). The observed sudden drop could thus be caused by the concentration of localized $|a\rangle$ atoms increasing beyond a percolation threshold, leading to localization of the $|b\rangle$ atoms [28, 29]. Another possible contribution, heating due to spontaneous photon scattering by $|a\rangle(|b\rangle)$ atoms, is measured to amount to less than 14(8) nK for symmetric ramps to 31(8) E_R and back down. However, thermalization (which by the earlier argument should be largely suppressed due to disparate band structures) would not appear to be consistent with the suddenness of the change in $|b\rangle$ visibility and peak width at $f_a \sim 0.8$ for a continuous increase of background $|a\rangle$ population.

5.6 Varying the localization of the background medium

Finally, having studied these two extreme cases, we examine more closely how the interspecies effects depend on the background medium's degree of localization at a fixed background fraction. Using the polarization dependence of our lattice, we keep V_a fixed at 12 E_R while tuning V_b over a wide range, changing the character of the $|b\rangle$ background component from superfluid to localized. Shown in Fig. 5.6 are results for a mixture with $f_b \approx 3/4$. The addition of $|b\rangle$ atoms leads to a reduction of the $|a\rangle$ visibility, most prominently

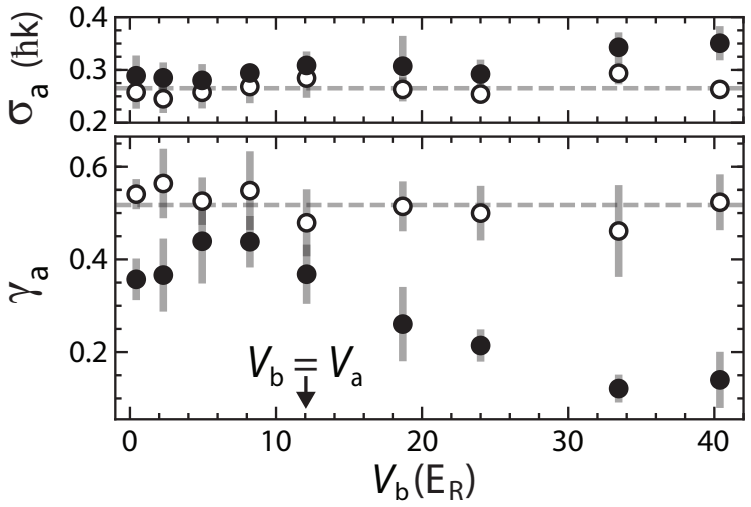

Figure 5.6: Dependence of superfluid coherence on the localization of the second component. Visibility (γ_a) and peak width (σ_a) (filled circles) of the $|a\rangle$ component, with fixed lattice parameters of $V_a = 12\ E_R$ and $V_\perp = 12\ E_R^\perp$, in the presence of $|b\rangle$ atoms ($f_b \approx 3/4$, $N_a + N_b = 3.7(2) \times 10^5$) as V_b is increased. In references (open circles) taken without $|b\rangle$ atoms and with $N_a = 1.0(1) \times 10^5$, the visibility and peak width are roughly constant at 0.52(3) and 0.26(2) (dashed lines). Data points are averaged over 3-5 runs, with statistical error bars shown. Uncertainties in lattice depth are ∼5% (not shown).

when the $|b\rangle$ component is either much lighter or much heavier, in terms of band mass. For $V_b = V_a$, the visibility is lower than in a reference measurement in which only $|a\rangle$ atoms were present, which is most likely caused by the near doubling of the chemical potential due to the increase in overall atom number. We note that the strongest interspecies effects are observed when the background $|b\rangle$ atoms are highly localized, while no effect is observed for a similar background fraction of localized atoms in Fig. 5.4 (II). However, here we have a much greater total population (more than twice that of Fig. 5.4 (II)), so that the concentration of sites occupied by localized background atoms will be greater for a given background fraction, which should enhance the disorder-induced localization of the foreground component as discussed above. In general, the foreground visibility at a given lattice depth should depend on the modified tunneling and on-site interactions due to background atoms, as well as non-trivial effects of clustering and disorder as discussed above. Thus, a determination of where the visibility maximum is located would require a quantitative model for the detailed interplay between these effects.

5.7 Conclusion

In summary, we have studied interspecies effects for a binary bosonic mixture, in a three-dimensional optical lattice with tunable state dependence along one axis. We observe a reduction of apparent superfluid coherence, most strongly for large population imbalances and tunneling rate asymmetries of the two components. The observed reduction in coherence for the addition of both a delocalized and also a localized second species suggest polaron-related effects and atomic-disorder, respectively. Our system should be of interest for future investigations of phonon-mediated interactions in polaron systems and in the spin-boson model.

Chapter 6

Collinear Four-Wave Mixing of Two-Component Matter Waves

We demonstrate atomic four-wave mixing of two-component matter waves in a collinear geometry. Starting from a single-species Bose–Einstein condensate, seed and pump modes are prepared through microwave state transfer and state-selective Kapitza–Dirac diffraction. Four-wave mixing then populates the initially empty output modes. Simulations based on a coupled-mode expansion of the Gross–Pitaevskii equation are in very good agreement with the experimental data. We show that four-wave mixing can play an important role in studies of bosonic mixtures in optical lattices. Our system should also be of interest in the context of quantum atom optics [47]. This chapter is based on our publication Ref. [115].

6.1 Introduction

Four-wave mixing is a fundamental, well-studied concept in nonlinear optics and spectroscopy [30]. Its matter-wave analogue, based on binary collisions in ultracold atomic gases, was first demonstrated experimentally a decade ago [31–33], establishing the field of nonlinear atom optics [34]. In four-wave mixing, two waves form a grating from which a third wave diffracts, thus generating a fourth wave. This process has been used for coherent matter-wave amplification [35, 36], and for the generation of correlated atom pairs [34–38]. Energy and momentum conservation require the magnitudes of all atomic momenta in the center-of-mass frame to be equal which, for atoms in a single internal state, necessitates a two-dimensional geometry [32, 33]. By modifying the dispersion relation with an optical lattice, non-degenerate four-wave mixing of a single species becomes possible also in one dimension [39–41].

Despite considerable theoretical work on atomic four-wave mixing (FWM) with more than one internal state [42–45], experiments have only very recently started to explore possible mechanisms for such FWM [38, 46]. The additional internal degree of freedom allows for degenerate FWM to occur in one dimension, with pairs of waves in different internal states sharing the same momentum mode, opening up possibilities to generate non-classical matter-wave states, e.g. with macroscopic spin entanglement [43, 44]. In this chapter, we demonstrate free-space collinear atomic FWM involving two internal states with distinct, macroscopically populated momentum modes.

Apart from the relevance for quantum atom optics, another important context arises in experimental studies of bosonic mixtures in optical lattices [77, 108, 121]. These systems are of high interest not only in connection with applications to quantum magnetism [15–17], but also for studies of decoherence mechanisms [20, 122], and for lattice thermometry [77, 121]. Most experiments with ultracold atoms in optical lattices to date rely on time-of-flight information. In particular, a sudden release from the lattice projects the band populations onto plane-wave states [123]. We find that for a homonuclear mixture of interacting superfluids, four-wave mixing processes can alter the expected momentum-space distributions, masking or even mimicking in-situ interaction effects.

6.2 Experimental Procedure

In order to induce collinear two-component four-wave mixing, we apply a state-selective optical lattice pulse to a Bose–Einstein condensate containing atoms in two internal states $|a\rangle$ and $|b\rangle$, as illustrated in Fig. 6.1 (A). The pulse induces Kapitza-Dirac (KD) diffraction [79–81] producing recoiling $|a\rangle$ atoms in both positive and negative momentum modes $|\pm 2\rangle \equiv |\pm 2\hbar k_L\rangle$ where $k_L = 2\pi/\lambda_L$, while the $|b\rangle$ atoms remain unaffected. Subsequently, as illustrated in Fig. 6.1 (B), the $|b\rangle$ atoms Bragg diffract from the density modulation formed by the interference of the recoiling $|a\rangle$ atoms $|a, +2\rangle \equiv |a\rangle \otimes |+2\rangle$ with those at rest, $|a, 0\rangle$. Due to momentum exchange collisions, the recoiling $|a\rangle$ atoms are coherently transferred back into $|0\rangle$, as recoiling atoms $|b, +2\rangle$ are produced. This process is formally not distinguishable from coherent (pseudo-) spin exchange. Our system might thus pose an interesting alternative to spinor condensates for the creation of non-classical states [43, 44, 46]. We note that due to the symmetry of the KD pulse, another, independent "copy" of the FWM process occurs on the negative momentum side. For quantum atom optics purposes, this can easily be avoided by using a state-selective Bragg pulse instead, which also allows for extended control of the initial mode pop-

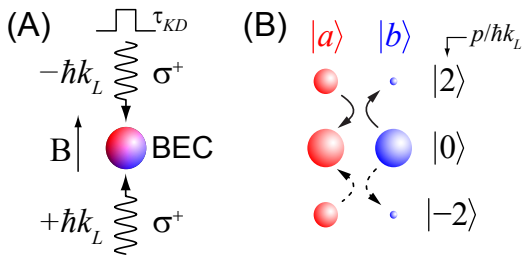

Figure 6.1: Experimental scheme. **(A)** State-selective Kapitza–Dirac diffraction of a two-component Bose–Einstein condensate in hyperfine states $|a\rangle$ and $|b\rangle$, which populates the recoiling modes $|a, \pm 2\hbar k_L\rangle$ while the $|b\rangle$ component remains unaffected. **(B)** Four-wave mixing (solid arrows) with pump modes $|b, 0\rangle$, $|a, 2\rangle$ and seed mode $|a, 0\rangle$ transfers $|b\rangle$ atoms to the output mode $|b, 2\rangle$. Due to the symmetry of the problem, the process also occurs for the modes $|a, -2\rangle$ and $|b, -2\rangle$ (dashed arrows).

ulations. In the present work, however, we are content with applying a KD pulse, mainly out of technical convenience.

Our experimental setup has been described in detail in Ref. [90]. In a crossed-beam optical dipole trap at 1064 nm wavelength, we produce nearly pure ^{87}Rb Bose–Einstein condensates in the $|a\rangle \equiv |F = 1, m_F = -1\rangle$ hyperfine state typically containing about 1.6×10^5 atoms. The trap is approximately isotropic with a mean trap frequency around 50 Hz and an alignment-dependent vertical frequency $\omega_z/2\pi$ between 40 and 50 Hz. We then apply a microwave Landau–Zener sweep to transfer a variable fraction of the condensate into the $|b\rangle \equiv |2, -2\rangle$ hyperfine state [113]. Immediately afterwards, a state-selective lattice beam [69, 70] of wavelength $\lambda_L = 785.1$ nm is pulsed on along the vertical z-direction ($1/e^2$ radius 230 μm) for a time τ_{KD}. The polarization of the light (σ^+) is chosen such that only the $|a\rangle$ atoms feel the optical lattice potential formed through retro-reflection of the beam. A small magnetic field of $\sim$0.4 G along the beam axis defines the quantization axis. After release from the trap and a few milliseconds of free evolution, during which the FWM occurs, a magnetic field gradient (Stern–Gerlach pulse) spatially separates the two hyperfine states along the horizontal x-axis for detection. Finally, the atoms are imaged along the y-axis after a total time of flight of 15 ms by a 100 μs long pulse of near-resonant $F = 2 \rightarrow F' = 3$ imaging light, combined with $F = 1 \rightarrow F' = 2$ repumping light, which ensures equal detection efficiencies for both hyperfine states.

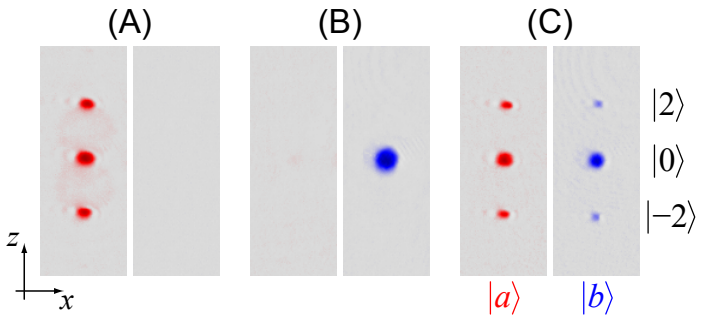

Figure 6.2: Typical absorption images taken after application of the state-selective Kapitza–Dirac pulse ($\tau_{KD} = 25$ μs, $V_a = 6$ E_R), 15 ms time of flight and Stern–Gerlach separation along x, for the case of **(A)** only $|a\rangle$ atoms present ($f_a = 1$), **(B)** only $|b\rangle$ atoms ($f_a = 0$), and **(C)** equal populations of both components ($f_a = 0.5$).

6.3 Results

In Fig. 6.2, typical absorption images are shown for three different fractions of $|a\rangle$ atoms $f_a \equiv N_a/N$. The KD pulse duration (25 μs) and the lattice depth V_a for atoms of type $|a\rangle$ (6 E_R, where $E_R = \hbar^2 k_L^2/2m$ is the recoil energy), are chosen such that half of the population of $|a\rangle$ atoms is diffracted into $|\pm 2\rangle$, while higher orders remain largely unpopulated. By analyzing single-component diffraction patterns [81], we have determined the lattice depths for each component, confirming that atoms of type $|b\rangle$ experience $< 5\%$ of the lattice depth seen by the $|a\rangle$ atoms. On their own, the $|b\rangle$ atoms therefore are not affected by the lattice pulse, as shown in Fig. 6.2 (B). However, when both components are present, a significant fraction of $|b\rangle$ atoms is transferred into the $|\pm 2\rangle$ momentum modes (Fig. 6.2 (C)).

We have measured the amount of diffracted atoms in each state as a function of f_a. As shown in Fig. 6.3, the fraction of diffracted $|b\rangle$ atoms $(N_{b,+2} + N_{b,-2})/N_b$ monotonically increases from zero towards a maximum as f_a is increased, consistent with the picture that the grating formed by interference of the $|a, 0\rangle$ and $|a, \pm 2\rangle$ modes, from which the atoms in $|b, 0\rangle$ diffract, gets deeper as the number of $|a\rangle$ atoms grows. The relative number of diffracted $|a\rangle$ atoms has a pronounced minimum near $f_a = 0.5$, which can be interpreted as a "back-action" of the $|b\rangle$ atoms onto the $|a\rangle$ grating.

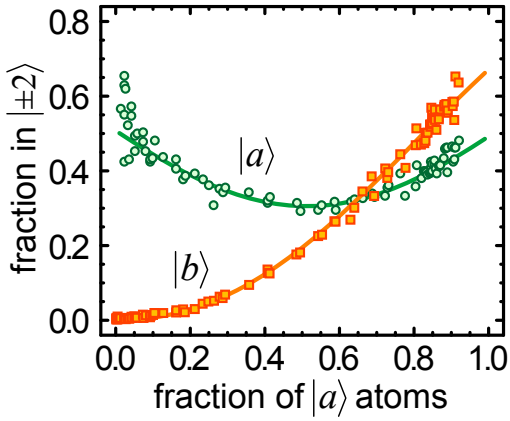

Figure 6.3: Fraction of atoms with momenta $\pm 2\hbar k_L$ in state $|a\rangle$ (green circles) and $|b\rangle$ (orange squares) after four-wave mixing. The solid curves are obtained from the theoretical model described in the text using the same parameters as in Fig. 6.4.

6.4 Theoretical Model

To obtain a more quantitative understanding, we theoretically model our system starting from the coupled Gross-Pitaevskii equations (GPE) for the order parameters $\Phi_\alpha(\mathbf{r}, t)$ of the two components $\alpha \in \{a, b\}$

$$i\hbar\,\partial_t \Phi_\alpha = \left(-\frac{\hbar^2}{2m}\nabla^2 + V_\alpha^{\mathrm{tot}} + \sum_{\beta\in\{a,b\}} g_{\alpha\beta}\,|\Phi_\beta|^2 \right) \Phi_\alpha, \tag{6.1}$$

where $g_{\alpha\beta} = 4\pi\hbar^2 a_{\alpha\beta}/m$, m is the atomic mass, and the intra and inter-species s-wave scattering lengths a_{aa}, a_{bb}, and a_{ab} in units of a_0 are 100.4, 99.0, and 99.0, respectively [114, 124]. The trapping and lattice potentials are given by $V_\alpha^{\mathrm{tot}} = V_{\mathrm{trap}}(\mathbf{r}, t) + V_\alpha(t)\,\sin^2(k_L z)$. Similar to the slowly-varying envelope approximation (SVEA) used in Refs. [32, 33, 45], we approximate the solution of Eq. (6.1) as an expansion in terms of momentum modes, or wave packets, moving along z with multiples of the recoil velocity $v_R = \hbar k_L/m$

$$\Phi_\alpha(\mathbf{r}, t) = \sum_{n=-\infty}^{\infty} c_{n\alpha}(t)\, e^{i\,n k_L z}\, \Phi_0(\mathbf{r} - \hat{\mathbf{z}}\, n v_R t, t)\,. \tag{6.2}$$

However, since we are mainly interested in the mode populations, we further assume that the wave packets Φ_0 are of Thomas–Fermi form and expand hydrodynamically after release from the trap [9], which leads to a significant

simplification compared to a full SVEA simulation. On the time scales of interest, phase-separation [125–127] can be neglected, and we have $\Phi_\alpha \propto \Phi_0$ for both components immediately following the microwave transfer [125, 126]. Since the momentum-spread of Φ_0 is much less than $\hbar k_L$, the modes in the expansion are quasi-orthogonal. After inserting the ansatz (6.2) into Eq. (6.1), we arrive at a system of coupled equations for the amplitudes $a_n(t) \equiv c_{na}(t)$

$$\begin{aligned} i\hbar\,\partial_t a_n = E_R\, n^2 a_n + V_a(t)\left[\tfrac{1}{2}\,a_n - \tfrac{1}{4}\,(a_{n+2} + a_{n-2})\right] \\ + \sum_{mm'n'} (g_{aa}\, a_m^* a_{m'} + g_{ab}\, b_m^* b_{m'}) a_{n'}\, h_{nmm'n'}(t) \end{aligned}$$

and similarly for the other component $b_n(t) \equiv c_{nb}(t)$. Here, $h_{nmm'n'}(t) \propto \delta(n+m-m'-n')$ denotes overlap integrals that include the effective temporal decay of the nonlinear interaction, as the different wave packets separate, and as the density decreases during the expansion. The terms responsible for FWM are of the form $b_m^* b_n a_m$ (and $a_m^* a_n b_m$ for the $|b\rangle$ component) with $m \neq n$. After adjacent modes ($|m-n| = 2$), for which the overlap decays the slowest, have completely separated, the populations remain frozen, since only equal-momentum self and cross-phase modulation terms of the forms $|a_n|^2 a_n$ and $|b_n|^2 a_n$ survive. With a typical Thomas–Fermi radius $R_z \sim 10$ μm, we obtain a typical separation time $t_{\mathrm{sep}} \approx 2R_z/2v_R$ of 1.7 ms.

6.5 Discussion

The full set of observed populations $|a_n|^2$ and $|b_n|^2$ after FWM is plotted in Fig. 6.4, along with predictions of our model obtained with parameters according to the experimental ones, leaving only the total atom number N as a fit parameter. The overall agreement between data and theory is remarkable. The maximum FWM yield occurs near $f_a = 2/3$ where the initial populations of the pump and seed modes are equal, maximizing the FWM term $a_m^* a_n b_m$ at $t = 0$ [32, 33]. The data also clearly show the correlated growth of $|b_{\pm 2}|^2$ and $|a_0|^2$, along with a corresponding depletion of the pump modes $|b_0|^2$ and $|a_{\pm 2}|^2$, as detailed in the inset.

We note that since the FWM yield is proportional to the inter-species scattering length as well as to the overlap $\int d^3r\, |\Phi_a|^2 |\Phi_b|^2$ of the two components, it can serve as a sensitive probe for both quantities. As a practical example, we use two-component FWM as a clear "single-shot" diagnostic for the optimization of component overlap. By carefully canceling magnetic field gradients we are able to sustain overlap, i.e. FWM yield, for up to 2 s after the microwave transfer.

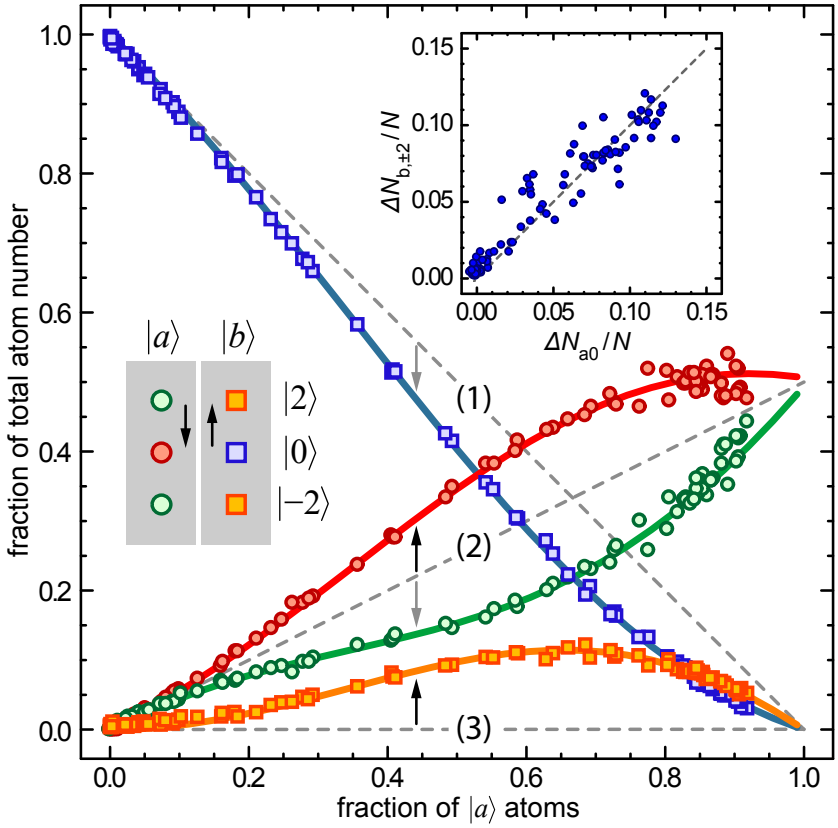

Figure 6.4: Mode populations after four-wave mixing. Populations $|c_{n\alpha}|^2 = N_{n\alpha}/N$ of the modes $|\alpha, n\rangle$, as indicated in the plaquette. The dashed lines (1), (2), and (3) indicate the initial conditions before FWM, $|b_0(0)|^2$, $|a_0(0)|^2 = |a_{\pm2}(0)|^2$, and $|b_{\pm2}(0)|^2$ (where ±2 indicates the combined populations). The arrows indicate the temporal evolution of the populations. The solid lines represent the predictions of the model ($V_a = 5.6\ E_R$, $\tau_{KD} = 25\ \mu$s, $\omega_z = 2\pi \times 51$ Hz, $N = 1.4 \times 10^5$). The inset shows the transferred $|b\rangle$ population vs. the transferred $|a\rangle$ population, where the dashed line represents a slope of unity.

To further confirm the coherence of the observed two-component FWM as implied by our model, we directly map out the time evolution of the output mode population $|b_{\pm2}|^2$ by interrupting the FWM process after a variable time through a selective removal of $|a\rangle$ atoms. This is achieved by a 50 μs long "blast" pulse of light resonant with the $F = 1 \rightarrow F' = 2$ repumping transition. As shown in Fig. 6.5, the atom number in the $|b, \pm2\rangle$ modes smoothly grows from zero to a maximum value reached around the expected separation time. The nonlinear, initially quadratic growth is indicative of a coherent process [33,

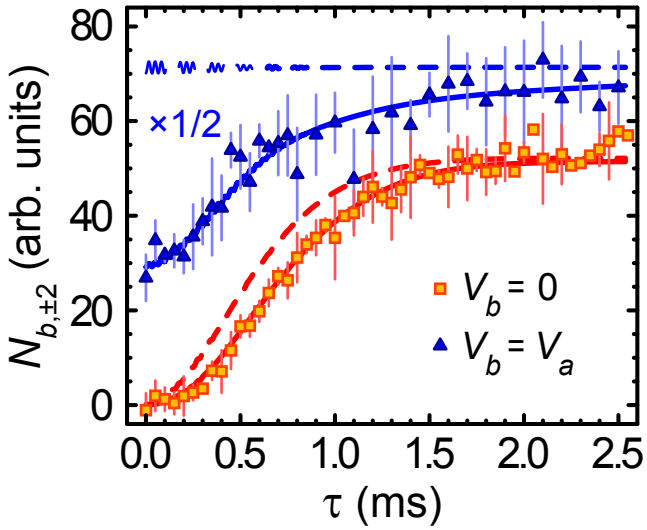

Figure 6.5: Growth of the population in the output mode $|b, \pm 2\rangle$ following the Kapitza–Dirac pulse for $V_b = 0$ (orange squares) and for $V_b = V_a$ (blue triangles, $\times 1/2$). The FWM was interrupted after a variable time τ by blasting away the $|a\rangle$ atoms. Each data point is averaged over 2–6 runs (here $\omega_z = 2\pi \times 41$ Hz, $f_a = 0.5$). The dashed lines are the predictions of the uncorrected model (including higher order FWM terms), whereas the solid lines take into account the loss of atoms during the blasting process (see text). The blast-loss model was calibrated by fitting to the $V_b = V_a$ data.

35] (other signs would be an overshoot and oscillations, which however would require higher densities or longer overlap). To exclude the possibility that the observed growth of the output mode population is merely an artifact caused by density-dependent losses of $|b\rangle$ atoms accompanying the blast (due to collisions with $|a\rangle$ atoms), we repeat the experiment with the polarization of the lattice beam chosen such that both components experience the same lattice depth of about 6 E_R. In this case, we expect the $|b, \pm 2\rangle$ modes to be populated immediately after the KD pulse, as indeed can be seen in Fig. 6.5. Further, no FWM is expected to occur for $V_b = V_a$, as the internal and external state dynamics are decoupled. By comparing the observed time evolution for this reference case with the expected one, we can calibrate our model for the blast-induced losses, which assumes a relative loss of $|b\rangle$ atoms proportional to the density of $|a\rangle$ atoms in the overlap region. With this correction, the theoretical

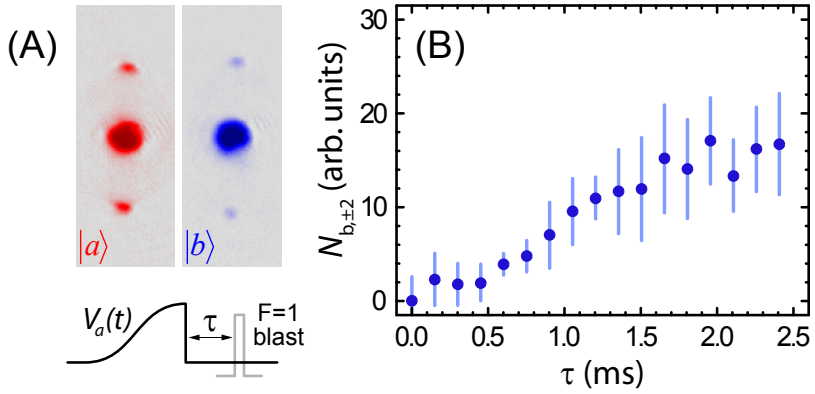

Figure 6.6: Four-wave mixing effects for an adiabatically ramped-up optical lattice. **(A)** An $|a\rangle$-selective lattice is ramped up to a depth of 6.0 E_R within 100 ms onto an equal mixture ($f_a = 0.5$). After release and 17 ms time of flight, $|b\rangle$ atoms appear in $|\pm 2\rangle$. **(B)** Growth of population in $|b, \pm 2\rangle$ as determined by blasting away the $|a\rangle$ atoms after an evolution time τ. Each data point is averaged over 6 runs.

time evolution for $V_b = 0$ matches the experimental data very well.

6.6 FWM after release from a slowly-loaded lattice

So far, we have discussed controlled FWM after application of a short optical pulse to induce diffraction. Now, we turn to the question whether FWM is also relevant in the case of adiabatically ramped-up, state-selective optical lattices. For such a system, inter-species interactions can be expected to give rise to diffraction effects qualitatively similar to those due to FWM. The density profile of the $|a\rangle$ component gets spatially modulated by the optical lattice, thus forming an "atomic lattice" that, in turn, should modulate the density of the $|b\rangle$ component. The momentum distribution after release should then exhibit diffraction peaks at $\pm 2\hbar k_L$, which thus could be interpreted as a signature of such a density modulation. However, we find that, at least as long as both components are in the superfluid state, FWM is by far the dominant mechanism for the emergence of recoiling $|b\rangle$ atoms, caused by the projection of the $|a\rangle$ component into plane-wave momentum modes after release. We note that the mismatch between the dispersion relations for $|a\rangle$ and $|b\rangle$ atoms suppresses FWM while the lattice is on. For $f_a = 0.5$ and $V_a = 6\ E_R$ ($V_b = 0$), as shown in Fig. 6.6 (A), we measure a relative population of up to 1.5 % in each of

the $|b, \pm 2\rangle$ states. Assuming this to be caused by a density modulation would require an atomic lattice modulation depth of 2 E_R, more than the chemical potential of the condensate in the lattice. A blast measurement as discussed above shows that the population in the observed peaks slowly grows only after release from the lattice (Fig. 6.6 (B)), indicating that the peaks are indeed caused by FWM.

We have performed analogous experiments for different final lattice depths V_a, and with additional, state-independent lattices along the x and y directions. In brief, we observe similar FWM effects along the state-dependent axis (cf. also [77], Fig. 8); however, we find that no FWM peaks are produced when the $|a\rangle$ atoms are in the Mott regime. This is consistent with the notion that FWM as described relies on the existence of a well-defined macroscopic phase and thus bears the potential to be used as a sensitive probe of phase coherence.

6.7 Conclusion

To summarize, we have demonstrated collinear four-wave mixing in a two-component mixture of bosonic atoms, and find excellent agreement with a simple theoretical model. Our work is of relevance both in the context of quantum atom optics [47], and for experimental studies of bosonic mixtures in optical lattices.

Chapter 7

Conclusion

In this thesis, I have described a versatile and simple moving-coil transporter apparatus for the production and study of magnetically and optically-trapped Bose-Einstein condensates. Further, I have reported on our first experiments using hyperfine-state mixtures of ultracold atoms in a state-selective optical lattice potential, which span from the strongly correlated regime to the field of nonlinear atom optics.

Using our BEC apparatus, in which the movable quadrupole coils are also used as an essential part of the final magnetic TOP trap, we have obtained the first BEC in downstate New York. In experiments with optically-trapped Bose-Einstein condensates, the quadrupole coils can be retracted before quantum degeneracy is reached, providing large optical access. Our apparatus has proven to be well-suited for experiments with optical lattices, as we have demonstrated by observing the superfluid-to-Mott insulator transition [90].

Further, we have observed many-body interaction effects in a homonuclear bosonic mixture in a three-dimensional optical lattice with variable state dependence along one axis [107]. Near the superfluid-to-Mott insulator transition for one component, we have found that the presence of a second component can reduce the apparent superfluid coherence, most significantly when the second component either experiences a strongly localizing lattice potential or almost none at all. We have examined this effect by varying the relative populations and lattice depths, and have discussed the observed behavior in view of recent proposals for atomic disorder and polaron-induced localization.

We have demonstrated atomic four-wave mixing of two-component matter waves in a collinear geometry with macroscopic mode populations [115]. Starting from a single-species Bose–Einstein condensate, we have prepared seed and pump modes through microwave state transfer and state-selective Kapitza–Dirac diffraction. We have observed how four-wave mixing subsequently populates the initially empty output modes, in very good agreement

with simulations based on a coupled-mode expansion of the Gross–Pitaevskii equation. We have shown that four-wave mixing can play a role in studies of homonuclear bosonic mixtures in optical lattices. Moreover, our system of internal and momentum modes coupled via four-wave mixing might have future applications in sub-shot noise atom interferometry [47].

In conclusion, the experimental system that we have realized over the course of the last few years has allowed us to perform a wide range of experiments involving two-component bosonic mixtures in state-dependent lattice potentials. Beyond the experiments I have described in this thesis, we have been able to demonstrate Bragg diffraction of a matter wave from a dilute atomic crystal [128], which can be used as a sensitive probe of the structure and long-range order of the atomic crystal. Further, we have by now more extensively explored the case of a strongly localized background component [129], which acts as a fine-grained atomic disorder potential, and have studied how this type of disorder affects the transport and localization behavior of the foreground atoms, in comparison to the pseudo-random potential created by an incommensurate bichromatic optical lattice.

Apart from the experimental investigation of the phases of the two-component Bose-Hubbard model such as the counterflow superfluid [15], natural future areas of study may include disordered systems [25, 26], polaron systems [23] and phonon-mediated interactions [130], as well as decoherence mechanisms and quantum dissipative systems [20, 21].

Bibliography

[1] Bose, "Plancks Gesetz und Lichtquantenhypothese," Z. Phys. **26**, 178 (1924).

[2] A. Einstein, "Quantentheorie des einatomigen idealen Gases," Sitzber. preuss. Akad. Wiss., Physik.-math. Kl. p. 261 (1924).

[3] A. Einstein, "Quantentheorie des einatomigen idealen Gases. Zweite Abhandlung," Sitzber. preuss. Akad. Wiss., Physik.-math. Kl. p. 3 (1925).

[4] M. Anderson, J. Ensher, M. Matthews, C. Wieman, and E. Cornell, "Observation of Bose-Einstein Condensation in a Dilute Atomic Vapor," Science **269**, 198 (1995).

[5] K. B. Davis, M. Mewes, M. R. Andrews, N. J. van Druten, D. S. Durfee, D. M. Kurn, and W. Ketterle, "Bose-Einstein Condensation in a Gas of Sodium Atoms," Phys. Rev. Lett. **75**, 3969 (1995).

[6] C. Bradley, C. Sackett, J. Tollett, and R. Hulet, "Evidence of Bose-Einstein Condensation in an Atomic Gas with Attractive Interactions," Phys. Rev. Lett. **75**, 1687 (1995).

[7] C. C. Bradley, C. A. Sackett, and R. G. Hulet, "Bose-Einstein Condensation of Lithium: Observation of Limited Condensate Number," Phys. Rev. Lett. **78**, 985 (1997).

[8] W. Ketterle, D. S. Durfee, and D. M. Stamper-Kurn, *M. Inguscio and S. Stringari and C.E. Wieman (eds.),* Bose-Einstein Condensation in Atomic Gases*, Proceedings of the International School of Physics "Enrico Fermi" Course CXL* (IOS Press Amsterdam, 1999). Also available online at arXiv:cond-mat/9904034v2.

[9] F. Dalfovo, S. Giorgini, L. P. Pitaevskii, and S. Stringari, "Theory of Bose-Einstein condensation in trapped gases," Rev. Mod. Phys. **71**, 463 (1999).

[10] I. Bloch, J. Dalibard, and W. Zwerger, "Many-body physics with ultracold gases," Rev. Mod. Phys. **80**, 885 (2008).

[11] O. Morsch and M. K. Oberthaler, "Dynamics of Bose-Einstein condensates in optical lattices," Rev. Mod. Phys. **78**, 179 (2006).

[12] C. Chin, R. Grimm, P. Julienne, and E. Tiesinga, "Feshbach resonances in ultracold gases," Rev. Mod. Phys. **82**, 1225 (2010).

[13] M. Greiner, O. Mandel, T. Esslinger, T. W. Hänsch, and I. Bloch, "Quantum phase transition from a superfluid to a Mott insulator in a gas of ultracold atoms," Nature **415**, 39 (2002).

[14] D. Jaksch, C. Bruder, J. I. Cirac, C. W. Gardiner, and P. Zoller, "Cold Bosonic Atoms in Optical Lattices," Phys. Rev. Lett. **81**, 3108 (1998).

[15] A. B. Kuklov and B. V. Svistunov, "Counterflow Superfluidity of Two-Species Ultracold Atoms in a Commensurate Optical Lattice," Phys. Rev. Lett. **90**, 100401 (2003).

[16] E. Altman, W. Hofstetter, E. Demler, and M. D. Lukin, "Phase diagram of two-component bosons on an optical lattice," New J. Phys. **5**, 113 (2003).

[17] A. Isacsson, M.-C. Cha, K. Sengupta, and S. M. Girvin, "Superfluid-insulator transitions of two-species bosons in an optical lattice," Phys. Rev. B **72**, 184507 (2005).

[18] S. G. Şöyler, B. Capogrosso-Sansone, N. V. Prokof'ev, and B. V. Svistunov, "Sign-alternating interaction mediated by strongly correlated lattice bosons," New J. Phys. **11**, 073036 (2009).

[19] L.-M. Duan, E. Demler, and M. D. Lukin, "Controlling Spin Exchange Interactions of Ultracold Atoms in Optical Lattices," Phys. Rev. Lett. **91**, 090402 (2003).

[20] P. P. Orth, I. Stanic, and K. Le Hur, "Dissipative quantum Ising model in a cold-atom spin-boson mixture," Phys. Rev. A **77**, 051601 (2008).

[21] A. J. Leggett, S. Chakravarty, A. T. Dorsey, M. P. A. Fisher, A. Garg, and W. Zwerger, "Dynamics of the dissipative two-state system," Rev. Mod. Phys. **59**, 1 (1987).

[22] K. Sacha and E. Timmermans, "Self-localized impurities embedded in a one-dimensional Bose-Einstein condensate and their quantum fluctuations," Phys. Rev. A **73**, 063604 (2006).

[23] M. Bruderer, A. Klein, S. R. Clark, and D. Jaksch, "Polaron physics in optical lattices," Phys. Rev. A **76**, 011605 (2007).

[24] A. Schirotzek, C.-H. Wu, A. Sommer, and M. W. Zwierlein, "Observation of Fermi Polarons in a Tunable Fermi Liquid of Ultracold Atoms," Phys. Rev. Lett. **102**, 230402 (2009).

[25] U. Gavish and Y. Castin, "Matter-Wave Localization in Disordered Cold Atom Lattices," Phys. Rev. Lett. **95**, 020401 (2005).

[26] B. Paredes, F. Verstraete, and J. I. Cirac, "Exploiting Quantum Parallelism to Simulate Quantum Random Many-Body Systems," Phys. Rev. Lett. **95**, 140501 (2005).

[27] T. Roscilde and J. I. Cirac, "Quantum Emulsion: A Glassy Phase of Bosonic Mixtures in Optical Lattices," Phys. Rev. Lett. **98**, 190402 (2007).

[28] K. Sheshadri, H. R. Krishnamurthy, R. Pandit, and T. V. Ramakrishnan, "Percolation-Enhanced Localization in the Disordered Bosonic Hubbard Model," Phys. Rev. Lett. **75**, 4075 (1995).

[29] P. Buonsante, F. Massel, V. Penna, and A. Vezzani, "Gutzwiller approach to the Bose-Hubbard model with random local impurities," Phys. Rev. A **79**, 013623 (2009).

[30] R. W. Boyd, *Nonlinear Optics* (Academic Press, San Diego, 2003).

[31] L. Deng, E. W. Hagley, J. Wen, M. Trippenbach, Y. Band, P. S. Julienne, J. E. Simsarian, K. Helmerson, S. L. Rolston, and W. D. Phillips, "Four-wave mixing with matter waves," Nature **398**, 218 (1999).

[32] M. Trippenbach, Y. B. Band, and P. S. Julienne, "Four-wave mixing in the scattering of Bose-Einstein condensates," Opt. Express **3**, 530 (1998).

[33] M. Trippenbach, Y. B. Band, and P. S. Julienne, "Theory of four-wave mixing of matter waves from a Bose-Einstein condensate," Phys. Rev. A **62**, 023608 (2000).

[34] P. Meystre, *Atom Optics* (Springer, New York, 2001).

[35] J. M. Vogels, K. Xu, and W. Ketterle, "Generation of Macroscopic Pair-Correlated Atomic Beams by Four-Wave Mixing in Bose-Einstein Condensates," Phys. Rev. Lett. **89**, 020401 (2002).

[36] J. M. Vogels, J. K. Chin, and W. Ketterle, "Coherent Collisions between Bose-Einstein Condensates," Phys. Rev. Lett. **90**, 030403 (2003).

[37] A. Perrin, H. Chang, V. Krachmalnicoff, M. Schellekens, D. Boiron, A. Aspect, and C. I. Westbrook, "Observation of Atom Pairs in Spontaneous Four-Wave Mixing of Two Colliding Bose-Einstein Condensates," Phys. Rev. Lett. **99**, 150405 (2007).

[38] R. G. Dall, L. J. Byron, A. G. Truscott, G. R. Dennis, M. T. Johnsson, and J. J. Hope, "Paired-atom laser beams created via four-wave mixing," Phys. Rev. A **79**, 011601 (2009).

[39] K. M. Hilligsøe and K. Mølmer, "Phase-matched four wave mixing and quantum beam splitting of matter waves in a periodic potential," Phys. Rev. A **71**, 041602 (2005).

[40] N. Gemelke, E. Sarajlic, Y. Bidel, S. Hong, and S. Chu, "Parametric Amplification of Matter Waves in Periodically Translated Optical Lattices," Phys. Rev. Lett. **95**, 170404 (2005).

[41] G. K. Campbell, J. Mun, M. Boyd, E. W. Streed, W. Ketterle, and D. E. Pritchard, "Parametric Amplification of Scattered Atom Pairs," Phys. Rev. Lett. **96**, 020406 (2006).

[42] E. V. Goldstein and P. Meystre, "Phase conjugation of multicomponent Bose-Einstein condensates," Phys. Rev. A **59**, 1509 (1999).

[43] H. Pu and P. Meystre, "Creating Macroscopic Atomic Einstein-Podolsky-Rosen States from Bose-Einstein Condensates," Phys. Rev. Lett. **85**, 3987 (2000).

[44] L.-M. Duan, A. Sørensen, J. I. Cirac, and P. Zoller, "Squeezing and Entanglement of Atomic Beams," Phys. Rev. Lett. **85**, 3991 (2000).

[45] J. P. Burke, P. S. Julienne, C. J. Williams, Y. B. Band, and M. Trippenbach, "Four-wave mixing in Bose-Einstein condensate systems with multiple spin states," Phys. Rev. A **70**, 033606 (2004).

[46] C. Klempt, O. Topic, G. Gebreyesus, M. Scherer, T. Henninger, P. Hyllus, W. Ertmer, L. Santos, and J. J. Arlt, "Multiresonant Spinor Dynamics in a Bose-Einstein Condensate," Phys. Rev. Lett. **103**, 195302 (2009).

[47] S. A. Haine and A. J. Ferris, "Surpassing the standard quantum limit in an atom interferometer with four-mode entanglement produced from four-wave mixing," Phys. Rev. A **84**, 043624 (2011).

[48] F. London, "The λ-Phenomenon of Liquid Helium and the Bose-Einstein Degeneracy," Nature **141**, 643 (1938).

[49] F. London, "On the Bose-Einstein Condensation," Phys. Rev. **54**, 947 (1938).

[50] H. J. Metcalf and P. van der Straten, *Laser Cooling and Trapping* (Springer, New York, 1999).

[51] H. F. Hess, "Evaporative cooling of magnetically trapped and compressed spin-polarized hydrogen," Phys. Rev. B **34**, 3476 (1986).

[52] E. A. Cornell and C. E. Wieman, "Nobel Lecture: Bose-Einstein condensation in a dilute gas, the first 70 years and some recent experiments," Rev. Mod. Phys. **74**, 875 (2002).

[53] W. Ketterle, "Nobel Lecture: When atoms behave as waves: Bose-Einstein condensation and the atom laser," Rev. Mod. Phys. **74**, 1131 (2002).

[54] K. Huang, *Statistical Mechanics*, 2nd ed. (John Wiley and Sons, New York, 1987).

[55] M. Plischke and B. Bergersen, *Equilibrium Statistical Physics*, 3rd ed. (World Scientific, Singapore, 2006).

[56] A. L. Fetter and J. D. Walecka, *Quantum Theory of Many-Particle Systems*, Dover reprint ed. (Dover Publications, Mineola, 2003).

[57] L. Pitaevskii and S. Stringari, *Bose-Einstein Condensation* (Clarendon Press, Oxford, 2003).

[58] C. Pethick and H. Smith, *Bose-Einstein Condensation in Dilute Gases*, 2nd ed. (Cambridge University Press, New York, 2008).

[59] A. J. Leggett, "Bose-Einstein condensation in the alkali gases: Some fundamental concepts," Rev. Mod. Phys. **73**, 307 (2001).

[60] W. Pauli, "The Connection Between Spin and Statistics," Phys. Rev. **58**, 716 (1940).

[61] A. Stern, "Anyons and the quantum Hall effect - A pedagogical review," Ann. Phys. **323**, 204 (2008).

[62] O. Penrose and L. Onsager, "Bose-Einstein Condensation and Liquid Helium," Phys. Rev. **104**, 576 (1956).

[63] C. N. Yang, "Concept of Off-Diagonal Long-Range Order and the Quantum Phases of Liquid He and of Superconductors," Rev. Mod. Phys. **34**, 694 (1962).

[64] Y. Castin and R. Dum, "Bose-Einstein Condensates in Time Dependent Traps," Phys. Rev. Lett. **77**, 5315 (1996).

[65] Y. Kagan, E. L. Surkov, and G. V. Shlyapnikov, "Evolution of a Bose-condensed gas under variations of the confining potential," Phys. Rev. A **54**, 1753 (1996).

[66] R. P. Feynman, F. L. Vernon, Jr., and R. W. Hellwarth, "Geometrical Representation of the Schrödinger Equation for Solving Maser Problems," J. Appl. Phys. **28**, 49 (1957).

[67] R. Loudon, *The Quantum Theory of Light*, 3rd ed. (Oxford University Press, New York, 2000).

[68] G. Breit and I. I. Rabi, "Measurement of Nuclear Spin," Phys. Rev. **38**, 2082 (1931).

[69] I. H. Deutsch and P. S. Jessen, "Quantum-state control in optical lattices," Phys. Rev. A **57**, 1972 (1998).

[70] D. Jaksch, H.-J. Briegel, J. I. Cirac, C. W. Gardiner, and P. Zoller, "Entanglement of Atoms via Cold Controlled Collisions," Phys. Rev. Lett. **82**, 1975 (1999).

[71] D. Jaksch and P. Zoller, "The cold atom Hubbard toolbox," Ann. Phys. (NY) **315**, 52 (2005).

[72] R. Grimm, M. Weidemüller, and Y. B. Ovchinnikov, "Optical dipole traps for neutral atoms," Adv. At. Mol. Opt. Phys. **42**, 95 (2000). Also available online at arXiv:physics/9902072v1.

[73] C. Cohen-Tannoudji, J. Dupont-Roc, and G. Grynberg, *Atom-Photon Interactions: Basic Processes and Applications* (John Wiley & Sons, New York, 1992).

[74] J. Dalibard and C. Cohen-Tannoudji, "Dressed-atom approach to atomic motion in laser light: the dipole force revisited," J. Opt. Soc. Am. B **2**, 1707 (1985).

[75] J. P. Gordon and A. Ashkin, "Motion of atoms in a radiation trap," Phys. Rev. A **21**, 1606 (1980).

[76] F. Gerbier and Y. Castin, "Heating rates for an atom in a far-detuned optical lattice," Phys. Rev. A **82**, 013615 (2010).

[77] D. McKay and B. DeMarco, "Thermometry with spin-dependent lattices," New J. Phys. **12**, 055013 (2010).

[78] R. H. Reimann, "Quantum Gases in State-Dependent Optical Potentials," M.A. thesis, Stony Brook University (2009).

[79] P. L. Gould, G. A. Ruff, and D. E. Pritchard, "Diffraction of atoms by light: The near-resonant Kapitza-Dirac effect," Phys. Rev. Lett. **56**, 827 (1986).

[80] Y. B. Ovchinnikov, J. H. Müller, M. R. Doery, E. J. D. Vredenbregt, K. Helmerson, S. L. Rolston, and W. D. Phillips, "Diffraction of a Released Bose-Einstein Condensate by a Pulsed Standing Light Wave," Phys. Rev. Lett. **83**, 284 (1999).

[81] B. Gadway, D. Pertot, R. Reimann, M. G. Cohen, and D. Schneble, "Analysis of Kapitza-Dirac diffraction patterns beyond the Raman-Nath regime," Opt. Express **17**, 19173 (2009).

[82] M. Abramowitz and I. A. Stegun, eds., *Handbook of Mathematical Functions with Formulas, Graphs, and Mathematical Tables* (National Bureau of Standards, Applied Mathematics Series - 55, 1964).

[83] NIST, *NIST Digital Library of Mathematical Functions* (National Institute of Standards and Technology, 2010-05-07). Available online at http://dlmf.nist.gov/.

[84] M. P. A. Fisher, P. B. Weichman, G. Grinstein, and D. S. Fisher, "Boson localization and the superfluid-insulator transition," Phys. Rev. B **40**, 546 (1989).

[85] B. Capogrosso-Sansone, N. Prokof'ev, and B. Svistunov, "Phase diagram and thermodynamics of the three-dimensional Bose-Hubbard model," Phys. Rev. B **75**, 134302 (2007).

[86] D. van Oosten, P. van der Straten, and H. T. C. Stoof, "Quantum phases in an optical lattice," Phys. Rev. A **63**, 053601 (2001).

[87] A. Hubener, M. Snoek, and W. Hofstetter, "Magnetic phases of two-component ultracold bosons in an optical lattice," Phys. Rev. B **80**, 245109 (2009).

[88] H. Lewandowski, D. Harber, D. Whittaker, and E. Cornell, "Simplified System for Creating a Bose-Einstein Condensate," J. Low Temp. Phys. **132**, 309 (2003).

[89] W. Petrich, M. Anderson, J. Ensher, and E. Cornell, "Stable, Tightly Confining Magnetic Trap for Evaporative Cooling of Neutral Atoms," Phys. Rev. Lett. **74**, 3352 (1995).

[90] D. Pertot, D. Greif, S. Albert, B. Gadway, and D. Schneble, "Versatile transporter apparatus for experiments with optically trapped Bose-Einstein condensates," J. Phys. B: At. Mol. Opt. Phys. **42**, 215305 (2009).

[91] D. E. Sproles, "Laser Spectroscopy and Magneto-Optical Trapping of Rubidium Atoms," M.S.I. thesis, Stony Brook University (2008).

[92] B. P. Anderson and M. A. Kasevich, "Loading a vapor-cell magneto-optic trap using light-induced atom desorption," Phys. Rev. A **63**, 023404 (2001).

[93] C. Klempt, T. van Zoest, T. Henninger, O. Topic, E. Rasel, W. Ertmer, and J. Arlt, "Ultraviolet light-induced atom desorption for large rubidium and potassium magneto-optical traps," Phys. Rev. A **73**, 013410 (2006).

[94] K. Nakagawa, Y. Suzuki, M. Horikoshi, and J. Kim, "Simple and efficient magnetic transport of cold atoms using moving coils for the production of Bose-Einstein condensation," Appl. Phys. B **81**, 791 (2005).

[95] S. G. Albert, "Cooling, Trapping, and Transport of Atom Clouds in a New BEC Apparatus," M.A. thesis, Stony Brook University (2007).

[96] D. G. Greif, "Evaporative cooling and Bose-Einstein Condensation of Rb-87 in a moving-coil TOP trap geometry," M.A. thesis, Stony Brook University (2007).

[97] J. H. Müller, O. Morsch, D. Ciampini, M. Anderlini, R. Mannella, and E. Arimondo, "Atomic Micromotion and Geometric Forces in a Triaxial Magnetic Trap," Phys. Rev. Lett. **85**, 4454 (2000).

[98] M. Cristiani, O. Morsch, J. H. Müller, D. Ciampini, and E. Arimondo, "Experimental properties of Bose-Einstein condensates in one-dimensional optical lattices: Bloch oscillations, Landau-Zener tunneling, and mean-field effects," Phys. Rev. A **65**, 63612 (2002).

[99] Y. Yoshikawa, T. Umeki, T. Mukae, Y. Torii, and T. Kuga, "Frequency stabilization of a laser diode with use of light-induced birefringence in an atomic vapor," Applied Optics **42**, 6645 (2003).

[100] C. P. Pearman, C. S. Adams, S. G. Cox, P. F. Griffin, D. A. Smith, and I. G. Hughes, "Polarization spectroscopy of a closed atomic transition: applications to laser frequency locking," J. Phys. B: At. Mol. Opt. Phys. **35**, 5141 (2002).

[101] C. E. Wieman and T. W. Hänsch, "Doppler-Free Laser Polarization Spectroscopy," Phys. Rev. Lett. **36**, 1170 (1976).

[102] T. Esslinger, I. Bloch, and T. W. Hänsch, "Bose-Einstein condensation in a quadrupole-Ioffe-configuration trap," Phys. Rev. A **58**, R2664 (1998).

[103] J. M. Reeves, O. Garcia, B. Deissler, K. L. Baranowski, K. J. Hughes, and C. A. Sackett, "Time-orbiting potential trap for Bose-Einstein condensate interferometry," Phys. Rev. A **72**, 051605 (2005).

[104] K. L. Baranowski and C. A. Sackett, "A stable ac current source for magnetic traps," J. Phys. B: At. Mol. Opt. Phys. **39**, 2949 (2006).

[105] W. Ketterle and N. J. van Druten, "Evaporative cooling of trapped atoms," Adv. At. Mol. Opt. Phys. **37**, 181 (1996).

[106] N. Gemelke, X. Zhang, C.-L. Hung, and C. Chin, "In-situ observation of incompressible Mott-insulating domains of ultracold atomic gases," Nature **460**, 995 (2009).

[107] B. Gadway, D. Pertot, R. Reimann, and D. Schneble, "Superfluidity of Interacting Bosonic Mixtures in Optical Lattices," Phys. Rev. Lett. **105**, 045303 (2010).

[108] J. Catani, L. D. Sarlo, G. Barontini, F. Minardi, and M. Inguscio, "Degenerate Bose-Bose mixture in a three-dimensional optical lattice," Phys. Rev. A **77**, 011603 (2008).

[109] K. Günter, T. Stöferle, H. Moritz, M. Köhl, and T. Esslinger, "Bose-Fermi Mixtures in a Three-Dimensional Optical Lattice," Phys. Rev. Lett. **96**, 180402 (2006).

[110] S. Ospelkaus, C. Ospelkaus, O. Wille, M. Succo, P. Ernst, K. Sengstock, and K. Bongs, "Localization of Bosonic Atoms by Fermionic Impurities in a Three-Dimensional Optical Lattice," Phys. Rev. Lett. **96**, 180403 (2006).

[111] T. Best, S. Will, U. Schneider, L. Hackermüller, D. van Oosten, I. Bloch, and D.-S. Lühmann, "Role of Interactions in ^{87}Rb-^{40}K Bose-Fermi Mixtures in a 3D Optical Lattice," Phys. Rev. Lett. **102**, 030408 (2009).

[112] P. Buonsante, S. M. Giampaolo, F. Illuminati, V. Penna, and A. Vezzani, "Mixtures of Strongly Interacting Bosons in Optical Lattices," Phys. Rev. Lett. **100**, 240402 (2008).

[113] M.-O. Mewes, M. R. Andrews, D. M. Kurn, D. S. Durfee, C. G. Townsend, and W. Ketterle, "Output Coupler for Bose-Einstein Condensed Atoms," Phys. Rev. Lett. **78**, 582 (1997).

[114] S. J. J. M. F. Kokkelmans (private communication).

[115] D. Pertot, B. Gadway, and D. Schneble, "Collinear Four-Wave Mixing of Two-Component Matter Waves," Phys. Rev. Lett. **104**, 200402 (2010).

[116] F. Gerbier, A. Widera, S. Fölling, O. Mandel, T. Gericke, and I. Bloch, "Phase Coherence of an Atomic Mott Insulator," Phys. Rev. Lett. **95**, 050404 (2005).

[117] C. Kollath, U. Schollwöck, J. von Delft, and W. Zwerger, "Spatial correlations of trapped one-dimensional bosons in an optical lattice," Phys. Rev. A **69**, 031601 (2004).

[118] C. Orzel, A. K. Tuchman, M. L. Fenselau, M. Yasuda, and M. A. Kasevich, "Squeezed States in a Bose-Einstein Condensate," Science **291**, 2386 (2001).

[119] P. B. Blakie and J. V. Porto, "Adiabatic loading of bosons into optical lattices," Phys. Rev. A **69**, 013603 (2004).

[120] P. B. Blakie and W.-X. Wang, "Bose-Einstein condensation in an optical lattice," Phys. Rev. A **76**, 053620 (2007).

[121] D. M. Weld, P. Medley, H. Miyake, D. Hucul, D. E. Pritchard, and W. Ketterle, "Spin Gradient Thermometry for Ultracold Atoms in Optical Lattices," Phys. Rev. Lett. **103**, 245301 (2009).

[122] A. Recati, P. O. Fedichev, W. Zwerger, J. von Delft, and P. Zoller, "Atomic Quantum Dots Coupled to a Reservoir of a Superfluid Bose-Einstein Condensate," Phys. Rev. Lett. **94**, 040404 (2005).

[123] P. Pedri, L. Pitaevskii, S. Stringari, C. Fort, S. Burger, F. S. Cataliotti, P. Maddaloni, F. Minardi, and M. Inguscio, "Expansion of a Coherent Array of Bose-Einstein Condensates," Phys. Rev. Lett. **87**, 220401 (2001).

[124] B. J. Verhaar, E. G. M. van Kempen, and S. J. J. M. F. Kokkelmans, "Predicting scattering properties of ultracold atoms: Adiabatic accumulated phase method and mass scaling," Phys. Rev. A **79**, 032711 (2009).

[125] D. S. Hall, M. R. Matthews, J. R. Ensher, C. E. Wieman, and E. A. Cornell, "Dynamics of Component Separation in a Binary Mixture of Bose-Einstein Condensates," Phys. Rev. Lett. **81**, 1539 (1998).

[126] D. S. Hall, M. R. Matthews, C. E. Wieman, and E. A. Cornell, "Measurements of Relative Phase in Two-Component Bose-Einstein Condensates," Phys. Rev. Lett. **81**, 1543 (1998).

[127] K. M. Mertes, J. W. Merrill, R. Carretero-González, D. J. Frantzeskakis, P. G. Kevrekidis, and D. S. Hall, "Nonequilibrium Dynamics and Superfluid Ring Excitations in Binary Bose-Einstein Condensates," Phys. Rev. Lett. **99**, 190402 (2007).

[128] B. Gadway, D. Pertot, J. Reeves, and D. Schneble, "Probing an Ultracold-Atom Crystal with Matter Waves," arXiv:1104.2564v1 (2011).

[129] B. Gadway, D. Pertot, J. Reeves, M. Vogt, and D. Schneble, "Glassy Behavior in a Binary Atomic Mixture," Phys. Rev. Lett. **107**, 145306 (2011).

[130] A. Klein, M. Bruderer, S. R. Clark, and D. Jaksch, "Dynamics, dephasing and clustering of impurity atoms in Bose-Einstein condensates," New J. Phys. **9**, 411 (2007).

[131] P. S. Jessen and I. H. Deutsch, "Optical lattices," Adv. At. Mol. Opt. Phys. (37), 95 (1996).

[132] A. Messiah, *Quantum Mechanics (Two volumes bound as one)*, Dover reprint ed. (Dover Publications, Mineola, 1999).

[133] J. J. Sakurai, *Modern Quantum Mechanics*, revised ed. (Addison-Wesley, Reading, 1994).

[134] D. A. Steck, "Rubidium 87 D Line Data," available online at `http://steck.us/alkalidata`. (revision 2.1.2, 12 August 2009).

Appendix A

Dipole Matrix Elements for Multi-level Atoms

In this this appendix we explicitly calculate the dipole matrix elements for a multi-level atom interacting with a classical light-field.

A.1 Atom-light interaction

The atom-light interaction Hamiltonian assuming a classical light field $\mathbf{E}$ is

$$H_{\text{ali}} = -\hat{\mathbf{d}} \cdot \mathbf{E}(\mathbf{r}, t) \tag{A.1}$$

with the dipole operator $\hat{\mathbf{d}} = -e\,\hat{\mathbf{r}}$. In terms of the polarizability it is

$$H_{\text{ali}} = -\frac{1}{2}\mathbf{E}^{\dagger}\hat{\boldsymbol{\alpha}}\,\mathbf{E}. \tag{A.2}$$

Writing the interaction Hamiltonian in the basis of the atomic eigenstates $|i\rangle$ we obtain the matrix elements

$$\langle j|H_{\text{ali}}|i\rangle = e\,\langle j|\hat{\mathbf{r}} \cdot \mathbf{E}|i\rangle = e\int d^3r\ \psi_j^*(\mathbf{r})\psi_i(\mathbf{r})\,\mathbf{r} \cdot \mathbf{E}(\mathbf{r}, t), \tag{A.3}$$

where $\psi_i(\mathbf{r}) = \langle \mathbf{r}|i\rangle$. Since the spatial variation of the electric field is usually very small over the size of the atomic wave functions, the electric field can be regarded as uniform over the size of the atom, and can be pulled out of the integral. This leads to

$$\langle j|H_{\text{ali}}|i\rangle = e\,\langle j|\hat{\mathbf{r}}|i\rangle \cdot \mathbf{E} = e\left(\int d^3r\ \psi_j^*(\mathbf{r})\psi_i(\mathbf{r})\,\mathbf{r}\right) \cdot \mathbf{E} \equiv e\,\mathbf{d}_{ji} \cdot \mathbf{E}. \tag{A.4}$$

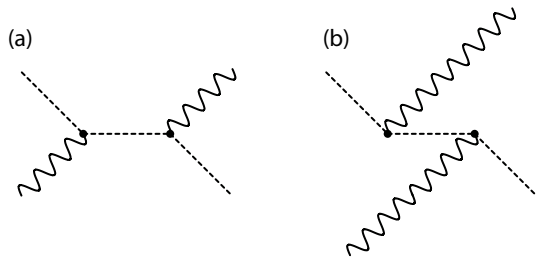

Figure A.1: The two possible second order perturbation theory diagrams to calculate the light shift. The dotted line represents the atom, the wavy lines represent quanta of the radiation field. Time is in the horizontal direction. **(a)** The atom absorbs light and gets into an intermediate higher internal state, then reemits the light, going back to the original state. **(b)** The opposite process is also possible, i.e. the atom emits light and goes into a lower internal state, and then reabsorbs a quantum from the radiation field. This process corresponds to the counter-rotating term that is usually neglected in the rotating wave approximation.

The here defined dipole matrix elements $\mathbf{d}_{ji}$ accordingly have the property

$$\mathbf{d}_{ji}^{*} = \mathbf{d}_{ij}, \tag{A.5}$$

which simply means that the dipole matrix (actually there are three) is Hermitian.

A.2 Optical Dipole Potential

The optical dipole potential corresponds to the spatially varying light shift of the atomic energy levels that they experience in an light field of varying intensity. The light shift for a multi-level atom can be calculated to very good approximation by treating the atom-light interaction $-\mathbf{d}\cdot\mathbf{E}$ as a perturbation. To leading order one obtains

$$\Delta E_i = \sum_{l\neq i} \frac{\left|\langle l|\mathbf{d}\cdot\mathbf{E}|i\rangle\right|^2}{E_i - E_l} = \sum_{l\neq i} \frac{\left|\mathbf{d}_{li}\cdot\mathbf{E}\right|^2}{E_i - E_l} = \sum_{l\neq i} \frac{\left(\mathbf{E}\cdot\mathbf{d}_{il}\right)\left(\mathbf{d}_{li}\cdot\mathbf{E}\right)}{E_i - E_l} \tag{A.6}$$

with $\mathbf{d}_{li} \equiv \langle l|\mathbf{d}|i\rangle = \mathbf{d}_{il}^{*}$. There is no first-order correction, since the dipole matrix element between same states vanishes due to parity.

It should be noted that the energy of the intermediate state E_l is not simply the eigenenergy of the atomic level, but it includes the state of the radiation

field, which has lost an energy quantum to the atom in the intermediate state, such that $E_l = \mathcal{E}_l - \hbar\omega$. Although much less probable, another possible process is that the atom first emits and then reabsorbs a photon. In this case, illustrated in Fig. A.1(b), the energy of the intermediate state is $E_l = \mathcal{E}_l + \hbar\omega$. This case corresponds to the counter-rotating term usually neglected in the rotating-wave approximation. So the denominator in (A.6) becomes

$$\frac{1}{E_i - E_l} = \frac{1}{E_i - \mathcal{E}_l + \hbar\omega} + \frac{1}{E_i - \mathcal{E}_l - \hbar\omega} = -\frac{1}{\hbar}\left[\frac{1}{\omega_l - \omega} + \frac{1}{\omega_l + \omega}\right] \tag{A.7}$$

where $\hbar\omega_l \equiv \mathcal{E}_l - \mathcal{E}_i$ is the energy difference between the fixed initial state and the intermediate state l. For a laser wavelength in between the D1 and D2 lines of rubidium, the contribution of the "counter-rotating" term is less than 1 % compared to the first term and may be neglected. For 1064 nm light, however, both terms should be retained, as the second term is already about 15 % of the first.

Here the electric field can be treated as a classical external field, since the light produced by a laser is essentially in a coherent quantum state. We can write the electric field at the position of the atom as

$$\mathbf{E} = \mathrm{Re}\,\mathbf{E}^{(+)}e^{-i\,\omega t} = \frac{1}{2}\left(\mathbf{E}^{(+)}e^{-i\,\omega t} + \mathbf{E}^{(-)}e^{i\,\omega t}\right) \tag{A.8}$$

where the complex vector $\mathbf{E}^{(+)}$ is the "positive" frequency component of the field, and $\mathbf{E}^{(-)} = \left(\mathbf{E}^{(+)}\right)^*$ [67, 75, 131]. In a quantum treatment $\mathbf{E}^{(+)}$ would be a destruction operator for the electric field at a certain position [67].

Plugging this into the numerator of (A.6) and performing a cycle average over the fast optical frequency yields

$$\langle(\mathbf{E}\cdot\mathbf{d}_{il})\,(\mathbf{d}_{li}\cdot\mathbf{E})\rangle_T = \frac{1}{4}\left[\left(\mathbf{E}^{(+)}\cdot\mathbf{d}_{il}\right)\left(\mathbf{d}_{li}\cdot\mathbf{E}^{(-)}\right) + \left(\mathbf{E}^{(-)}\cdot\mathbf{d}_{il}\right)\left(\mathbf{d}_{li}\cdot\mathbf{E}^{(+)}\right)\right]. \tag{A.9}$$

These two terms can be identified with the two possible processes mentioned above, so that we arrive at

$$\langle\Delta E_i\rangle_T = -\frac{1}{4\hbar}\sum_{l\neq i}\left[\frac{\left(\mathbf{E}^{(-)}\cdot\mathbf{d}_{il}\right)\left(\mathbf{d}_{li}\cdot\mathbf{E}^{(+)}\right)}{\omega_l - \omega} + \frac{\left(\mathbf{E}^{(+)}\cdot\mathbf{d}_{il}\right)\left(\mathbf{d}_{li}\cdot\mathbf{E}^{(-)}\right)}{\omega_l + \omega}\right]. \tag{A.10}$$

Note that the numerators are not necessary equal, since total angular momentum has to be conserved. In other words, depending on the magnetic quantum number of the initial state, one of the two processes might not be possible for circularly polarized light due to the lack of appropriate intermediate states.

Now, the dipole matrix elements $\mathbf{d}_{li}$ can be factored into a universal angular part expressed in terms of Clebsch-Gordon coefficients and a residual reduced dipole matrix element. For this we need to change into a spherical basis. The orthonormal spherical basis vectors are defined as $\hat{\mathbf{e}}_{\pm 1} \equiv \mp(\hat{\mathbf{e}}_x \pm i\,\hat{\mathbf{e}}_y)/\sqrt{2}$ and $\hat{\mathbf{e}}_0 \equiv \hat{\mathbf{e}}_z$. In this basis we have $\mathbf{E}^{(+)} = \sum_q \hat{\mathbf{e}}_q E_q^{(+)}$ and $\mathbf{d}_{li} = \sum_q \hat{\mathbf{e}}_q d_q^{li}$ where the index $q \in \{-1, 0, +1\}$. This finally leads to

$$\langle \Delta E_i \rangle_T = -\frac{1}{4\hbar} \sum_{l \neq i} \left[\frac{\left| \sum_q d_q^{li} E_q^{(+)} \right|^2}{\omega_l - \omega} + \frac{\left| \sum_q d_q^{il} E_q^{(+)} \right|^2}{\omega_l + \omega} \right]. \tag{A.11}$$

In the following, we will extract the angular dependence of the dipole matrix elements.

A.3 Factoring out the angular dependence of the dipole matrix elements

Since the atomic energy eigenstates are eigenstates of the total angular momentum as well, we can use the Wigner-Eckart theorem [50, 132, 133] to separate the matrix element into a universal angular part and an atom specific radial part[1]

$$\mathbf{d}_{q,i' \leftarrow i} = \langle \alpha' F' m' | \mathbf{r}_q | \alpha F m \rangle = \langle \alpha' F' \| \mathbf{r} \| \alpha F \rangle \, \frac{\langle F 1 m q | F' m' \rangle}{\sqrt{2F'+1}} \tag{A.12}$$

with the Clebsch-Gordan coefficients $\langle F 1 m q | F' m' \rangle$. These can be expressed in terms of the Wigner 3-jm symbol (which make the symmetries more apparent, i.e. are more handy for calculations)

$$\frac{\langle F 1 m q | F' m' \rangle}{\sqrt{2F'+1}} = (-1)^{F'-m'} \begin{pmatrix} 1 & F & F' \\ q & m & -m' \end{pmatrix} \tag{A.13}$$

[1] We use the usual definition for the reduced matrix element as in Refs. [50, 56, 132]. Note that Steck [134] uses a slightly different convention by including the factor $1/\sqrt{2F'+1}$ into the reduced matrix element.

With $\mathbf{F} = \mathbf{J} + \mathbf{I}$ and $\mathbf{r}$ only acting on $\mathbf{J}$, we can reduce the double-bar matrix element further [132]

$$\langle \alpha' J' I F' \| \mathbf{r} \| \alpha J I F \rangle = \langle \alpha' J' \| \mathbf{r} \| \alpha J \rangle \ (-1)^{J'+I+F+1} \times \sqrt{(2F'+1)(2F+1)} \begin{Bmatrix} J' & F' & I \\ F & J & 1 \end{Bmatrix} \quad \text{(A.14)}$$

where the curly brackets denote the Wigner 6-j symbol. Also note that the nuclear spin $\mathbf{I}$ is unaffected by the position operator that only acts on $\mathbf{J}$, and therefore is constant throughout, just as the electronic spin $\mathbf{S}$. The new reduced matrix element can be reduced once more due to $\mathbf{J} = \mathbf{L} + \mathbf{S}$ in the same manner

$$\langle \alpha' L' S J' \| \mathbf{r} \| \alpha L S J \rangle = \langle \alpha' L' \| \mathbf{r} \| \alpha L \rangle \times \times (-1)^{L'+S+J+1} \sqrt{(2J'+1)(2J+1)} \begin{Bmatrix} L' & J' & S \\ J & L & 1 \end{Bmatrix}. \quad \text{(A.15)}$$

After plugging everything in we finally obtain

$$\langle \alpha' L' J' F' m' | \mathbf{r}_q^{(1)} | \alpha L J F m \rangle = \langle \alpha' L' \| \mathbf{r} \| \alpha L \rangle \ (-1)^{L'+J+J'+F+F'-m'} \sqrt{(2J'+1)(2J+1)(2F'+1)(2F+1)} \times \begin{Bmatrix} L' & J' & 1/2 \\ J & L & 1 \end{Bmatrix} \begin{Bmatrix} J' & F' & 3/2 \\ F & J & 1 \end{Bmatrix} \begin{pmatrix} 1 & F & F' \\ q & m & -m' \end{pmatrix} \quad \text{(A.16)}$$

where we already assumed the relevant values $S = 1/2$ and $I = 3/2$ in the case of ^{87}Rb.